

# **Ion Beam Deposition and STM Analysis of Macromolecules on Solid Surfaces in UHV**

THÈSE N° 5147 (2011)

PRÉSENTÉE LE 29 SEPTEMBRE 2011  
À LA FACULTÉ SCIENCES DE BASE  
LABORATOIRE DE SCIENCE À L'ÉCHELLE NANOMÉTRIQUE  
PROGRAMME DOCTORAL EN PHYSIQUE

ÉCOLE POLYTECHNIQUE FÉDÉRALE DE LAUSANNE

POUR L'OBTENTION DU GRADE DE DOCTEUR ÈS SCIENCES

PAR

**Nicha THONTASEN**

acceptée sur proposition du jury:

Prof. G. Meylan, président du jury  
Prof. K. Kern, directeur de thèse  
Prof. J. Barth, rapporteur  
Prof. L. Forró, rapporteur  
Prof. T. Jung, rapporteur



ÉCOLE POLYTECHNIQUE  
FÉDÉRALE DE LAUSANNE

Suisse  
2011



## Zusammenfassung

Organische und biologische Makromoleküle sind von großem Interesse innerhalb der Nanotechnologieforschung, da ihre Eigenschaften in zukünftigen Anwendungen nützlich sein können. Interessante Funktionen wie optische Aktivität, Wirt-Gast-Interaktion und molekulare Erkennung basieren auf Effekten, die auf der Ebene des Einzelmoleküles stattfinden. Zur Untersuchung der Eigenschaften und Funktionen von Molekülen mit submolekularer Auflösung ist eine atomar definierte Umgebung mit geringster Kontamination notwendig. Eine solche kann z.B. auf einer sauberen Oberfläche im Ultrahochvakuum, wo oberflächenempfindliche analytische Techniken und fortschrittliche Nanostruktur-Fertigung möglich sind, zur Verfügung gestellt werden. Atome und kleine organische Moleküle sind mittels thermischer Vakuumsublimation einfach auf eine Oberfläche im Vakuum zu übertragen. Viele große funktionale Moleküle sind jedoch nicht verdampfbar und zerfallen bei erhöhter Temperatur, was ihre Anwendung und Untersuchung innerhalb der UHV-Umgebung verhindert.

Zur Erforschung der Eigenschaften einzelner sowie zu Nanostrukturen assemblierter nichtflüchtiger Moleküle auf Oberflächen wird Elektrospray-Ionenstrahldeposition (ES-IBD), eine Technik für Übertragung intakter nichtflüchtiger Moleküle auf Oberflächen im UHV und in-situ Rastertunnelmikroskopie (STM) kombiniert. Eine im Hause entwickelte ES-IBD-Quelle ermöglicht Molekularstrahl-Depositionen mit beispielloser Prozess-Kontrolle. Die Zusammensetzung des Ionenstrahls wird mit Flugzeit Massenspektrometrie (TOF-MS) vor der Deposition bestimmt. Molekularer Fluss und Bedeckungsgrad, die durch den Ionenstrom und die Strahlenergie kontrolliert sind, können gemessen und gesteuert werden. Die modifizierten Oberflächen werden in-situ durch STM charakterisiert, was die Abbildung der strukturellen und elektronischen Eigenschaften mit submolekularer Auflösung erlaubt. Ex-situ Analyse durch Rasterkraftmikroskopie (AFM) erlaubt die Untersuchung der Strukturbildung auf der Meso-Skala. Abgesehen davon werden Laser Desorptions Ionisierung (LDI), Matrix-unterstützte LDI (MALDI) und Sekundärionen-Massenspektrometrie (SIMS) durchgeführt, um die chemischen Kompositionen und Reinheit der adsorbierten Materialien zu überprüfen.

Diese Arbeit stellt zunächst die Grundlagen unserer Experimente und den gegenwärtigen Stand der Forschung molekularer Ionenstrahldeposition vor. Im folgenden wird die experimentelle Methode im Detail am Beispiel von Rhodamin 6G, einem organischen Farbstoff, als Modellsystem charakterisiert. Es wird gezeigt, dass homogene Schichten von intakten adsorbierten Molekülen auf der Oberfläche gebildet werden und Adsorbatmoleküle einzeln durch STM beobachtet werden können. Eine Untersuchung mit SIMS und LDI zeigt, dass die kinetische Energie der Molekülionen bei einer Kollision mit der Oberfläche bestimmen, ob intakte Moleküle oder Fragmente deponiert werden.

Molekulares Schicht-Wachstum wurde mit Cluster-Ionenstrahlen des nichtflüchti-

gen Tensids Natrium-Dodecylsulfat (SDS) untersucht. Auf Graphit und  $SiO_x$  Oberflächen werden mit AFM kristalline Strukturen, die als invertierte Doppelschicht-Membranen beschrieben werden können, beobachtet. Die Schichten zeigen, typisch für Tenside, eine Anordnung der Moleküle die auf dem Strukturmotiv einer Kopf-Kopf und Schwanz-Schwanz-Geometrie basiert. Ein ähnliches strukturelles Merkmal, das im STM beobachtet wird, ist die flachliegende Doppelreihe der Moleküle auf Cu(100) Oberflächen, was die Robustheit dieses Strukturmotivs unterstreicht.

Die Eigenschaften funktionaler molekularer Systeme wird anhand zweier großer funktionaler Moleküle untersucht: Makrozyklen-Komplexe und Proteine. Wirt-Gast-Komplexe dreier Kationen,  $Na^+$ ,  $Cs^+$  und  $H^+$ , die in der Kavität eines Dibenzo-24-Crown-8 (DB24C8) Makrozyklus gefangen sind, werden direkt in den Elektrospray-Lösungen gebildet und intakt auf die Oberflächen übertragen. Die Charakterisierung durch STM und Dichtefunktionaltheorie-Berechnungen zeigt die Struktur der Komplexe mit dem Alkali-Ion in der Kavität.

Cytochrom c, ein Ladungstransfer Protein, wird auf Oberflächen im UHV aus einem Ionenstrahl von hohem oder niedrigem Ladungszustand deponiert. STM zeigt entfaltete Stränge mit klar erkennbarer submolekularer Struktur nach der Deposition der hohen Ladungszustände. Wenn niedrige Ladungszustände deponiert werden findet man zwei deutlich unterschiedliche Strukturen. Gefaltete Proteine erscheinen als kugelige Einheiten von 2-3 nm Durchmesser, während entfaltenen Proteine als flachliegende Stränge abgebildet werden. Auf Au(111) organisieren sich die entfaltenen Stränge in kompakten, zweidimensionalen Inseln. Zusätzlich werden die Variationen der kinetischen Energie bei der Deposition und eine erhöhte Oberflächentemperatur untersucht, um deren Einfluss auf die Änderung der Konformation von adsorbierten Proteinen zu studieren.

Die Ergebnisse dieser Arbeit eröffnen neue Möglichkeiten für die Herstellung von funktionalen Nanostrukturen auf Oberflächen. Sowohl die Herstellung von Schichten als auch die kontrollierte Immobilisierung einzelner funktionaler Moleküle wurde mit ES-IBD demonstriert und mit STM in submolekularer Auflösung in-situ charakterisiert. Eine große Vielfalt nichtflüchtiger Substanzen von kleinen bis zu sehr großen funktionalen Molekülen mit unterschiedlichen Bindungsmotiven wie kovalenten, Komplex-Koordinationen oder Wasserstoffbrückenbindungen, ist ESI-kompatibel und kann daher als Baustein für die Konstruktion neuer Materialien benutzt werden.

**Schlagwörter:** Elektrospray-Ionisation, Ionenstrahldeposition, Massenspektrometrie, Rastertunnelmikroskopie, Ultrahochvakuum, Wirt-Gast-Interaktion, Protein

## Abstract

Organic and biological macromolecules have attracted great interest within nanotechnology research due to properties that can be useful in future devices. Interesting functionalities such as optical activity, host-guest binding and molecular recognition are based on effects at the single molecular level. To study the properties and functions of molecules at submolecular scale, an atomically defined environment with low contamination is of great advantage. This can for instance be provided on a clean surface in ultrahigh vacuum (UHV), where surface sensitive analytical techniques and advanced nanostructure fabrication can be applied. Atoms and small organic molecules are easily transferred to a surface in vacuum by thermal sublimation. Many large, functional molecules, however, are nonvolatile and disintegrate at an elevated temperature, which hinders their application and investigation within the UHV environment.

To explore the properties of nonvolatile molecules adsorbed at surface as well as the nanostructure fabricated from such molecules, electrospray ion beam deposition (ES-IBD), a technique capable of transferring nonvolatile molecules intact to surfaces in UHV, and in situ scanning tunneling microscopy (STM) are combined. A home-built ES-IBD setup allows molecular beam deposition with an unprecedented level of control: the ion beam composition is monitored by time-of-flight mass spectrometry (TOF-MS) prior to the deposition, molecular flux and coverage controlled via the ion beam current and the beam energy can be measured and adjusted. The modified surfaces are characterized in situ by STM, which reveals structural and electronic properties with submolecular resolution. Moreover, ex situ analysis by atomic force microscopy (AFM) allows to access meso-scale structural formation. In addition, Laser Desorption Ionization (LDI), Matrix-Assisted Laser Desorption Ionization (MALDI) and Secondary Ion Mass Spectrometry (SIMS) are performed to check the chemical composition and purity of the adsorbed materials.

This work first introduces the principles of our experiments and reviews of the literature on molecular ion beam deposition. In the following, the experimental method is characterized in detail using Rhodamine 6G, an organic dye, as a model system. It is shown that homogeneous layers of adsorbed, intact molecules are formed on the surface and single molecule adsorbates are observed by STM. An investigation by SIMS and LDI reveals that the kinetic energy of the molecular ions upon collision with the surface determines whether intact or fragment ions are deposited.

Molecular layer growth was studied using cluster ion beams of the nonvolatile surfactant SDS, resulting in an arrangement of the molecules typical for surfactants in a head-to-head and tail-to-tail manner based on the structural motive. Crystalline structures are observed by AFM resembling inverted bilayer-membranes formed on graphite and  $SiO_x$  surfaces. A similar structural feature revealed by STM is a flat-laying double row of the molecules on Cu(100) surface showing the robustness of the

structural motive.

The properties of single molecular functional systems are studied on two types of large functional molecules: macrocycle complexes and proteins. Macrocyclic host-guest complexes of the three cations:  $Na^+$ ,  $Cs^+$  and  $H^+$  trapped in the cavity of dibenzo-24-crown-8 (DB24C8) are formed in the electrospray solutions and transferred intact to the surface. Characterization by STM and density functional theory calculations shows the structure of the complexes with the alkali ion present in the cavity. The shape of the complex at the surface is also determined.

Cytochrome *c*, an electron transfer protein is deposited on surfaces in UHV as an ion beam of high or low charge-state. STM reveals unfolded strands with distinguishable submolecular structural features after the deposition of high charge states. When low charge states are deposited, two significantly different structures are observed. Folded proteins appear as globular features of 2-3 nm diameter, while unfolded proteins are imaged as flat strands. On Au(111) the unfolded strands fold into compact two-dimensional patches. Additionally, the variation in kinetic energy upon deposition and elevated surface temperature are also studied regarding the change in conformation of the adsorbed proteins.

The results of this thesis open up new opportunities for the creation of functional nanostructures on surfaces. Both the preparation of layers and thin films as well as the controlled immobilization of single functional molecules were demonstrated with ES-IBD and characterized at submolecular resolution in situ by STM. A great variety of nonvolatile substances from small to large functional molecules with different binding motives like covalent, complex coordination or hydrogen bonds, is compatible with ESI and thus can be used as building blocks to construct new materials in a well-controlled manner.

**Keywords:** electrospray ionization, ion beam deposition, mass spectrometry, scanning tunneling microscopy, ultrahigh vacuum, host-guest interaction, protein

# Contents

<b>Zusammenfassung/Abstract</b>	<b>1</b>
<b>I Introduction</b>	<b>7</b>
<b>1 Basics</b>	<b>13</b>
1.1 Molecular Interactions . . . . .	13
1.1.1 Chemical Bonding in Molecules . . . . .	14
1.1.2 Proteins . . . . .	15
1.1.3 Supramolecular Interactions . . . . .	16
1.1.4 Surface Modification by Molecules . . . . .	17
1.2 Electrospray Ionization (ESI) . . . . .	19
1.2.1 Creation of Charged Droplets from Solutions . . . . .	19
1.2.2 Solvent Evaporation and Production of Gas-Phase Ions . . . . .	20
1.2.3 Atmospheric Interface . . . . .	21
1.3 Soft Landing and Collisional-Induced Dissociation . . . . .	22
<b>2 Materials and Methods</b>	<b>27</b>
2.1 The Electrospray Ion Beam Deposition Source . . . . .	28
2.1.1 Electrospray Ionization Source . . . . .	30
2.1.2 Ion Funnel . . . . .	32
2.1.3 Quadrupole Ion Guides . . . . .	33
2.1.4 Electrostatic Lenses . . . . .	34
2.1.5 Time-of-Flight Mass Spectrometry . . . . .	35
2.1.6 Sample Holders . . . . .	36
2.2 Atomic Force Microscopy . . . . .	38
2.3 UHV surface preparation . . . . .	38
2.4 Scanning Tunneling Microscopy . . . . .	39
2.5 Matrix-Assisted Laser Desorption Ionization . . . . .	40

<b>II</b>	<b>Results and Discussion</b>	<b>43</b>
<b>3</b>	<b>Soft Landing and Collisional-Induced Dissociation (CID)</b>	<b>45</b>
3.1	Experimental Design . . . . .	46
3.2	Collisional-Induced Dissociation of Rhodamine 6G in the Gas Phase . . . . .	49
3.3	Surface Characterization by STM . . . . .	50
3.4	Characterization of Fragments on the Surface . . . . .	52
3.5	Soft Landing and Collisional-Induced Dissociation at Surface . . . . .	54
3.6	Summary and Conclusions . . . . .	57
<b>4</b>	<b>Crystalline Inverted Bilayer Growth from Molecular Cluster Ion Beams</b>	<b>59</b>
4.1	Gas Phase SDS Clusters . . . . .	60
4.2	Crystalline Growth on Surfaces in Vacuum . . . . .	63
4.3	Crystal Growth on Surfaces in Solution . . . . .	70
4.4	Conclusions . . . . .	72
<b>5</b>	<b>Grafting of Preformed Host-Guest Complexes</b>	<b>75</b>
5.1	Limitation of Thermal Sublimation . . . . .	76
5.2	ES-Mass Spectrometry of Host-Guest Complexes . . . . .	78
5.3	Proof of Soft Landing by MALDI-MS . . . . .	78
5.4	Atomic Structures at the Surface . . . . .	80
5.5	Conclusions . . . . .	85
<b>6</b>	<b>Folded and Unfolded Proteins in UHV</b>	<b>87</b>
6.1	Introduction . . . . .	87
6.2	ES-MS of Folded and Unfolded Proteins . . . . .	90
6.3	Folded and Unfolded Proteins at Surfaces . . . . .	92
6.4	Parameters Influencing the Protein Conformation on the Surface . . . . .	99
6.4.1	Influence of Thermal Treatment . . . . .	100
6.4.2	Influence of the Deposition Energy . . . . .	102
<b>III</b>	<b>Summary and Outlook</b>	<b>107</b>
	<b>Appendix</b>	<b>115</b>
	<b>Bibliography</b>	<b>119</b>
	<b>Acknowledgement</b>	<b>139</b>
	<b>Curriculum Vitae</b>	<b>142</b>



Part I  
Introduction



Nanoscience involves the study and application of nanoscale objects, defined by a size of 1-100 nm in at least one dimension. Moreover, the properties of nanocompounds can diverge dramatically from the bulk properties because a variety of physical phenomena evolves as the size of materials decreases towards the nanoscale, at which quantum mechanical effects dominate. Moreover, at such a small length scale the surface of an object becomes more influential than its volume. The aim of nanotechnological research includes the discovery of physical, chemical and biological properties of nanomaterials as well as the ability to control and manipulate objects at the atomic and molecular scales. The prospect of nanotechnology was first introduced by Richard Feynman in "There's Plenty of Room at the Bottom", a talk given at the American Physical Society conference in 1959. Feynman suggested the idea of developing methods for material synthesis using—then still unknown—tools to manipulate individual atoms or molecules to build a structure at a desired proportional size. Since then, new technologies emerged and the findings of nanotechnological research have influenced many areas of everyday life and technology such as electronics, medicine, biomaterials and energy production.[1, 2, 3]

Today, two general strategies to create nanoscale objects exist, *top-down* and *bottom-up*. Top-down approaches incorporate the production of smaller objects from larger entities. The related techniques include thin-film deposition [4], etching [5], optical and electron beam lithography.[6, 7] Top-down technologies are most advanced in the fabrication of silicon-based devices. The bottom-up approach is based on the arrangement of microscopic constituents into larger-scale assemblies. This typically involves molecular self-assembly [8], molecular recognition [9], self-organized growth [10] and other processes in supramolecular chemistry.[11] At the length scale where these processes manifest, the optical microscopy cannot be applied due to insufficient resolution. More advanced analysis tools are employed to probe the fabricated structures. In this context, the development of scanning probe microscopy (SPM) has had a great impact on nanotechnology since it can be used to visualize a multitude of physical properties down to the single atom. In general, the mechanical properties of nanostructures on surfaces can be studied using atomic force microscopy (AFM) [12], while the electronic properties are explored by scanning tunneling microscopy (STM) and spectroscopy [13]. Not only the information on surface topography and density of states can be acquired by STM but also chemical bonding, magnetic ordering and interactions, molecular excitation and vibration, recognition or hierarchical processes.[14, 15, 16] Apart from characterization, scanning probe microscope tips can also be used to pattern surfaces by moving the adsorbates.[17, 18, 19]

Nanostructure fabrication often requires a vacuum environment since contamination from the surrounding can have a great effect on the purity of the created structures. Due to the requirement of atomic precision for the construction process, already an infinitesimal amount of impurities can cause a large deviation from the desired structure. One key example where vacuum processing has been extensively

utilized is the manufacturing of semiconductor nanostructures such as quantum-well heterojunctions or quantum dots.[20, 21] Ultra high vacuum (UHV) not only enables clean and well-controlled material fabrication, but also the ability to access advanced surface analytical techniques for which UHV is required.[22, 23] These include for example SPM, photoelectron spectroscopy and low energy electron diffraction.

While nanotechnological research of materials like metals and semiconductors needs engineering of electronic band structures, shapes, or specific surfaces for distinct optical, electronic or chemical properties, functional organic molecules already possess such novel properties in nature. Many types of molecules ranging from small organic substances to macromolecules and polymers are useful for the development of biomaterials [24], nanosensors [25], or functional systems for various applications in nanoelectronics [26, 27, 28] and medicine [29]. Many functional organic and biological molecules possess unique properties which are essential in complex biological processes such as, light harvesting, electron donors/acceptors, host-guest interactions and molecular recognition.[30, 31, 32] These molecules have been extensively studied in their native environment, which are aqueous solutions.[33, 34, 35] In spite of the promising properties, a large amount of functional molecules are nonvolatile, thus difficult to be applied directly to the vacuum processing by thermal evaporation, which is the conventional way to fabricate surface-based nanostructures in UHV. These molecules disintegrate at elevated temperatures. Therefore, a suitable procedure has to be employed for transferring nonvolatile molecules intact to a surface in vacuum environment in order to build nanostructures in a clean, controlled manner.

Our approach to this challenge is to use the combination of electrospray ion beam deposition (ES-IBD) [36] and in situ analysis to investigate large functional molecules at a submolecular scale. A home-built ES-IBD [36] apparatus is employed for vacuum deposition of nonvolatile molecules on solid surfaces (see chapter 2). Using this technique ion beams of gas-phase materials are formed and deposited onto surfaces. The method allows the controlled deposition of a vast class of molecules and particles in high vacuum and in UHV. The chemical composition of the ion beam can be selected and characterized prior to the deposition. The kinetic energy of the ions can be adjusted through electric fields. If desired, collisions with background gas molecules can induce molecular fragmentation at sufficient collision energies. During deposition the collision energy of ions and surfaces can be tuned in order to yield intact molecules or fragments on the surface. Moreover, parameters, which influence the adsorption directly, namely the surface temperature as well as the ion flux and net fluence, the integrated current over the entire deposition period, are fully controlled during the experiment.

After surface modification, in situ STM is utilized for surface characterization. The measurements are performed at room temperature or at approximately 40 K. STM analysis allows the morphological and structural characterization of adsorbed material at high resolution as well as probing of electronic density of states. Thereby,

informations about the intra-molecular and molecule-surface interactions at the surface can be extracted.

In addition to in situ characterization in UHV, the deposition can also be performed in high vacuum so that the samples can be taken out for ex situ analysis by supplementary techniques, which can be applied also to nonconductive materials. Atomic force microscopy (AFM) is employed for ex situ structural characterization of the structures grown on surfaces in vacuum. This approach can also be used to determine the stability of the fabricated structures in ambient conditions as well as to characterize structures made from aqueous solutions. Matrix-assisted laser desorption ionization (MALDI-TOF) and secondary ion mass spectrometry (TOF-SIMS) are employed for the chemical characterization of deposited materials on the surface. The results are then compared with the substances contained in the initial ion beam and allow conclusions about chemical modifications on the surface.

This thesis consists of three main parts. In an introductory part (chapters 1-2), scientific principles of physical and chemical processes related to this research are explained, followed by the detailed description of experimental techniques and procedures. The experimental results are discussed in the next part divided into four individual chapters. Chapter 3 presents the versatility of surface modification which can be obtained by tuning relevant parameters during the IBD process. Rhodamine 6G, a fluorescent dye, is used as a model system to characterize the method. The effect of the kinetic energy of the ions in the gas phase and upon collisions at the surface is studied by MALDI and SIMS, showing that the collision energy determines whether the molecules will be deposited intact or as fragments. Moreover, we show that homogeneous and clean deposition is possible. The topographic images of the modified surfaces obtained by STM for low and high coverage confirm these results.

Crystal growth of amphiphilic molecules in vacuum, in the absence of hydrophilic-hydrophobic interactions, is demonstrated in chapter 4. Gas-phase cluster formation in vacuum and crystalline structure formation on surfaces of the surfactant sodium dodecyl sulfate (SDS) is investigated. These are compared with layers of the same materials grown on surfaces from aqueous solutions. The results indicate multilayered crystalline growth, which shows that ES-IBD is in principle equivalent to molecular beam epitaxy (MBE).

The last two chapters present the studies beyond small organic molecules. In chapter 5 the investigation of macrocyclic host-guest complexes is reported. A large cyclic compound in the crown ether family, dibenzo-24-crown-8 (DB24C8), is chosen as the host. Three types of cations are used as guest species to form three different complexes with DB24C8 in solution. Atomic structures of the different complexes at surface are explored and the results show the guest ion residing in the central cavity of DB24C8. Together with theoretical calculations the interactions between the host and the guest in a complex adsorbed on the surface can be explained.[37]

Of highest interest to molecular nanotechnology are biological molecules, because

of the diversity of complex functions they provide in nature. In the last chapter, the transfer of Cytochrome *c*, a protein, which is responsible for electron transport in cells, onto surfaces in UHV is presented. Normally the functionalities of biomolecules emerge from highly specific chemical interactions which are mediated by the presence of fluid and solvated ions. Thus transferring biological molecules into vacuum would mean to characterize them in an unconventional environment yet at better resolution. Here, structural differences between folded and unfolded Cytochrome *c* are revealed by STM, corresponding to initial conformations, which can be steered in solution. The influence of the deposition energy and the surface properties are studied. Apart from pre-unfolding of Cytochrome *c* in solution, an approach to unfold the proteins on surfaces is introduced by increasing the surface temperature after the deposition of folded structures.

Implications from the results and an outlook are given in the last part of the thesis. It is shown that the combination between IBD and in situ STM characterization allows to explore a large variety of nonvolatile substances at an atomic scale, which were previously unavailable in vacuum. Several types of molecules ranging from small organic substances to large biological species like proteins are studied at a submolecular level. Through these investigations the behavior of such complex molecules outside their native environment are discovered. New materials are created on surfaces in a well-defined manner. The versatility and controllability of this approach paves the way for the design and construction of nanomaterials for novel applications. In this way the distinct functions of single molecules, complexes or molecular assemblies can be exploited.

In view of the large variety of molecules and nanoparticles that ES-IBD can be applied to, this method represents both bottom-up and top-down approaches for nanostructure fabrication. The bottom-up approach involves the deposition and characterization of single molecules or complexes, which represent a functional single molecular systems. Moreover, the layer deposition of nanomaterials can also be performed by ES-IBD as a production step within a top-down approach. The ability to combine these two fundamental principles of material synthesis opens up new possibilities in the architecture of vacuum-based nanofunctional systems.

# Chapter 1

## Basics

In this chapter, the basic physical and chemical principles of molecular interactions and processes involved in transferring nonvolatile molecules from liquid environment into gas phase ions as well as the deposition of molecules on surfaces are described. In the first part, intra- and intermolecular interactions including the nature of protein folding and supramolecular interactions in host-guest systems are briefly discussed. Adsorption mechanisms of molecules on surfaces are introduced through examples of molecular systems on surfaces.

The second part focuses on molecular ion beams. The principles of electrospray ionization (ESI), that is how molecular ion beams are formed from aqueous solutions are reviewed. Furthermore, the effects of ion-surface collisions with an emphasis on molecular ions and soft landing are discussed and the related research is reviewed.

### 1.1 Molecular Interactions

The structure of matter is determined by chemical binding and molecular interactions. For molecules and complexes, where many different intra- and intermolecular interactions occurring at several strengths, complex behaviours can emerge. Hierarchies of interactions lead to highly ordered structures by self-organization or hierarchical assemblies. Several external parameters also have influences on the molecular interactions. One important criterion is the environment where the interactions occur. For instance, the interactions of molecules in aqueous solutions are mediated by solvents which are absent in the gas and solid phase. When molecules are transferred through different interfaces, they undergo several interactions. Some examples of such processes include evaporation or ionization of molecules from the solution into gas phase and adsorption of gaseous molecules onto solid surfaces. The latter is governed by intermolecular and molecule-surface interactions, which determine the adsorption process.

Similarly surface properties also play an important role in the interactions involved in the adsorption behaviors of molecules. Thermal sublimation of molecules onto surfaces has been employed for the study of molecular interactions in UHV.[38, 39, 40] This approach cannot be applied to large nonvolatile molecules since they decompose at elevated temperatures. Therefore, the investigation of large molecules on surfaces in the UHV environment has been hindered. According to this limitation, the aspects involved in intra- and intermolecular interactions such as chemical bond strengths and organizational hierarchies in these large systems are not well understood. The combination of IBD and in situ STM allows these systems to be investigated. Therefore, chemical bonds and interactions occurring upon the adsorption of large molecules on surfaces in UHV can now be characterized.

### 1.1.1 Chemical Bonding in Molecules

Atoms are attracted to one another and form bonds resulting in molecules, liquids or solids. Chemical binding is the result of the electromagnetic force, and can be categorized by bond strength and binding characteristics.[41]

Weak bonding such as **van-der-Waals**-type binding is originated from a polarization of the electron cloud in the proximity of an adjacent nucleus, causing a non-directional weak attraction. This bonding type can be found in noble gas crystals, polymers and to some extent in all materials. The energy of van-der-Waals bonds is usually below 0.04 eV.

**Hydrogen bonds** are responsible for many recognition processes in biological systems. They belong to a specific type of dipole-dipole interaction, in which a hydrogen atom binds to an electronegative atom (e.g. O, N), attracted by a dipole in an adjacent molecule or functional group. Hydrogen bonds show a variety of strengths and are highly directional. They can be categorized as strong (0.62-1.24 eV), moderate (0.17-0.62 eV) and weak ( $< 0.12$  eV). The bond lengths and angles vary between 1.2-3.2 Å and  $90^\circ - 180^\circ$ , respectively. The strong bonds tend to have shorter bond lengths and large bond angles.

**Ionic bonds** are formed between charged atoms or molecules, i.e. ions. For instance in sodium dodecyl sulfate (SDS)  $C_{12}H_{25}SO_4^-$  anions and  $Na^+$  cations are held together by the electrostatic force. Ionic compounds often form crystalline structures. The ionic bond is typically in the range of 1.0-3.5 eV.

A strong bonding such as **covalent bond** occurs between two atoms with comparable electronegativity. These atoms having unfilled electron shells are held together by sharing of electron pairs through a common wave function. The bond strength which is in the range of 2.2-4.4 eV, is determined by bond length and angle between two adjacent bonds. The fixed angle between the atoms in the covalent bonds is also responsible for the predictable shape of organic molecules. If the binding between two atoms is entirely from lone pair electrons of one atom, the **coordination bond**



is formed. In this case donor atoms donate a pair of electrons to the acceptors to form chemical bonds. Coordination bonds can be found between central metal atoms or ions surrounded by molecules or anionic ligands, which donate electron pairs to the central metal atom. A configuration called chelation is given when two or more individual bonds are formed between a polydentate ligand and a metal ion.

Apart from chemical bonding, a cooperative type of molecular attraction, which plays an important role in maintaining biological structures such as proteins or lipid bilayers, is based on **hydrophobic effect**.<sup>[42]</sup> This effect occurs when non-polar molecules are present in polar solvents, typically water. Water molecules attract strongly to one another via hydrogen bonds and thus squeezes out non-polar organic molecules to exclude them from the polar environment. This mechanism resembles attraction between the organic molecules apart from van-der-Waals force and  $\pi - \pi$  stacking interaction. The hydrophobic interaction plays an important role in the case of amphiphilic molecules which consist of both hydrophobic and hydrophilic parts. Driven by the hydrophobic interaction, amphiphilic molecules are oriented at an interface regarding the polarity of the solvents. Such self-organization can lead to a functional structure, for example lipid bilayers that form all cell membranes. On the other hand, it is possible to obtain an invert membrane with shielded hydrophobic interior provided a hydrophobic solvent.

### 1.1.2 Proteins

Proteins are important parts in living organisms since they participate as catalysts, transporters, etc. <sup>[43]</sup> in most of the biochemical processes taking place in cells. Proteins are constituted from amino acid building blocks covalently assembled in a macromolecular chain. This chain has the unique property to fold into a regular 3D structure. Fig. 1.1 shows an example of the three-dimensional protein structures. Twenty different types of amino acids existing in nature, which can be categorized based on their side-group properties being either neutral, polar, charged, etc. The properties of amino-acid side groups determine how the amino acids interact with one another and with the surrounding. The function of a protein directly depends on its structure and conformation, which result from the complex intramolecular interactions.

Hydrophobic amino-acid residues, that only bond via van-der-Waals interaction are packed together at the inside of the globule due to the hydrophobic effect in order to avoid contact with water. On the other hand, hydrophilic side chains attracted to one another and to water through hydrogen bonds, are found at the rim. The third type of amino-acid residues is amphipathic, that is having both polar and non-polar characters. Therefore, they usually act as an interface between hydrophobic and hydrophilic molecules.<sup>[43]</sup>

Four levels structural hierarchy of a protein can be classified.<sup>[43]</sup> **Primary struc-**

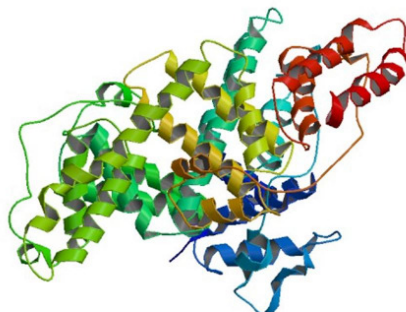


Figure 1.1: **Three-dimensional structure of human serum albumin**[44], Protein Data Bank entry 1UOR.

**tures** relates to the sequences of amino acids which are determined based on genetic code. The joining of amino acids through peptide bonds yields polypeptide chains. It is often found that the polypeptide chains can take the form of alpha helices or beta sheets which have well-defined structures, that are the **secondary structures** of proteins. These conformations are the results of hydrogen bonding between N-H and C=O groups of different amino-acid residues in polypeptide backbones or main chains. The folding of two or more secondary structures including other linking elements into a compact structure through several kinds of weak interactions results in a **tertiary structure**. Finally, the association of individual folded polypeptide chains forms a **quaternary structure** which represents the functional entity in the cell.

Protein folding, which is the consequence of molecular interactions is a very complex process, that results in the three-dimensional functional protein. The fact that this process occurs with such precision despite the dominating kinetics, is subject to the ongoing research.[45] Therefore, a study of chemical bonds and hierarchical assembly in proteins offers an opportunity to understand how specific conformations are obtained and thus how they function.

### 1.1.3 Supramolecular Interactions

Supramolecular chemistry was defined by Jean-Marie Lehn (Nobel prize in chemistry 1987) as the chemistry of molecular assemblies and of intermolecular bonds; van-der-Waals, hydrogen, dipole-dipole interaction—in other words, as chemistry beyond the molecule.[46, 47] Supramolecular chemistry was originally referred to as noncovalent interaction between a host and a guest molecule. However, mo-

dern supramolecular chemistry also evolves towards molecular devices and machines, molecular recognitions, self-assembly and self-organization which are the basic processes in nanochemistry.[41]

Host-guest interaction has been developed along with the evolution in the field of supramolecular chemistry. It can be described as the binding of a host to a guest molecule to form a host-guest complex. The guest molecules are attracted to the hosts through noncovalent interactions between the binding sites of the hosts and the guests.[48, 41] The hosts are usually large molecules such as enzymes or cyclic compounds having a central cavity. The variety of guest species range from atomic ions to sophisticated molecules like hormones, pheromones, and neurotransmitters. Donald Cram, who shares the Nobel prize in chemistry with Lehn and Pedersen in 1987, stated that the host-guest relationship involves a complementary stereoelectronic arrangement of binding sites.[49]

Supramolecular and host-guest chemistry is based on the different properties of the involved chemical bonds. A framework provided by strongly covalently bonded atoms enables the design of highly specific reactions, catalysts, sensors or molecular recognition.

The host molecules can be classified by their structures such as Corands, Cryptands, Spherands, etc. Corands are the first type of host molecules developed by Pedersen.[50] They can be described as macrocyclic polyether that can be synthesized varying the number of oxygen atoms in the ring. This group of molecules are named crown ether with dibenzo-18-crown-6 being the first type discovered. Crown ethers are popular in complexation chemistry due to the versatility of affinity to numerous guest species as well as many possible ways of synthesis. Moreover, functionalization can be performed and derivative compounds can also be created.

Each type of crown ethers has a selectivity for binding specific types of cations. For example, 15-crown-5 has high affinity for  $Na^+$ , 18-crown-6 for  $K^+$ , 21-crown-7 for  $Cs^+$  and 30-crown-10 for two  $Na^+$  ions.[41] The ion affinity of crown ethers are usually higher than linear polyethers due to chelate effect [51] and partial preorganization (macrocyclic structure) [49].

#### 1.1.4 Surface Modification by Molecules

Modification of solid surfaces by functional molecules provides an opportunity to create tailored nanomaterials for specific novel applications. In combination with advanced surface characterization techniques, chemical bonding and interactions of molecules occurring at the surface can be studied and applied to yield the desired structure. Apart from understanding the chemical processes, the surface investigation allows to discover new properties and functions of materials, which can be useful for the design and fabrication of a more sophisticated molecular systems on the surfaces.

Organic molecules are widely used as building blocks for the molecular assembly

due to their variety of functions, flexibility and controllable synthesis. One of the special focus is on biomolecules such as amino acids [52] and peptides [53, 54] which in most cases have the ability to form hydrogen bonds in specific directions. Such mechanisms are the basis for folding of proteins into particular structures responsible for their corresponding functions.

The folding of proteins in nature relies on several factors including the fluid environment. In the nontypical environment on solid surfaces the protein's conformation and function could be different. Several studies have been performed to characterize the immobilized proteins on surfaces prepared at solution interfaces.[55, 56, 57, 58, 59] The conformation, orientation as well as chemical properties of the adsorbed proteins are characterized by several approaches. Among those, electrochemical STM (EC-STM) is often employed to study the electron transfer properties of proteins, which, in many cases, indicates the retaining of their functions.[60, 61] The vacuum preparation of a protein coated surface, which allows advanced in situ analysis has not been shown by any methods other than ES-IBD (see chapter 6).

Apart from the adsorption and assembly of one molecular type at surfaces, coadsorption between two different substances can be performed to achieve a higher level of complexity. An important example is the formation of host-guest complexes. The well-known metal-Porphyrin and -Phthalocyanine complexes has been widely investigated in liquid and vacuum, showing a great variety of functions and organization of a network through self-assembly.[62, 63, 64, 65]

While at the solid-liquid interface the electrochemical properties of the surface-electrolyte-adsorbant-system plays the key role in the adsorption process, in vacuum the adsorption of molecules on surfaces is determined by binding energies, molecular flux, surface properties, and temperature. The binding energy between the molecules and the surface as well as the temperature determine the diffusion of the molecules on the surface. Based on the binding energy, the adsorption can be categorized into physisorption (no chemical change in the molecules) and chemisorption (with chemical change in the molecules). Physisorption occurs through weak binding caused by van-der-Waals- or dipole-dipole interactions between the molecules and the surface at a separation distance larger than 0.3 nm. On the other hand, chemisorption which is a strong binding results from covalent or ionic bonds at a shorter distance from the surface.[52]

In the physisorption regime, important processes involved in the construction of well-defined nanostructures can occur. Self-organization and self-assembly processes depend on the ratio between the flux of the molecules that is supplied and the diffusion on the surface. When a high flux of molecules is supplied and the diffusion is low, the competitive diffusion and molecular interactions lead to a self-organized nanostructure.[66] In contrast, a low flux of molecules combined with high diffusion on the surface leads to self-assembly, in which the system reaches thermodynamic equilibrium. The mechanism which controls self-assembly based on the interplay be-

tween the interactions among the molecules and the interactions between molecules and the surface.[67]

## 1.2 Electrospray Ionization (ESI)

Mechanisms involved in a liquid emerging from the end of a tip in an electric field have been studied since 1914.[68] Followed by some development [69, 70], a process named "electrospray" was proposed by Dole in 1968.[71] The early research narrowly focused on specific types of polymers and only in mass spectrometric aspects. The development of the technique into a new eminent tool for biochemical application was first introduced by Yamashita and Fenn in 1984 [72] as Electrospray Ionization (ESI).

In general ESI allows a large variety of nonvolatile molecules from aqueous solutions to be transferred intact into gas phase ions. Those can be positive or negative, single or multiple charged. The ionization methods which had existed before, such as fast atom bombardment and plasma desorption make use of highly localized energetic processes of short duration to ionize molecular substances into the gas phase. These mechanisms could only applied very limited to molecules since fragmentation occurs frequently.

The common application of ESI is in mass spectrometry, in which nonvolatile molecules in solutions are transferred into gas-phase ions at the interface to the mass spectrometer.[73] In this work, ESI is employed as the source to produce gas-phase molecular ions to form an intense continuous beam for vacuum deposition since it can be applied to a large variety of molecules and particles including fragile biological substances such as proteins. In the following the basics of ESI are reviewed with respect to the implications for mass spectrometry and deposition.

### 1.2.1 Creation of Charged Droplets from Solutions

The first step in the ESI mechanism is the creation of charged droplets.[73] Fig. 1.2a displays an overview scheme of the positive-mode orthogonal ESI setup. The negative-mode ESI can be obtained in the same way by reversing the polarity of the power supply. At ml/hr speed a solution containing molecules is pumped in the electrospray needle which has a tip with a small orifice (1-100  $\mu m$ ). The needle and the counter electrode are connected to a high voltage power supply. To create an electrospray a high voltage is applied between the needle and the counter electrode. Since the tip of the needle is very thin, a very high electric field at the end of the tip is generated. This electric field penetrates the solution (typically contains molecules in polar solvent) through the tip of the needle. The solution is polarized and positive and negative electrolyte ions are created. The positive electrolyte ions move in

the direction towards the counter electrode while the negative electrolyte ions move towards the needle, which is connected to the positive output of the power supply. The movement of positive and negative ions in liquid in the opposite directions under an influence of electric field is based on electrophoretic mechanism.[74] The accumulation of the positive ions at the tip leads to mutual charge repulsion. At the same time the positive charge carriers are attracted by the counter electrode. When these forces overcome the surface tension of the liquid, its surface expands and form a cone called Taylor cone [75] at the end of the needle tip. At a sufficiently high electric field, a fine jet is released from the cone apex and subsequently breaks up into small charged droplets due to Rayleigh instability (Fig. 1.2b).[76]

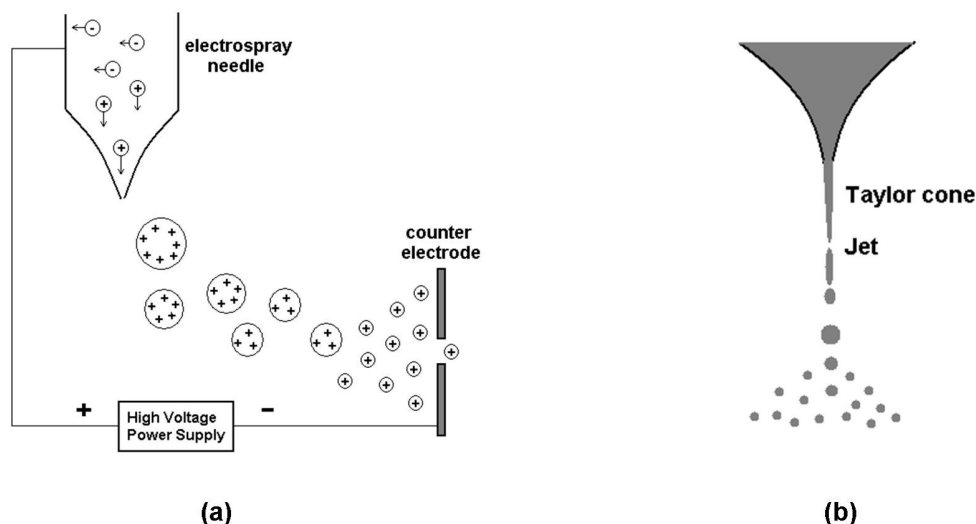


Figure 1.2: (a) a scheme of positive-mode orthogonal ESI setup, (b) a Taylor cone and jet which breaks into small charged droplets

### 1.2.2 Solvent Evaporation and Production of Gas-Phase Ions

After the creation of small charged droplets, the solvent contained in the droplets evaporates, resulting in the reduction in droplet size while the number of excess charges in a droplet remains constant.[73] This induces an increase of the electrostatic repulsion between equal charges accumulated at the surface of the droplet. The repulsive force increases as the droplet shrinks to radius  $R$  and charge  $q$ .

$$q_{R_y} = 8\pi(\epsilon_0\gamma R^3)^{1/2} \quad (1.1)$$

Equation 1.1 is Rayleigh stability condition [77] for a droplet of radius  $R$  and charge  $q_{R,y}$ , which is satisfied when the electrostatic repulsion is equal to the force due to surface tension  $\gamma$ . The charge  $q$  increases with decreasing radius  $R$  and the droplet becomes unstable. In ESI, coulomb fission [78] of charged droplets occurs near this limit resulting in a plume of smaller droplets with lower amount of charges. As this represents an iterative process, at last it results in molecular ions.

Two mechanisms were proposed for the generation of gas-phase ions from small charged droplets. The first mechanism was proposed by Dole et al. [71], the so called **charge residue model**. This model explains the situation when the electrospray solution is highly diluted. The production of gas-phase ions proceeds through the creation of very small droplets by coulomb fission containing only one molecular ion in the droplet. The gas-phase ions are obtained when the entire solvent in such droplets evaporates.

The second mechanism called **Ion Evaporation** was proposed by Iribarne and Thomson [79, 80]. According to this model, at a certain point during solvent evaporation of the charged droplets, the ions can be emitted from highly charged droplets as independent desolvated gas-phase ions. This process occurs when the radius of the charge droplet is equal to 10 nm or below. At this critical point, the ion emission dominates coulomb fission, thus the production of gas-phase ions begins.

### 1.2.3 Atmospheric Interface

The ions produced by ESI in an atmospheric environment have to be transferred into vacuum to be used for mass spectrometry or deposition. The transfer and formation of an ion beam from the ion cloud generated by ESI will be briefly explained in this section.[81, 82, 73]

Fig. 1.3a shows a scheme of the phenomena occurring at the atmospheric-vacuum interface. Gas-phase ions created at atmospheric pressure enter a vacuum vessel through an aperture along with the background gas ( $N_2$ ). Ions and gas are expanded and accelerated into the vacuum side due to a large pressure gap between two sides of the aperture. In the region close to the aperture, the mixture of ions and gas moves with speed around the sound velocity. Since the pressures are typically above  $10^{-3}$  mbar, the gas molecules still interact. Thus far from the aperture, gas molecules move randomly and are eventually pumped. In between these two regions, ions and gas molecules undergo extensive collisions within an area confined to the shock wave. The collisions leads to scattering of the beams of ions and gas. In the silent zone enclosed by the Mach disk, the expansion of ions and gas molecules result in rapid cooling. Here, ions and gas move at equal speed in the same direction.

Nozzle-skimmers combinations are conventional ion optical elements which have been used to collect collimated ion beams from the silent zone. However, the drawback of this method is the high loss of current due to the fact that relatively small solid

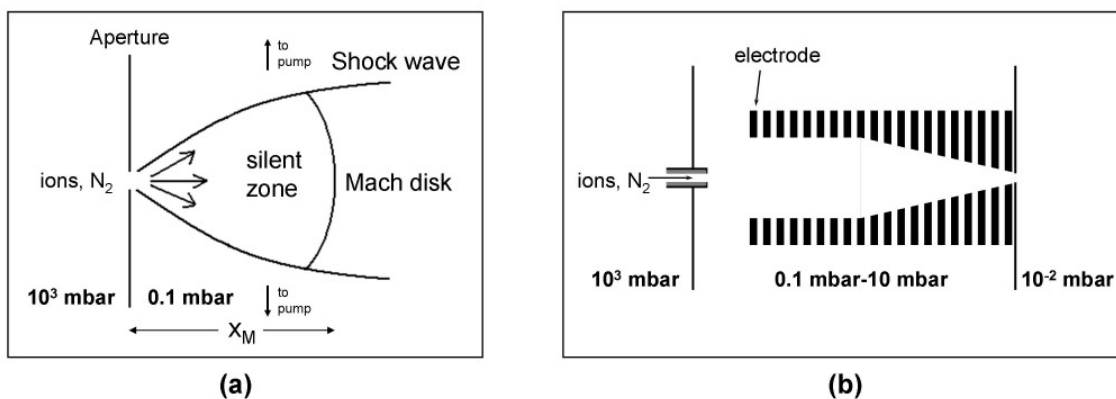


Figure 1.3: (a) gas expansion into vacuum through a small aperture (b) a scheme of an ion funnel at the vacuum interface

angle can be transmitted and thus most of the ions are blocked by the skimmer. To solve this problem, an ion optical tool, the so called ion funnel, has been developed. These devices achieve ion currents of one order of magnitude higher than the conventional skimmer interface for the same experimental conditions.[83] A scheme of an ion funnel with interfaces to both atmospheric and low pressure is shown in Fig. 1.3b. The ion funnel consists of a series of ring electrodes with subsequently decreasing internal diameters. Radio frequency- and dc-voltages are applied to each electrode in such a way to create an effective potential that confines the ions from the expansion to the central axis.[83] As a result an effective transmission of the ions to the low vacuum side can be achieved over a wide  $m/z$  range. A home-built ion funnel is employed in our IBD setup to increase the current yield.

In summary, molecules in solutions are ionized into gas phase by ESI. A capillary, a nozzle-skimmer combination or an ion funnel can be used at the interface to transmit the ions from atmospheric pressure to vacuum. Ion beams are formed in vacuum and can be used for mass spectrometry or depositions.

### 1.3 Soft Landing and Collisional-Induced Dissociation

The result of the deposition of particle beams on surfaces can be influenced by several parameters, such as the properties of particle and surface, exposure time, or incidence angle.[84] For molecular ion beam one crucial parameter is the kinetic energy of the ion, since it does not only exceed those of conventional thermal beams from



evaporation sources by several orders in magnitude, it is, moreover, a free parameter, which can be used to influence the result. In this section, the effect of collision energy on molecular ion beam deposition at surfaces will be in focus since it has a significant influence on the IBD process, particularly the binding probability between the molecules and the surface as well as the fragmentation by ion-surface collision. Fig. 1.4 shows ranges of energy classified by different kinds of collision phenomena into thermal (0.1-1 eV), hyperthermal (1 – 10<sup>2</sup> eV), low energy (10<sup>2</sup> – 10<sup>5</sup> eV) and high energy (10<sup>5</sup> – 10<sup>8</sup> eV) ranges.

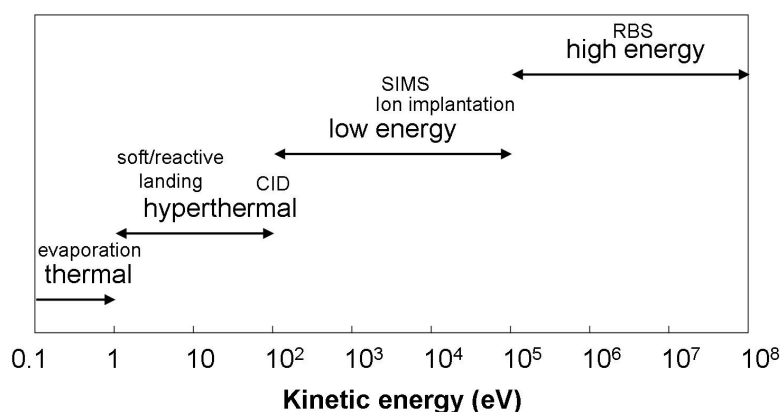


Figure 1.4: **energy range of ion-surface collision**

The lowest energy range associated with meV up to several eV collision energy is thermal range. In this range, the main processes occurring at the surface are physisorption or chemisorption of the molecules which are well-studied with neutral molecular beam from evaporation sources.

The high and low energy range of keV up to MeV is usually applied for chemical analysis of materials on surfaces and material modification. In ion beam analysis, the ion flux is usually minimized in order to avoid destruction of materials from the intense collisions. Analytical methods in this energy range are Secondary Ion Mass Spectrometry (SIMS) and Rutherford Backscattering (RBS). In SIMS, the secondary ions ejected from the sputtered surface are detected while in RBS, the detection of back-scattered primary ions is performed. For material modification, sputtering and ion implantation are typical techniques applied in these energy ranges. These methods are widely employed in semiconductor device fabrications for doping, thin-film deposition, or dry-etching.[85, 86, 87]

Relevant to molecular ion beam deposition is the hyperthermal collision energy range of 1-100 eV (see Fig. 1.4). Here inelastic scattering, adsorption, chemical reaction and modification may occur. The collision energy is equivalent to or higher

than typical energies of chemical bonds thus collisions can induce bond cleavage in which broken bonds are present together with the possibility to form new bonds. For this reason, ion-surface collisions at hyperthermal energies are a highly complex phenomenon, interesting for research in surface science. A large variety of chemical processes occurs at hyperthermal energies. Surface modification by means of IBD, particularly soft landing of molecular ions, reactive landing which induces chemical modification of the surface as well as collisional-induced dissociation (CID) at surface also belong to this energy scale. While the dissociation of several molecules can be induced by CID, some species such as fullerene ( $C_{60}$ ) could not be fragmented by collision with surfaces, even at the energy above 250 eV. [88, 89, 90]

Several works study chemical interactions at hyperthermal energies.[91, 92, 93] These include soft landing, reactive landing and CID. Soft landing was first proposed in 1977 [94] as a surface modification method by deposition of intact molecular ions. In some cases, charge state retention is also included in the definition.[91]

An application of soft landing was reported in 1997.[95] Polyatomic ions were successfully soft landed onto fluorinated self-assembled surface (F-SAM) at collision energy of 5 eV. The suggested reasons supporting soft landing process were steric hindrance in the polyatomic ions combined with the inert nature of the ordered matrix formed by fluorinated alkylthiolate chains. As well large biomolecules such as proteins were found to survive soft landing onto gold substrate.[96] A protein mixture was mass-selected for particular charge states of each type of proteins and soft landed onto different spots on the surface as a microarray. The deposited materials on each spot was rinsed and the corresponding mass spectra match the original types of proteins. In addition to biomolecules, ordered crystalline structures on surfaces were obtained by soft landing of synthetic nanographene molecules.[97] The nanographene was embedded in a matrix and desorbed into gas phase ions by solvent-free MALDI. Recently soft landing of reactive organometallic complexes onto an inert F-SAM was found to create chemical reactions at the interface leading to a chemically modified surface.[98] In our work, soft landing of organic dyes [99] (chapter 3), amphiphilic molecules (chapter 4), macrocycle host-guest complexes [37] (chapter 5) and proteins (chapter 6) are demonstrated.

Another type of ion-surface interaction which can be employed to study chemical reactions at surfaces is reactive landing (RL). Self-assembled monolayers (SAMs) are one important example where interactions between ions approaching the surface and atoms on the top-most layer have been studied in the framework of reactive landing.[100] Providing suitable collision energies, covalent bonds can be formed between the atoms in the functional groups of the SAM and the projectile ions creating a novel monolayer surface which is difficult to achieve otherwise.[101] Interactions of peptides with SAMs has been investigated by Laskin et al.[93] Lysine-containing peptides were found to form covalent bonds with SAM on gold surface through RL.[102] The optimal efficiency for RL was achieved when the collision energy is 40 eV. High

collision energies lead to efficiency reduction since the scattering of ions away from the surface competes with RL. Functional groups of SAMs also play a significant role in the reactions. This was found to have a greater influence on the secondary structures of soft-landed peptide ions than their kinetic energy, charge and initial conformation.[103]

Collisional-induced dissociation (CID) results from conversion of translational to internal energy during ion collisions at the surface. The first model of CID mechanism [104] involved two-step processes; excitation at surface and dissociation of inelastic scattered ions at some distance from the surface. This model is consistent with most of the experiments of polyatomic ions, but does not fully cover the CID processes of some other molecular systems. More extended explanations were later reported and can describe more types of experiments.[105, 106, 107] These include a three-step model and the evidence for dissociation both at the surface and in the gas-phase.

CID has been extensively studied, in particular as an alternative source of molecular fragments for mass spectrometry. Collisions of atomic and molecular ions with Langmuir-Blodgett (L-B) films induce chemical reaction or CID at surfaces.[108] Energy as well as electron transfer during collisions are determined by the outermost functional groups ( $CF_3$  vs  $CH_3$ ) of the L-B films. Dissociation of protein tetramers and pentamers through CID on the F-SAM surface [109] was also reported from the same group. The result yields monomers of proteins with equally-divided charges. These identical monomers could not be observed as the products from CID in the gas phase of the same initial proteins. Another example for the application of CID is the use as a probe for stability of complex formation between vancomycin and cell-wall analogue peptides.[110] Charge states of vancomycin were found to significantly influence the binding energy between the host and the guest molecules.

Collision energy is an important factor determining the interactions between the ions and the surfaces. The collision energies for IBD belong to the hyperthermal range which includes soft landing, reactive landing and CID. In chapter 3, the characterization of soft landing and CID processes upon IBD is presented. The depositions of molecular ions shown in chapter 4, 5 and 6 are based on soft landing to preserve the integrity of the molecules.



# Chapter 2

## Materials and Methods

This chapter provides a detailed description of the experimental setup as well as the methods and procedures used throughout this work. In the first part, the electro-spray ion beam deposition (ES-IBD) apparatus is presented. The entire process of surface coating, starting from preparation of electro-spray solutions to the deposition of molecules on surfaces is explained in detail. Sample preparation as well as measurement procedures are explained. The analytical methods employed for structural and chemical characterization of the modified surfaces, including AFM, STM and MALDI are described thereafter.

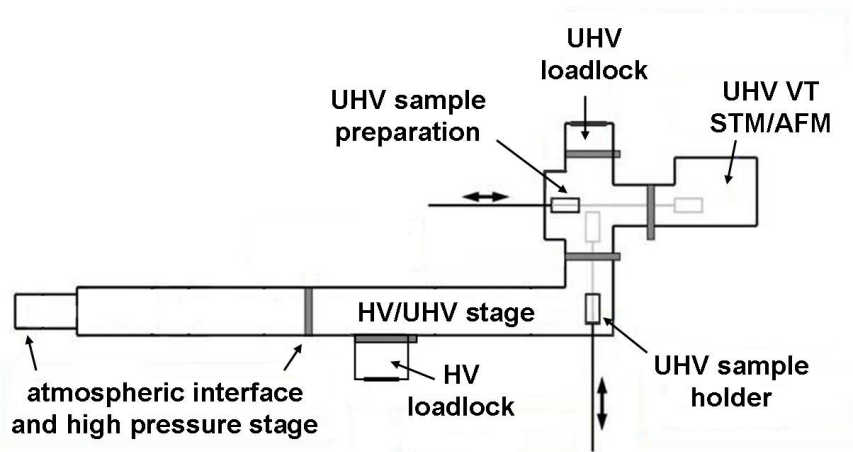


Figure 2.1: Scheme overview of the experimental setup for ES-IBD in combination with in situ STM (top view)

Fig. 2.1 shows a scheme of the experimental setup. The source is connected

to a UHV-STM via the UHV deposition chamber. The STM part consists of two main UHV chambers: preparation- and STM chamber. Manipulators and mechanical hands allow the samples to be transferred between these three parts such that the sample never has to leave UHV. A loadlock is connected to the preparation chamber in order to transfer samples and STM tips from outside. Gate valves are installed to isolate adjacent chambers. In the preparation chamber a sample stage, mounted on a manipulator, is used to transfer the tips and samples to the STM chamber as well as exchange samples with the deposition chamber. Single crystalline metal surfaces are cleaned on the sample stage in this chamber before being transferred to the deposition chamber for IBD. The ESI-source also contains a manipulator, that is used to hold the sample during deposition and to transfer it to the preparation chamber.

## 2.1 The Electrospray Ion Beam Deposition Source

The ES-IBD setup is employed for the deposition of nonvolatile molecular ions on surfaces in vacuum. Fig. 2.2 displays an outline of the machine showing all main components. The functions and characteristics of these components are described in detail in the following sections.

To transform nonvolatile molecules into intact gas phase ions, a nondestructive ionization process, namely electrospray ionization (ESI) is applied.[111] In general this technique is suitable for soluble molecules with a few exceptions, such as nonpolar or organic compounds without functional groups. Apart from the atmospheric interface, the IBD setup consists of six differentially pumped inter-connected vacuum chambers separated by apertures of 2 mm diameter intended to let the beam pass (Fig. 2.2). The first vacuum chamber (0.1 mbar) is evacuated by a roots pump (Balzers Pfeiffer WKP500A) which is capable of running at a high gas load. The other five chambers ( $10^{-2}$ – $10^{-10}$  mbar) are pumped through turbo molecular pumps. Because ESI occurs at atmospheric pressure, differential pumping is needed to attain UHV conditions in the last chamber where the deposition takes place. When the setup is idle, a gate valve between the 3rd and 4th chambers is closed and all the pumps upstream of the gate valve can be switched off. This is done to reduce noise due to ambient sound during STM measurement or for maintenance purpose. The turbopumps in the last three chambers behind the gate valve are always running in order to maintain UHV condition. As indicated in Fig. 2.2, with differential pumping it is possible to bridge the gap of 13 orders in magnitude between ambient pressure (1000 mbar) and UHV ( $10^{-10}$  mbar).

After the ions are generated and form a beam. It is collimated, focused and guided through the vacuum chambers by ion optical elements; including an ion funnel, rf-quadrupoles and electrostatic lenses. In order to achieve a controlled deposition, the ion beam composition is characterized by time-of-flight mass spectrometry (ES-TOF)

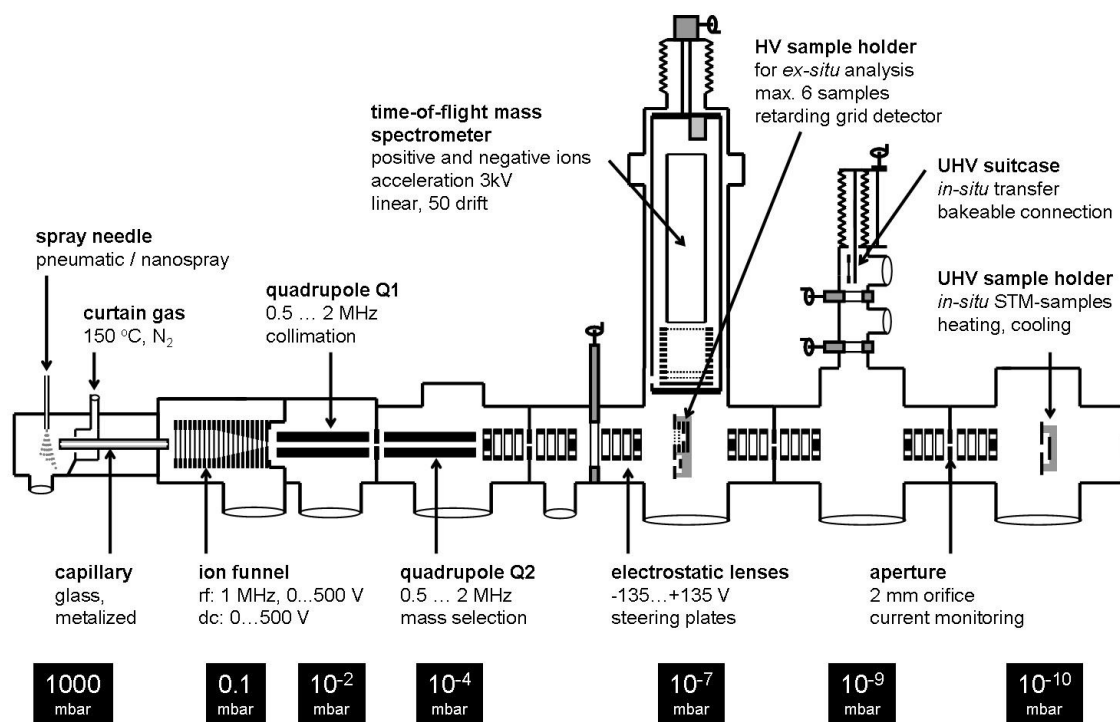


Figure 2.2: Electro spray Ion Beam Deposition Setup

before the deposition is performed. A retarding grid energy detector integrated in the HV-sample holder is used to determine the beam energy. In this manner, a mass-selected beam can be focused on the target sample and the deposition can be performed either at  $10^{-7}$  or  $10^{-10}$  mbar (see Fig. 2.2). A UHV suitcase can be employed to transfer the sample to and from the IBD apparatus without leaving the UHV condition. The ion current on the target sample is recorded with respect to the deposition time to estimate the amount of particles deposited on the surface.

### 2.1.1 Electrospray Ionization Source

Two types of electrospray sources are utilized in our ES-IBD setup. The first type is a pneumatically assisted electrospray, which is shown in Fig. 2.3a. The second type (Fig. 2.3b) is called nanospray since it utilizes spray needles of much smaller diameter and thus consumes only very little amount of solution. The needle is placed orthogonally in the pneumatically assisted source and horizontally in the nanospray source. A capillary is used in both cases to let the ions pass into the vacuum chamber. Hot curtain gas is applied against the direction of ion flow to dry off the solvents. Additionally, for pneumatically assisted source an entrance plate is placed before the capillary to direct the droplet/ion stream towards the capillary entrance.

In both sources a solution containing molecules to be ionized is fed through a spray needle. In the pneumatically assisted ESI source  $N_2$  gas at room temperature flows through a concentric outer cylinder to assist the nebulizing process. The needle assembly is purchased from Agilent Technologies (Weinheim, Germany). A high voltage of 4-4.3 kV is applied to the entrance plate and the capillary, which creates the electrospray moving towards the capillary. A hot curtain gas ( $N_2$ ) heated to the temperatures between 80-200 °C, flows through the channel along the side of the capillary and in the direction opposite to the ionized droplet motion. In combination with the orthogonal configuration, this scheme ensures the effective drying of the solvent in the charged droplets. As a result, a stable flux of gas phase ions enters into the first vacuum chamber through the capillary.

In the nanospray source, the spray needle is either a metal capillary of 50  $\mu m$  diameter or a small metalized glass needle (Proxeon Biosystem, Odense, Denmark). In operation both are oriented in-line with the capillary. To generate the electrospray, the needle is moved close to the capillary entrance at a distance of a few millimeters. A voltage of about -750 V is applied to the capillary entrance. Since the initial droplets are very small, a nebulizer gas is not needed for the nanospray source. Charged droplets are created and dried by hot curtain gas in the same way as for the orthogonal spray setup. The created gas phase ions pass through the capillary. Since a very small amount (2-10  $\mu l$ ) of solution can be loaded to the off-line nanospray needle at a time, the spray only lasts for 5-30 minutes. In continuous operation, as required for IBD, refilling would often be needed during the operation. Moreover, due



to the small amount of solvent, it is more likely to have contamination as compared to the pneumatically assisted spray source for which a large volume (usually up to 20 ml) of solution can be provided without interrupting the spray process.

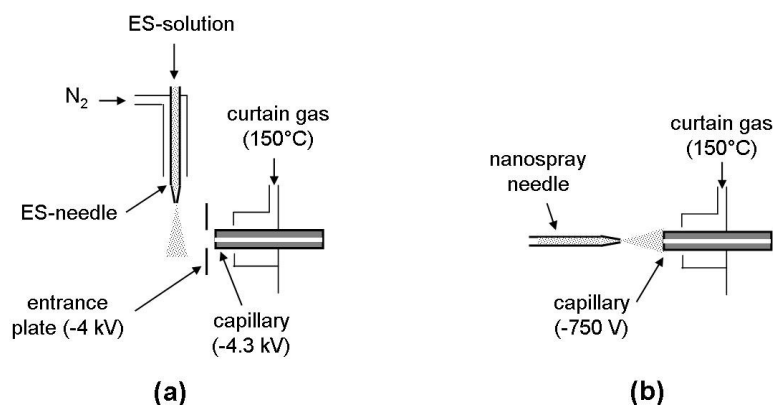


Figure 2.3: **Electrospray Ionization Source** (a) Pneumatically assisted spray source, (b) Nanospray source

Consequently, the nanospray source is preferably used for mass spectrometry experiments. Only very small amounts of material is needed to create an ion beam, which is needed for a few minutes to complete a measurement. For deposition experiments, however, a stable current is needed for the whole duration of deposition, which can last up to several hours. The nanospray setup with the small glass needle is not suitable for such purpose since the needle can be clogged easily from the accumulation of the solid materials at the apex. Due to the missing nebulizer gas, the produced current is less stable compared to the orthogonal setup and might contain small droplets. Therefore, for depositions the pneumatically assisted spray source is better suited.

Electrospray solutions are prepared by dissolving the substances in appropriate solvents, which need to be polar, and moderately volatile. Typical solvents are water, methanol (MeOH), ethanol (EtOH) and acetonitrile (MeCN) and mixtures of those. In some cases in which the substance cannot be dissolved in one of the typical solvents, diethylether, dichlormethane (DCM), trichlormethane, acetone or tetrahydrofurane (THF) are used. These uncommon solvents usually cause a less stable spray and lower current due to their low polarity or high volatility.

For positive-mode ESI, a small amount of acid is often added to the solution in order to increase the concentration of  $H^+$  and thus the current. In general, 0.1-1.0 % vol formic acid (HCOOH) is added. In some cases the presence of acid or other ions can change the chemical state of the substances causing them to be ionized in

an unusual way. For example, in protein solutions, denaturing can occur at low pH value. Also in the solutions of crown ethers,  $Na^+$  and  $Cs^+$  are added as charge carriers to explore the host-guest interactions. For mass spectrometry experiments, the concentration of the prepared solution is about  $1 \mu mol/ml$  while up to two order of magnitude higher concentration is required for deposition experiments.  $10^{-2} - 10^{-1} mmol/ml$  are the typical values that represent a good compromise between high current and limited contamination of the source.

### 2.1.2 Ion Funnel

In order to achieve high currents for deposition, a nozzle-skimmer is replaced by an ion funnel to collimate and guide the ion beam through the first vacuum chamber after the supersonic expansion at the capillary exit. Fig. 2.4a shows a model of the ion funnel as cross section along the axis. The device consists of a series of ring electrodes which have decreasing internal diameters at the downstream side resembling an actual funnel. The first electrode has the inner diameters of 30 mm after a cylindrical part. The inner diameters of the following electrodes decrease linearly towards the exit. The last electrode has an inner diameter of 2.5 mm. Rf- and dc-voltages are co-applied to these electrodes through a resistor-capacitor-circuit. The ions are trapped radially by the rf-field and accelerated through the funnel by the superimposed dc-voltages to create a funneling effect in the narrow part. The effective potential barriers resulting from the rf-field become more significant as the inner diameter of the electrode become smaller. The height of the effective potential barrier is also charge-state and mass dependent.[112] Additionally, collisional damping of the ions by interaction with buffer gas is crucial to make sure that the ions do not gain too much energy from the rf-field.

Fig. 2.4b shows simulated trajectories of particles with different  $m/z$  through the ion funnel at 0.1 mbar with an rf-amplitude of 200 V and a dc-voltage of 50 V. The effect of collisions between particles and buffer gas on the ion trajectory and transmission can be clearly seen for low  $m/z$  particles (10 Th). Moreover, those light particles are trapped by the rf-potential at the narrow end which leads to a low transmission in this mass range. The particles of 1000 Th can be transmitted efficiently through the funnel while the trajectory of higher  $m/z$  particles (10000 Th) diverges due to the high initial kinetic energy gained in the supersonic expansion, which enables heavy ion to get beyond the effective potential barrier. This beam divergence makes the heavy particles hit the electrodes of ion funnels and leads to low transmission for very high  $m/z$ . Since ESI typically supplies ions in the  $m/z$  range up to 5000 Th, by replacing a skimmer with an ion funnel, the obtained current increases by one order of magnitude.

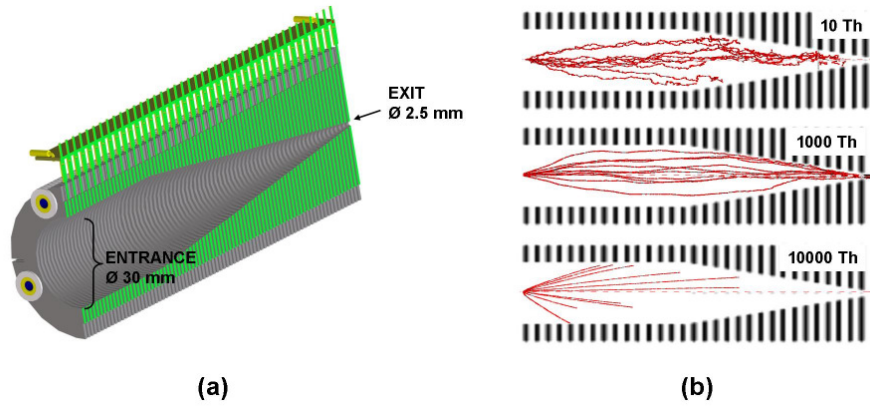


Figure 2.4: **Ion Funnel** (a) a model of an ion funnel cut through the axis (b) simulated trajectories of different  $m/z$  particles through the ion funnel at 0.1 mbar with an rf-amplitude of 200 V and a dc-voltage of 50 V

### 2.1.3 Quadrupole Ion Guides

Two quadrupoles with an identical geometry are used in the IBD setup. Both of the quadrupoles have 10 cm length and the radius of each rod is 3 mm. The four rods are assembled in the way that the radius of the cavity is 2.5 mm. The operating frequencies can be chosen between 0.5, 1 and 2 MHz. RF-voltages between 0 V and 600 V can be applied.

Due to the high operating pressure ( $10^{-2}$  mbar) quadrupole Q1 is usually operated at the voltage below 200 V. At high rf-voltages the metallization of the insulating components can occur due to gas discharge creating a shortcut between quadrupole rods. Q1 is used for the beam collimation and as an ion guide. The ions exiting the funnel are trapped in the radial rf-field and thermalized by the collisions with buffer gas. Equivalent to the ion funnel, the collisional damping supports the trapping, so that no high fields are needed. A difference in dc-potential at the exit aperture between Q1 and Q2 extracts the thermalized ions into the next chamber ( $10^{-5}$  mbar). At this pressure no collisions with buffer gas occur. Therefore, the kinetic energy of the ions is defined at this stage and the absolute dc-voltage at this aperture can be used to control the kinetic energy of the ions.

Quadrupole Q2 is used as an ion guide and for mass selection. It is operated at the pressure of about  $10^{-5}$  mbar. Mass selection can be done by applying differential dc-voltages between the two pairs of quadrupole rods.

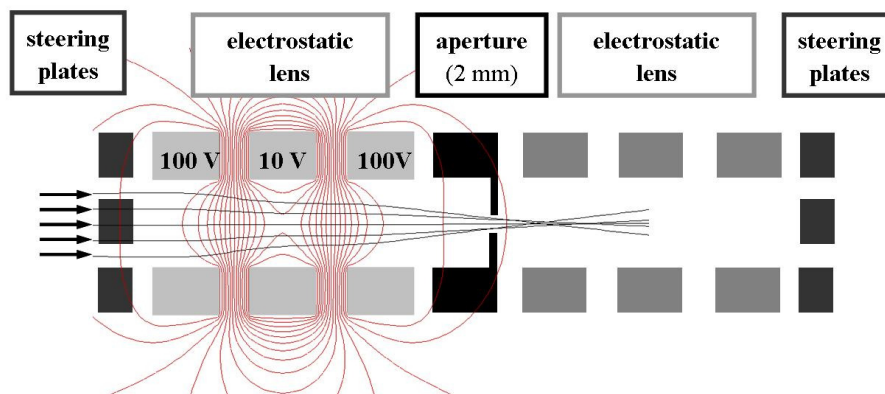


Figure 2.5: **Ion optical assemblies** consist of electrostatic lenses, steering plates and apertures.

### 2.1.4 Electrostatic Lenses

Ion beams are focused and guided throughout the whole high vacuum part of the apparatus by ion optical assemblies, which are composed of electrostatic lenses, steering plates and apertures. Each lens consists of three concentric ring electrodes of 10 mm diameter while a 4-fold segmented ring constituting a set of steering plates, which can be used to control the beam directions. Between two lens systems there is an aperture of 2 mm diameter, which separates two successive pumping stages. The lens upstream of the aperture is used to focus the ions through the hole into the next chamber, the lens downstream is used to restore the beam collimation. Voltages can be applied to the lens to focus the ion beam at a certain desired local distance, while steering plates can move this point within the focal plane. Like this, the points of interest, such as the sample surface, the extraction volume of the mass spectrometer or an aperture can be targeted precisely. Applying a proper set of voltages to the steering plates and lenses is aided by software control of a multitude of voltage channels. To choose the right voltages, the beam is steered around the central axis by the steering plates while recording the current on an electrode area comprising the spot where the beam should be directed to (see chapter 3, Fig. 3.1c). This process leads to a current image of the area where the desired target point can be visualized. The voltages applied to the steering plates can then be chosen in a way that the beam is directed to the target point.

## 2.1.5 Time-of-Flight Mass Spectrometry

The linear time-of-flight mass spectrometer (TOF) is employed for chemical characterization of an ion beam before the deposition. Ions are accelerated through the TOF by an electric field and arrive at the detector at different time depending on their  $m/z$ . The TOF is placed in the 4th chamber where the pressure is  $10^{-7}$  mbar. It is mounted onto a vertical manipulator so that it can be moved into the beam axis for mass spectrometry and out of the beam when the depositions are performed. Fig. 2.6 displays a model of the TOF and the corresponding potential landscape when it is operated at positive (black voltages) or negative (blue voltages) mode, respectively.

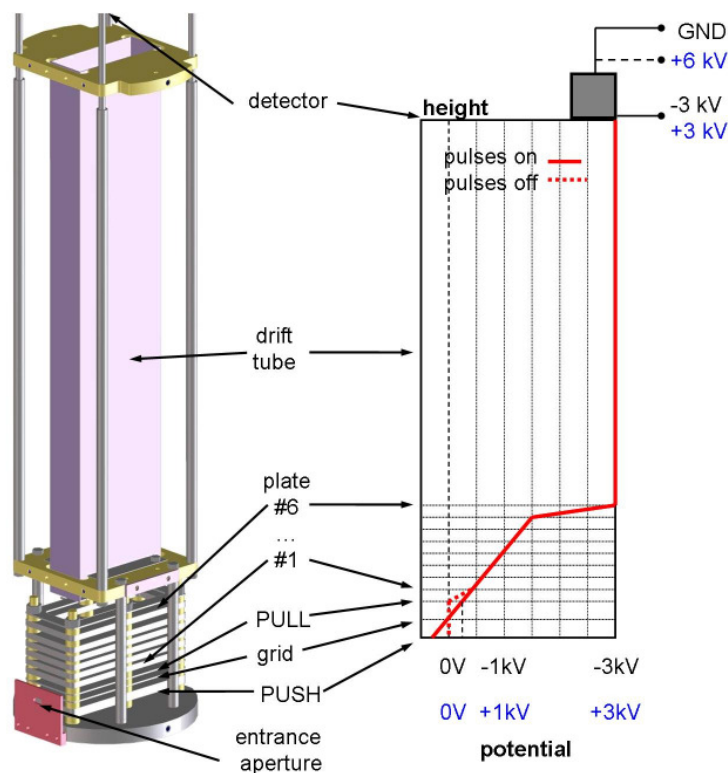


Figure 2.6: **TOF Mass Spectrometer**, a model of the TOF and its components including the potential landscape for the positive (black) and negative (blue) ion modes

The beam enters the TOF through an entrance aperture and fills the extraction region between the push-plate and a grounded grid. Push- and pull-plates are pulsed in order to extract the ions from the extraction into the acceleration region which

consists of six frame plates of rectangular shape. To accelerate the ions, increasing time-independent voltages are applied to the frame-shaped plates from plate 1 to plate 6. These voltages are negative for positive ions and reversed for negative ions. After acceleration, the ions enter the field-free drift region inside a drift tube and fly to the detector which is mounted on top. The voltage of -3 kV (positive mode) or +3 kV (negative mode) is applied to plate 6, the drift tube and the detector, which is either operated versus ground potential (positive mode) or +6 kV (negative mode). When an ion reaches the detector, a current pulse is produced by the amplification of secondary electrons created upon each impact event. In an external preamplifier the current pulse is further amplified, discriminated and the resulting signal is converted into TTL pulses, which are recorded digitally by a time-to-digital card in a PC with 1 ns resolution. A histogram of counts with respect to flight time of the ions represents the TOF-spectrum which can be converted to a mass spectrum through a calibration.

Calibration is performed in order to convert the obtained data which are recorded as a function of flight time into mass spectra which is a function of mass-to-charge-ratio ( $m/z$ ). The substances used for calibration are chosen based on the ability of peak identification to deliver the need fix-points. Typically salts are used since their mass spectra contain a manifold of well-separated peaks which can be easily identified. The ion beams obtained from salt solutions consist of mostly singly charged clusters which are produced from drying droplets containing salt ions.[113, 114] Another important characteristic of the calibration spectra is that they should span the whole  $m/z$  range of interest in order to achieve a precise calibration for the full range. CsI and SDS (see chapter 4) are commonly used in our experiments as calibration substances.[115, 36]

### 2.1.6 Sample Holders

Sample holders for deposition are in the TOF chamber at  $10^{-7}$  mbar or in the UHV chamber at  $10^{-10}$  mbar. The samples are placed in the sample holders behind an aperture of 4 mm diameter. The sample holder in the TOF chamber (HV sample holder) serves multiple purposes. Fig. 2.7a displays a scheme of this type of sample holders.

Apart from accommodating the sample, it can also be employed to characterize the beam energy by creating potential barrier to energetically filter the incoming beam. The energy detector integrated in the sample holder consists of a shield grid, a sweep grid, plate 1 and plate 2. The two grids (0.5 mm pitch, 50  $\mu m$  tungsten wires) are used to create a linear potential slope with low disturbance to minimize the error in energy measurement to 0.1 eV per charge.[115] The voltage applied to the sweeping grid is swept from 0 to 40 V while the current on the most inner plate (plate 2) is recorded. The absolute value of the first derivative of the current as a function of the grid voltage corresponds to the kinetic energy distribution of the ion

beam. Fig. 2.7b displays a measured current as a function of grid voltage and the derived beam energy distribution.

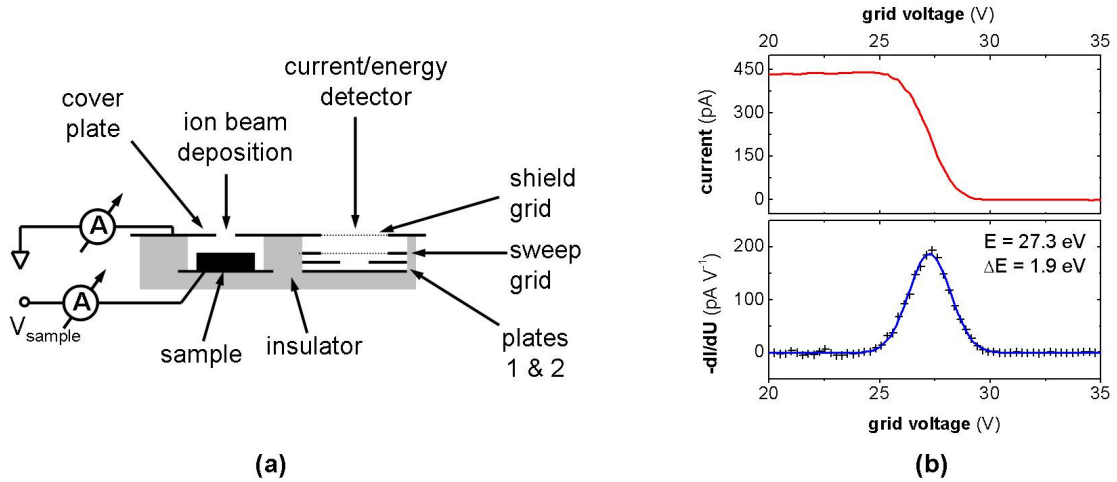


Figure 2.7: (a) HV sample holder scheme (b) data from beam energy measurement: currents on the detector (upper panel) and their absolute values of the first derivative (beam energy distribution, lower panel) as a function of grid voltage

The cover plate and the sample are separately connected to electrometers (Keithley 617) (Fig. 2.7a) for individual current monitoring. A voltage can be applied to the sample at the time of the current measurement to adjust the incidence energy upon deposition. Two types of HV sample holders are used for depositions at  $10^{-7}$  mbar: a single sample and a 6-fold sample holders. The difference between these two types is only the number of samples that can be placed on the holders. The advantage of the 6-fold sample holder is that six deposition experiments can be performed without having to transfer the samples in and out of the loadlock for each deposition. Moreover, this design also supports the reproducibility and increases the throughput of the experiments. While a deposition is performed on one target sample, a voltage is applied to five other samples to repel the beam so that the samples left unaffected (see chapter 3, Fig. 3.1).

Based on the same principle as the HV-sample holder, the UHV sample holder is designed for accommodating the crystal samples prepared in UHV and intended for in situ STM characterization. For deposition, the cleaned sample is transferred from the preparation chamber to the UHV deposition chamber by the sample holder which is mounted on a manipulator (see Fig. 2.1). The sample can be cooled and heated on the UHV sample holder within a range of 100-1000 K. The heating is performed using an electron beam heating stage. A thermocouple is integrated for temperature

measurements.

## 2.2 Atomic Force Microscopy

Atomic force microscopy (AFM) is employed for surface characterization after ion beam deposition at high vacuum or after liquid deposition of reference samples. It is a scanning probe technique for visualizing surface topography at nanometer resolution. AFM imaging is based on the force between a sharp tip and the surface. This force is kept at a constant level by a feedback mechanism. A topographic image is recorded by lateral rastering the tip across the surface while recording the tip height.[12]

Through out this work a commercial AFM (Nanoscope IV, Digital Instruments, Veeco) equipped with etched silicon tips is used. It is operated at ambient condition only in intermittent contact mode (tapping mode). In this mode the cantilever holding the tip is driven to oscillate up and down by a piezoelectric actuator close to its resonance frequency. The interaction between the tip and the surface induces a change in resonance frequency and thus in oscillation amplitude. In tapping-mode AFM images can be obtained by recording the height between tip and surface—the actual topography—but also the oscillation amplitude and the phase. The obtained images are then analyzed using the Nanoscope software and the WsxM software.[116]

A typical resolutions for AFM operated at ambient conditions are 10-100 nm in the lateral scale and 0.3-0.5 nm in the vertical scale. This characteristic implies that small isolated objects on a surface can easily be identified even with a low height. On the other hand, two small objects located near to each other cannot be distinguished.

In this study, samples characterized by AFM were prepared by two methods; IBD in high vacuum, and liquid deposition at ambient surrounding. For IBD, the clean samples are loaded onto the sample holder through the loadlock in the high vacuum chamber where the depositions are performed. After the depositions, the modified samples are taken out of vacuum and characterized by AFM. For liquid deposition, samples are immersed in the solution containing the molecules followed by blow-drying. The dried samples are then characterized by AFM.

## 2.3 UHV surface preparation

The single crystals used in this work are Cu(100), Au(111) and Rh(111) purchased from MaTeck GmbH (Jülich, Germany). The surfaces are prepared by three repeating cycles of  $Ar^+$  sputtering at 1 kV (15-20 min) followed by annealing for 5-15 min. This results in a clean surface with extended terrace. The annealing temperature depends on the type of metal surface; 800 K for Cu(100), 900 K for Au(111) and 1300 K for Rh(111). Typically a current of approximately 1.8-2.4 A is passed through the



filament of the ion gun (PSP vacuum technology Ltd.) resulting in a gas discharge from which a sputtering current of 12-18  $\mu A$  is extracted. This current impinges on sample surfaces with the area of 38-63  $mm^2$ . Annealing is done by electron beam heating of the samples. In this technique, electric current in the range of 2.0-2.5 A is passed through a filament beneath the sample causing thermionic electron emission. A high voltage (400-700 V) is applied between the filament and the sample accelerating the electrons onto the sample, where the kinetic energy is converted into heat. The filament is integrated in the sample holder which can be easily repaired. This design also provides local heating which leads to a fast sample cleaning process.

In some experiments, layers of atomically well-defined templates are grown on the single crystalline metal substrates, in particular the boron nitride nanomesh on Rh(111) (BN) [117, 118]. To prepare such surface, borazine is fed into the preparation chamber through a leak valve while a cleaned Rh(111) crystal is heated to 1100 K. The pressure in the chamber is kept at  $1 \times 10^{-6}$  mbar for an adsorption time of one minute. The resulting template is used in this work for the deposition of proteins (see chapter 6).

Apart from surface preparation, deposition of volatile molecules by thermal sublimation can also be performed in the preparation chamber. For this purpose, organic molecular beam epitaxy (OMBE) source is installed. The source contains a crucible, which is heated by a filament, and a thermocouple to monitor the temperature. The whole source is connected to a bypass vacuum system and thus can be retracted and isolated from the main chamber for refilling of molecules or during degassing. In this thesis OMBE was used as a reference only for the crown-ether experiment (see chapter 5) together with an additionally installed cesium atom dispenser.

The pressure in the preparation chamber is kept in the low  $10^{-10}$  mbar range by a turbo pump (Leybold, 360 l/sec). The turbo pump can be isolated from the system by a plate valve and turned off to avoid vibration noise during an STM measurement. To maintain the pressure an ion getter pump (Meca 2000, 400 l/sec) can be operated when the turbo pump is switched off.

For graphite and  $SiO_x$  surfaces, used for high vacuum deposition and reference experiments in liquid, the surface preparation is performed at ambient condition. A clean graphite surface is prepared by stripping of the top-most layer by an adhesive tape, while  $SiO_x$  samples are cleaned by sonication in an organic solvent, followed by rinsing with deionized water and drying in an oven.

## 2.4 Scanning Tunneling Microscopy

Scanning tunneling microscopy (STM) is employed for in situ surface characterization after IBD in UHV. It is a scanning probe method like the AFM, but relies on the distance-dependence of the tunneling current to probe the topography. The tunneling

current is measured between a sharp metallic tip and a flat conducting surface.[13] The gap between the tip and the surface must be small enough to allow quantum tunneling upon applying a voltage difference between the tip and the sample. To obtain the surface topography, the tip is raster-scanned across the surface in constant current mode. In this mode, the current is kept constant by regulating the tip-surface distance by a piezo with a feedback loop. As a result the topography can be extracted as the height of the piezo/tip. Due to the high sensitivity of the STM measurement, an atomically flat surface and UHV are required to achieve an atomic resolution.

The STM chamber is separated from the preparation chamber by a soft bellow and a gate valve. It contains a small ion pump (Varian, 150 l/sec), a sample storage carousel and the STM. The carousel has 12 places for storing the samples and tip holders. The commercial variable temperature STM/AFM (Omicron Nanotechnology GmbH, Taunusstein, Germany) is used for surface characterization at room temperature and at low temperature. The STM can be cooled by liquid helium through a flow cryostat down to approximately 40 K. The whole STM chamber is mounted on an active damping system (TMC STACIS 2100, Technical Manufacturing Corporation, MA, USA) to reduce noise during the measurement. Chemically-etched tungsten tips are used for the STM scan. Bias voltages and tunneling currents are varied among different samples. These parameters are given in the results and discussion part for measurement in the respective chapter.

## 2.5 Matrix-Assisted Laser Desorption Ionization

Matrix-Assisted Laser Desorption Ionization (MALDI) was simultaneously developed by Tanaka [119], Karas and Hillenkamp [120]. The invention resulted in the Nobel prize in chemistry in 2003.[121] MALDI makes use of the rapid and local heating by a laser pulse to desorb and ionize nonvolatile molecules from solid or liquid. The laser fluence determines whether the molecules will be vaporized intact or fragmentation will occur. For this reason, the power of laser can be adjusted depending on the energy needed for the desorption and ionization process. In general sufficiently rapid irradiation often leads to successful desorption of intact molecules. However, one difficulty in Laser Desorption Ionization (LDI) is that the energy transferred to the irradiated sample is usually inadequate. To solve this problem the use of matrices is implemented to facilitate energy transfer as well as to protect the molecules from damage. The choice of matrices is based on their ability in light absorption and charge transfer.[122] Good matrices in general are mildly acidic with carboxylic or phenolic functional groups as well as conjugated and/or aromatic character which provide chromophoric properties.[123] For UV-laser aryl-based acid is often used while succinic acid, glycerol and urea are the common matrices for macromolecules desorbed by IR-laser. Other examples of typical matrices are Sinapinic acid (SA),

2,5-dihydroxybenzoic acid (DHB), 2',4',-Dihydroxyacetophenone (DHAP) and Ferulic acid (FA). In the preparation of matrix solutions acetic or trifluoroacetic acid is often added to promote ionization process, except for proteins in which denaturing can occur through a change of pH.

In our experiments MALDI-TOF (Bruker Reflex IV, Bruker Daltonik GmbH, Bremen, Germany) is employed to detect the deposited materials on surfaces ex situ to confirm the chemical integrity after IBD. The mass spectrometer is operated in positive-ion mode with the laser power adjusted to 10-40 % of the full scale. In the forth pumping stage of the IBD source at  $10^{-7}$  mbar, ion beams are deposited on Si samples (7 mm x 7 mm) coated with the matrix 7, 7, 8, 8-tetracyanoquinodimethane (TCNQ) (Alfa Aesar GmbH, Karlsruhe, Germany). Substrate preparation was carried out by sublimation of TCNQ molecules onto the Si samples at 200 °C for a few minutes under ambient conditions.[124, 125]



Part II

Results and Discussion



## Chapter 3

# Soft Landing and Collisional-Induced Dissociation (CID)

Functional molecules are attractive candidates for many applications due to their specific properties such as fluorescence, catalysis, etc. Properties and functions of complex molecules are an expression of their molecular structure, in which even a small modification leads to significant changes or the disappearance of some properties. The investigation of such complex molecules by means of advanced surface analysis methods, in particular STM, requires a preparation of a surface with intact molecules in a clean environment that is UHV. Thermal evaporation has been successfully employed for the deposition of small molecules on surfaces.[126, 127, 128] However, large functional molecules often disintegrate at an elevated temperature before they sublime. To keep these molecules intact upon deposition, a gentle deposition technique has to be applied. In this chapter, ES-IBD, an experimental technique for controlled depositions of nonvolatile molecules at hyperthermal energy, is evaluated with respect to cleanliness, homogeneity and intactness of the molecules. For this purpose, samples prepared by ES-IBD are characterized with respect to gentle deposition of Rhodamine 6G molecules in vacuum. ESI-TOF mass spectrometry was performed prior to the deposition to ensure that the beam contains only the intact molecules and no fragments are deposited. By varying the beam energy, collisions of molecules with background gas or at the surface lead to fragmentation. MALDI and SIMS are utilized for characterization of the chemical components on the surface *ex situ* after the depositions. *In situ* STM analysis reveals the topography of the modified surfaces and allows to study the homogeneity. The combination of these techniques shows that ES-IBD is a suitable tool for well-defined surface modification with nonvolatile molecules.

Ion Soft landing, first introduced in 1977 [94], is defined as the intact deposition of molecular ions onto solid surfaces at very low energy (1-100 eV), in some cases including charge retention.[84] Surface modification by means of ion beam deposition

at low energy has been studied for several cases in high vacuum. [95, 96, 129, 102] Polyatomic ions were reported to remain intact after soft landing onto fluorocarbon surfaces (F-SAM).[95] It has later been shown by Cooks et al. that gas-phase ions of large biopolymers, such as proteins can be non-destructively landed onto solid or liquid matrices and recovered with retention of biological activity.[96, 129] Another recent application of molecular ion beam deposition is reactive landing, in which sufficiently high impact energy or a chemical active surface induces chemical reactions between the deposited ions and the surfaces. An example of reactive landing is the interaction between deposited peptide ions and self-assembled monolayer surfaces (SAMs).[102] Covalent bonding between the peptides and functional groups of the surface can be achieved by a proper tuning of the collision energy.

### 3.1 Experimental Design

A special design of the sample holder and the energy-controlled deposition used in many experiments are presented here. As a key parameter in order to ensure soft or reactive landing respectively, the collision energy of the ions with the surface has to be controlled to avoid molecule disintegration from crash landing or to ensure ion-surface reaction. Given an appropriately designed sample holder, this can be achieved by applying a voltage to the sample to decelerate the ions in the electric field before reaching the surface. This scheme can also be applied to avoid the contamination of the sample when no deposition is intended. For instance, when a many-fold sample holder (see Fig. 3.1b and chapter 2) is used and only one deposition is supposed to take place at a time. In this case, all other samples are biased at a voltage higher than the beam energy, so that no ions can reach the surface and only one sample is modified.

Fig. 3.1b shows a scheme of the 6-fold sample holder. A retarding grid energy detector is integrated at the center and the six samples are placed at the positions behind six holes with 3 mm diameter (marked in red) on the cover plate. By sweeping the voltages applied to the up-down and the left-right steering plates upstream the sample holder from -10 to 10 V (see chapter 2), an electric current image of this sample holder is acquired (Fig. 3.1c) and at the same time recording the current measured on the front plate of the sample holder as a function of the steering plate voltage. The image contrast is proportional to the measured current. In the current image, the energy detector can be identified as a big circle in the middle of the rectangle (marked by an arrow), which corresponds to the cover plate. Six sample positions are visible as three spots on each side, left and right of the energy detector. The sample positions are imaged at different contrast. Two samples, observed as dark bigger spots, are not biased while the other four, appearing as small light spots, are biased at +60 V.



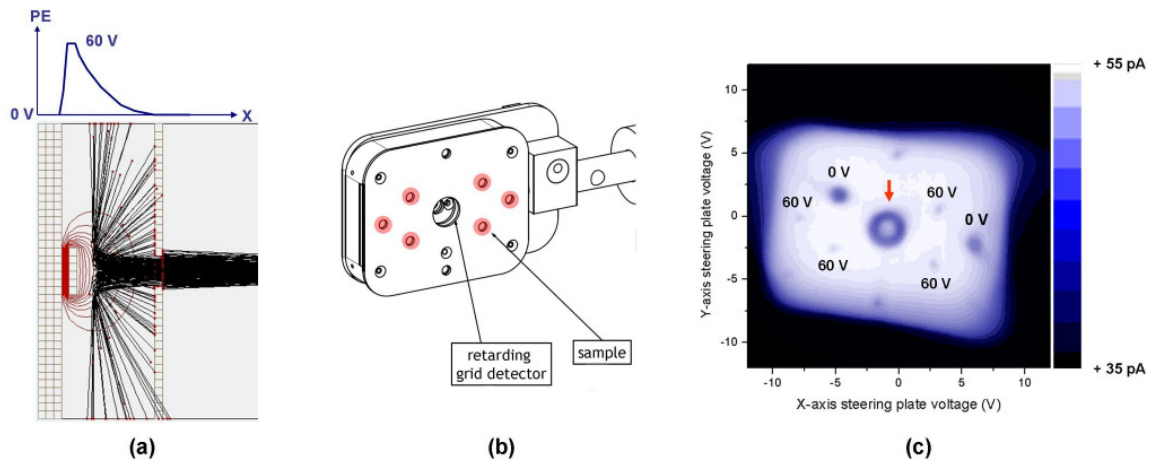


Figure 3.1: **(a) Ion trajectories obtained from a simulation and the corresponding potential energy landscape (upper panel)** Equipotential lines (red) surround the metal-sample electrode (brown). The ion beam (black) is deflected by electric field. **(b) Scheme of the 6-fold sample holder** consisting of a retarding grid energy detector and six sample positions behind a shield. **(c) Electric current image of the 6-fold sample holder** obtained by steering the ion beam. The energy detector is imaged as a big circle in the middle (see the arrow), with 6 samples as three spots on each side. 60 V was applied to four samples (small light spots) while to the others (bigger dark spots) no voltage was applied.

This deposition method can be well understood by electrostatic simulations. Fig. 3.1a shows a simulation performed with SIMION 8.0 of a sample behind the aperture and the ion trajectories (black lines). Three electrodes are located in this region; the front entrance with an aperture through which the ions can fly, the sample and the base plate. In the figure, the sample is biased at 60 V while the front and back plates are on ground potential. A cut through the potential energy landscape of the corresponding region is displayed above the image. The equipotential lines (red) are illustrated in the simulation. The electrode geometry determines the shape of the potential landscape, which is scaling linearly with the applied voltage. Therefore, only inhomogeneous potential energy is obtained around the sample position. An ion beam with a kinetic energy of  $30 \text{ eV} \pm 2 \text{ eV}$ , which is the same range as used in the experiments, is directed towards the sample. The kinetic energy of the ions at this value is not high enough to overcome the potential barrier, thus the ions are deflected in the directions depending on the electric field they experienced and their initial conditions. In such situation, no ions reach those samples but instead are reflected to the back side of the cover plate, resulting in the reduced contrast in its current image (Fig. 3.1c). On the other hand, without a bias voltage, the beam passes through the holes on the cover plate and reaches the sample, resulting in a drop of the current measured on the front plate and thus in a stray contrast. Chemical analysis of the surfaces by SIMS after the deposition confirms that the protected samples remain clean, while Rhodamine 6G is only detected on the target surface.

In summary, our method provides a controlled deposition where the beam is directed only towards the target sample, while other samples remain unaffected. It can also be employed for the adjustment of the deposition energy by accelerating or decelerating the incoming beam through the applied sample voltage. In this way, a well-defined deposition can be achieved with controlled deposition energy and coverage while contamination is excluded. It will now be shown in this chapter that the effect of deposition energy is an important factor determining the integrity of molecules on the surface.

To characterize the function of kinetic energy on soft landing and chemical modifications, ion beam deposition (IBD) of Rhodamine 6G is performed. The investigation focuses on the integrity of the molecules and the purity of the surface coating. Chemical analysis is done to prove soft landing and the cleanliness of the surface. Dissociation of molecules on the surface by increasing the deposition energy by adjusting the sample bias voltage is the effect known as collisional-induced dissociation (CID).[130, 131]

## 3.2 Collisional-Induced Dissociation of Rhodamine 6G in the Gas Phase

To monitor the chemical composition of the ion beams before deposition, ESI-TOF MS was employed. The beams of Rhodamine 6G were characterized for various declustering potentials ( $V_{decl}$ ), which defines whether CID will occur due to the intensity of the ion's collisions with the background gas. Fig. 3.2 shows ESI-TOF mass spectra of Rhodamine 6G at the  $V_{decl}$  of 50 V, 250 V and 350 V. At 50 V, a single peak at mass-to-charge-ratio ( $m/z$ ), given in units of Thomson (Th);  $1 \text{ Th} = 1 \text{ u/e}$  [132], of 443 Th is observed corresponding to single positively charged Rhodamine 6G ion. As  $V_{decl}$  increases, a series of lower  $m/z$  peaks appears. At 250 V, a series of peaks between 300 Th and 443 Th is observed. The peak distances vary in the range of 13-16 Th. The peak with strongest intensity appears at 415 Th, which corresponds to a fragment generated by the loss of one ethyl group from the Rhodamine 6G molecule.[99] At 350 V, The peak series shifts towards lower  $m/z$  values (150-443 Th), centering at around 300 Th where the strongest peak appears. The Rhodamine 6G peak at 443 Th can be observed at a very low intensity at this potential.

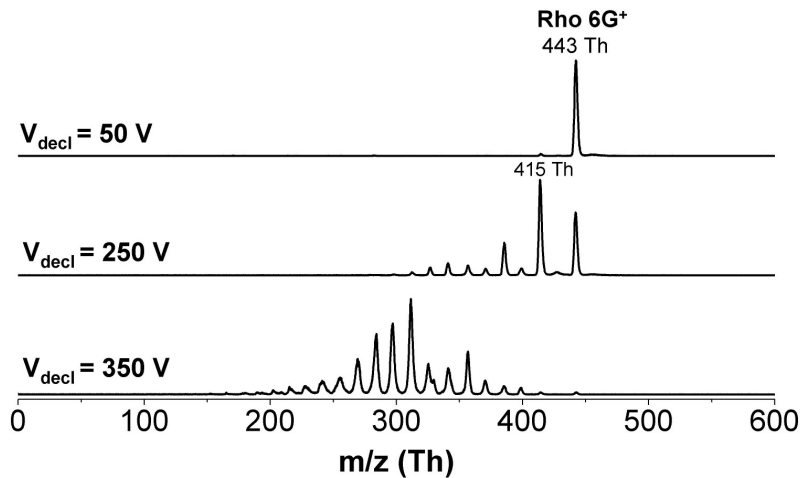


Figure 3.2: **ESI-TOF mass spectra of Rhodamine 6G at different declustering potentials** The main peak at 443 Th corresponds to single-charged Rhodamine 6G ion. Lower  $m/z$  peaks are originated from fragmentation of the molecules induced by increasing declustering potential.

These observations can be explained by nozzle-skimmer (later replaced by an ion-funnel) fragmentation (see chapter 2). The ions are accelerated and gain more kinetic energy as  $V_{decl}$  increases. These ions collide with neutral gas molecules in the first

pumping stage, resulting in collision-induced dissociation (CID) of the ions in the gas phase. Further disintegration upon increasing  $V_{decl}$  creates smaller fragments as observed by the shift of the mass spectrum towards lower  $m/z$  values.

The results indicate that the beam composition can be altered by tuning  $V_{decl}$ . Ion beams containing intact molecules or fragments can be created. This provides a method through which the intact molecule- or fragment-coated surfaces can be prepared.

### 3.3 Surface Characterization by STM

In order to demonstrate the deposition capability and test the homogeneity of the molecular film growth, in situ surface characterization by STM was performed (see chapter 2). For structural characterization by STM, ion beams containing only intact Rhodamine 6G ions (443 Th), confirmed by ES-MS, were deposited on three different surfaces in UHV. The samples were not biased by voltages which results in the deposition energy of  $26 \pm 2$  eV. STM measurements were performed in situ at 43 K because the investigation at room temperature was hindered by surface mobility of molecules and did not yield stable images. Fig. 3.3 displays topographic images of the modified surfaces: Au(111) (a, b) and Cu(100) (c). Fig.3.3d displays a zoom-in image of a commonly observed structure overlaid by a model of Rhodamine 6G. The fluence of the deposition on Cu(100) was 60 pAh, while on Au(111) the fluences of two depositions are 50 pAh and 357 pAh.

For low-fluence depositions of Rhodamine 6G on Au(111) (Fig.3.3a) and on Cu(100) (Fig. 3.3c) bright features of sizes between 1.5- 4.0 nm in diameters are observed on step edges and on terraces. The observed structures decorate the step edges of both surfaces while randomly distributed on Cu(100) terraces. On Au(111) terraces the structures are mostly adsorbed at the elbow sites. The coverage of 0.05 ML and 0.2 ML are found for the modified Au(111) and Cu(100) surfaces, respectively. A magnified view of the commonly observed small bright feature is displayed in Fig.3.3d. The structure is overlaid with a model of Rhodamine 6G molecule. Light blue color represents carbon atoms while red and dark blue correspond to oxygen and nitrogen atoms, respectively. It can be noticed that the size and shape of the structure fit well to the model.

For high-fluence deposition a coverage close to a full monolayer is obtained on Au(111) (Fig. 3.3b). A flat homogeneous layer with the same pattern as the surface reconstruction of Au(111) can be clearly observed from the topographic image.

The small structures with the size of approximately 1.5 nm, observed in Fig. 3.3a, c and d, are attributed to single Rhodamine 6G molecules. The mobility of Rhodamine 6G on Cu(100) and on Au(111) surfaces leads to step-edge decoration and some aggregation of the molecules which results in the observed larger-size features.

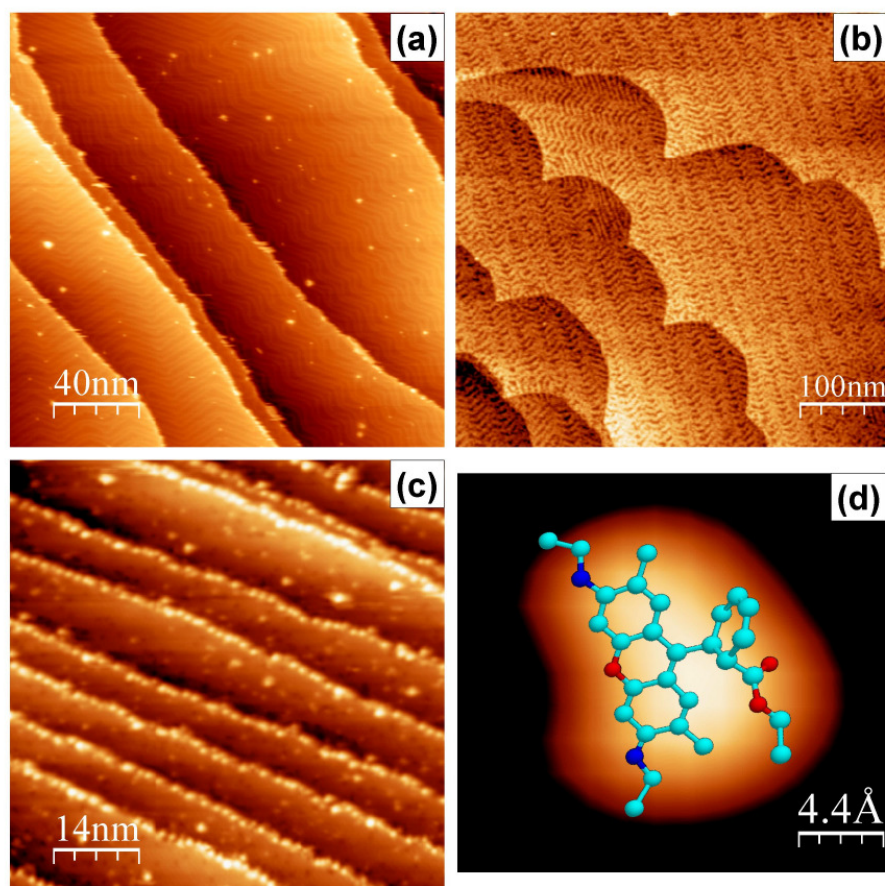


Figure 3.3: **STM topographic images of Rhodamine 6G deposited by IBD in UHV on Au(111) (a, b), Cu(100) (c) and a zoom-in structure (d)** Step-edge decoration and random distribution of bright features on terraces are observed for Au(111) and Cu(100) for low coverage. For high coverage a full monolayer of Rhodamine 6G is observed on Au(111) following the surface reconstruction. An overlaid model structure of Rhodamine 6G fits to the size and shape of the structure shown in (d).

The fact that at low coverage the single molecules are observed only at pinning sites points to a weak molecule-surface interaction as well.

The higher apparent coverage obtained on Cu(100) compared to Au(111) when depositing with same low fluence could be explained by the presence of multiple step edges in the scanned area. The surface topography of the region on Cu(100) with extended terraces (not displayed here) shows a similar coverage as the gold surface. For the high-fluence deposited Au(111) surface, the flatness and homogeneity of the full monolayer suggest the self-organization of intact Rhodamine 6G molecules following the symmetry of surface reconstruction.

STM characterization demonstrates that intact Rhodamine 6G-coated surfaces can be achieved with high purity. ES-IBD together with soft landing provides a clean well-defined surface modification with high homogeneity. The observation of single molecule on the surface suggests that no chemical modification occurs upon deposition. However, to ensure the integrity chemical characterization of the surface has to be performed after the deposition. This procedure allows to check whether the molecules remain intact and chemical components adsorbed on the surface match those contained in the ion beam (see Fig. 3.2 top panel). This result shows that the combination of ES-IBD with soft landing and in situ STM analysis is a suitable approach for the investigation of molecular structures and properties at the nanoscale.

### 3.4 Characterization of Fragments on the Surface

Based on ES-MS measurements, the fragmentation of Rhodamine 6G in the gas phase by increasing  $V_{decl}$  was discussed. In this section, chemical characterization of adsorbed Rhodamine 6G is performed in order to test whether the molecules or fragments deposited on surface can be detected and distinguished. For this purpose, three types of ion beams are prepared varying  $V_{decl}$  (see Fig. 3.2). The first beam contains only the intact Rhodamine 6G ions. The second beam contains both the intact molecules and the fragments ( $V_{decl} = 150$  V). The third beam contains only fragments ( $V_{decl} = 350$  V). Three types of samples are prepared from IBD of each ion beam on  $SiO_x$  surfaces in high vacuum. The impact energy of all depositions is below 5 eV and the fluence is approximately 15 pAh. The complementary mass spectrometric techniques, MALDI and SIMS are employed to characterize the chemical components on the surface ex situ after the depositions.

Fig. 3.4a shows MALDI-TOF mass spectra of the intact and intact+fragment deposited samples. Fig. 3.4b shows TOF-SIMS spectra of the intact and fragment-only deposited samples. For MALDI measurement of the surface coated by the intact molecules, only a single peak at 443 Th can be observed with a high intensity. As discussed before in the ES-MS section, the peak at 443 Th belongs to the intact Rhodamine 6G ions. The mass spectrum obtained from the surface deposited by

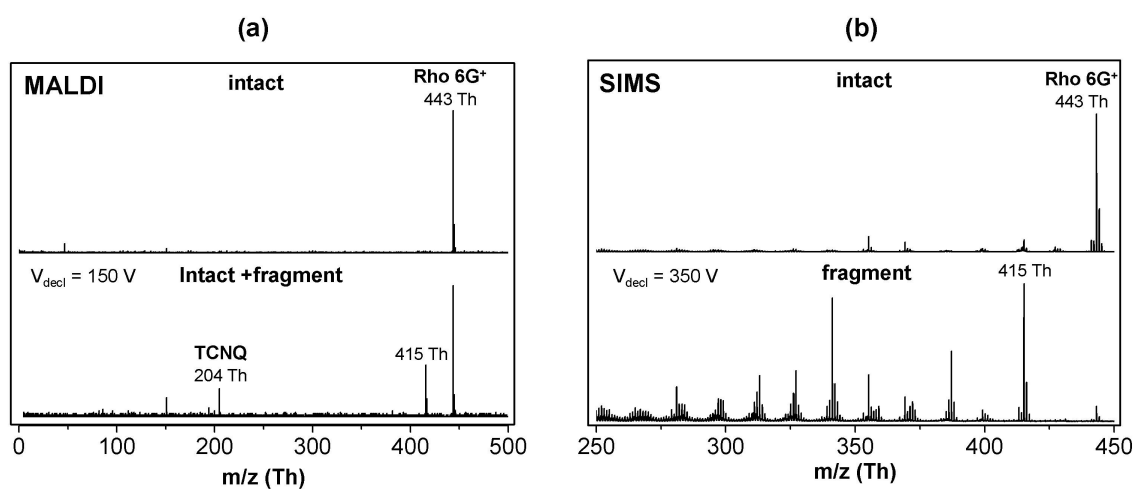


Figure 3.4: (a) MALDI-TOF mass spectra of Rhodamine 6G, intact and intact+fragment on  $SiO_x$  (b) SIMS spectra of Rhodamine 6G, intact and fragments on  $SiO_x$ . The single charged Rhodamine 6G peak at 443 Th appears dominantly in both MALDI and SIMS spectra for the intact sample. An additional fragment of 415 Th appears in the MALDI spectrum for intact+fragment deposition. The peak at 204 Th belongs to the matrix molecules, TCNQ. The SIMS fragment-spectrum shows a series of peaks in the range of 250-415 Th as the main feature.

the beam containing both intact molecules and fragments is different than the one from intact molecules only. In this spectrum, the peaks at 415 Th, 204 Th and 150 Th appear in addition to the intact Rhodamine 6G peak. The peak at 415 Th belongs to the fragment created by the loss of one ethyl group of Rhodamine 6G molecule. The peak at 204 Th, belongs to TCNQ, the molecules used as a matrix in this measurement. The peak at 150 Th, which also appears at a very low intensity in the intact mass spectrum could be originated from fragmentation of TCNQ. It should be noted that the function of matrix molecules is to assist the desorption ionization process. Therefore, in some cases where the molecules can be easily ionized without disintegration, the use of matrix molecules are not necessary.

In Fig. 3.4b, SIMS mass spectra obtained from intact and fragment deposited surfaces are shown. The Rhodamine 6G peak at 443 Th is observed as the dominant peak for the intact case. Some low intensity fragment peaks of  $m/z$  above 350 Th can also be detected. Since SIMS is well-known to easily generate fragments during the 15 keV  $Ga^+$  bombardment, a small amount of fragments detected in the spectrum must be expected. For the fragment-coated surface, a series of fragment peaks from 250-415 Th can be observed as the main feature in the spectrum. Apart from the fragments, the intact molecule peak at 443 Th also appears at a very low intensity (1%). This feature can also be observed in the ESI-TOF mass spectrum (see Fig. 3.2, the lowest panel). The fragments detected by SIMS on the surface are consistent with the fragments obtained in the gas phase by ES-MS.

The results indicate that the chemical components obtained on the surfaces by SIMS and MALDI after deposition match the components of the initial beams. An additional experiment also confirms that other samples on the 6-fold sample holder biased at 60 V neither contain molecules nor fragments. This also shows that no neutrals are deposited, since they would not be fragmented by nozzle-skimmer fragmentation. Besides, the beam was completely repelled and left such samples unaffected while the deposition on the target sample is being performed. This experiment shows that ES-IBD provides controlled depositions of molecules on surfaces. The desired chemical components can be selected as the ion beam contents and transferred to the surface in their original state.

### 3.5 Soft Landing and Collisional-Induced Dissociation at Surface

To investigate the effect of beam energy on soft landing, the voltages applied to the samples were adjusted so that the deposition energies are varied between 2-100 eV. An ion beam containing intact Rhodamine 6G was deposited onto  $SiO_x$  surfaces in high vacuum. Due to its high sensitivity, SIMS is employed for ex situ characterization



of the surfaces after the depositions. The obtained mass spectra of Rhodamine 6G deposited at the incidence energies between 2-100 eV are displayed in Fig. 3.5a. In all spectra, the same series of peaks can be observed. However, the intensity of each peak in each spectrum is significantly different. The peak at 443 Th corresponds to the intact Rhodamine 6G molecule. It is detected in all spectra up to 100 eV collision energy. Other small peaks, which are visible at low incidence energies, rise at an onset of 60 eV collision energy. The peaks of  $m/z$  lower than 443 Th, whose intensities increase with the incidence energy, are attributed to the fragments generated from the collisions between the molecules and the surface. Higher incidence energy results in smaller fragments, which appear at relatively high intensity in the spectrum for 100 eV, such as those having  $m/z$  between 355 Th and 415 Th. It can also be noticed at this energy that the intact peak has lower intensity compared to the strongest fragment peak. The fragment pattern in the spectra obtained from CID at surface are similar compared to the one from gas-phase fragmentation (see Fig. 3.4b) The results suggest that same fragments are produced either by collisions in the gas phase or at the surface.

Soft landing ratios are extracted from the SIMS data for each incidence energy. The relation between the incidence energy and soft landing ratio shown in Fig. 3.5b shows that at the incidence energy below 60 eV, more than 80 % of the molecules are soft landed. The soft landing ratio reduces significantly as the energy is higher than this value. However, due to the ionization process SIMS always creates molecular fragments. Therefore, an offset from 100 % soft landing even at the low deposition energies is present. At 100 eV, less than 50 % of the molecules remain intact upon deposition.

Soft landing energies for several types of ions and surfaces have been reported. Polyatomic ions can be soft landed onto F-SAM surface at 5-10 eV incidence energy [95] while larger molecules, like peptides were found intact after being deposited on an SAM surface at the energy up to 150 eV.[133, 93] Optimum energy for soft landing of 3 eV/charge was reported for the deposition of yeast hexokinase on both solid and liquid surfaces.[129] The proteins, MP-11, soft landed at 10-12 eV on a gold electrode, were confirmed by voltammetry to retain their native properties and electron-transfer functionality.[134] Gas-phase synthesized  $Cr(benzene)_2$  sandwich complexes were soft-landed onto  $C_{15}COOH - SAM$  on a gold substrate at 5-20 eV.[135] According to our study, soft landing energies of Rhodamine 6G are in the range of 2-60 eV, which is comparable to what reported from other studies mentioned above. However, the upper limits of soft landing or the onset for fragmentation is rarely given in other studies.

The collision energy of 60 eV, which is an order of magnitude higher than the binding energy of a C-C bond, could exceed the fragmentation threshold. However, large molecules have many degrees of freedom among which the collision energy can be distributed. Compared to the 1 eV/atom rule for soft landing energy of nanoparticles

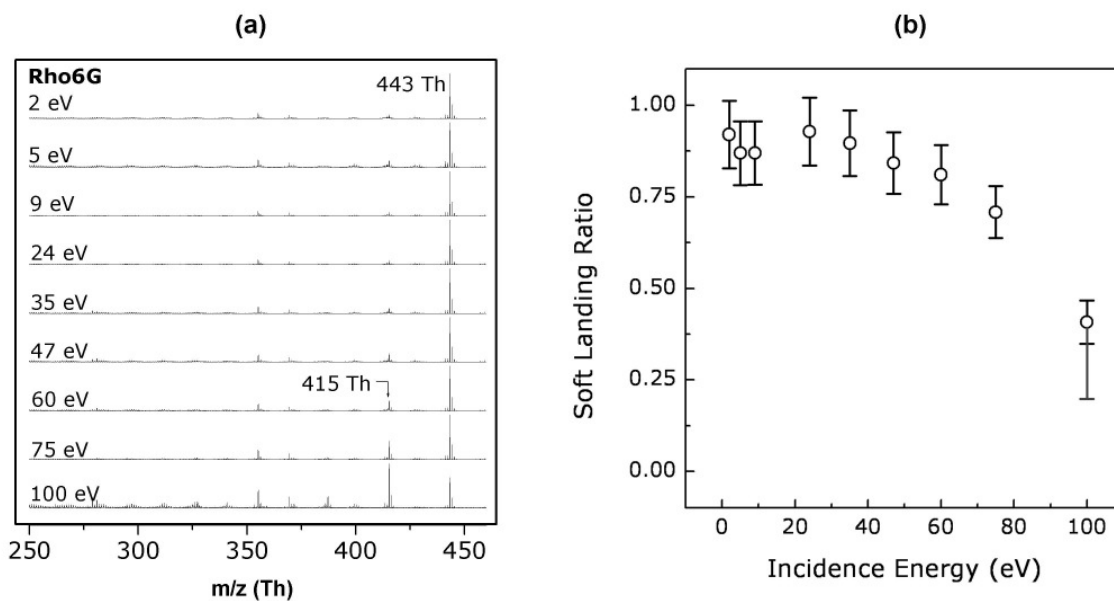


Figure 3.5: **(a) SIMS spectra of Rhodamine 6G deposited on  $SiO_x$  surface in high vacuum at incidence energies 2-100 eV** The same series of peaks was obtained in all spectra. At 100 eV, the peak corresponding to Rhodamine  $6G^+$  at 443 Th decreases in intensity relative to the fragment peaks at lower  $m/z$ . These fragment peaks rises with increasing incidence energy at an onset of 60 eV. **(b) Soft landing ratio as a function of incidence energy extracted from the SIMS spectra** Soft landing ratio decreases as the incidence energy increases. 100 % soft landing was not achieved due to additional fragmentation characteristic for SIMS.

[136], Rhodamine 6G contains 64 atoms, and thus would disintegrate at around 64 eV. This agrees well with our result.

This experiment indicates a strong effect of collision energy between the molecules and the surface on soft landing. The incidence energy has to be controlled with respect to the types of molecules and surfaces in order to maintain the molecular properties and functionalities after surface coating. Apart from soft landing, the incidence energy can also be adjusted to obtain reactive landing or to generate chemical active species at the surface.

### 3.6 Summary and Conclusions

Ion beam deposition of Rhodamine 6G implies that ES-IBD allows soft landing of molecules under clean conditions where surface modification can be achieved with high purity and homogeneity. The integrity of the deposited materials can be maintained by controlling the experimental parameters. High declustering potentials promote the collision between the ions and neutral background gas, leading to the dissociation of molecules in the gas phase. Upon deposition the incidence energy can be tuned by biasing the target sample with voltage to slow down or accelerate the ions arriving at the surface. In this way, the collision energy between the molecules and the surface can be adjusted for both soft, reactive and dissociative landing conditions. The soft landing limit of 60 eV found is very large, however it confirms the simple 1 eV/atom rule known for the soft landing of clusters.



## Chapter 4

# Crystalline Inverted Bilayer Growth from Molecular Cluster Ion Beams

Electronic devices based on organic thin films offer an attractive alternative to conventional inorganic microelectronics due to potentially lower costs and compatibility with flexible substrates.[137, 138] There has been an enormous effort in the direction of making organic molecular materials with good characteristic of field-effect transistor (FET) and low power consumption [139, 140] as well as efficient light-harvesting.[141] In order to achieve good device characteristics, crystalline organic films produced in vacuum to avoid contamination are often advantageous.

As a model system for the growth of organic crystals from ion beams, the deposition of the organic surfactant, sodium dodecyl sulfate (SDS) on solid surfaces in vacuum is presented. Crystallization of SDS has been extensively studied at the liquid-air [142], liquid-solid [143, 144] and liquid-liquid [145, 146] interfaces. The well known characteristic of surfactants is the difference in hydrophobicity between two parts of the molecule. Together with hydrophilic-hydrophobic interactions this structure gives rise to a variety of highly ordered self-assembled structures, such as micelles, tubes or membranes [147] of high stability that play an important role in many applications and our everyday life, such as foams, detergents or lubricants. Since the hydrophilic-hydrophobic interaction is the key for the self-assembly of surfactants, a variety of structures can be made from aqueous solution where this type of interactions can occur.[148, 149] However, a controlled fabrication of surfactant crystals with structural characterization at molecular level requires vacuum environment. In this case the situation could be different particularly because the hydrophobicity is absent, which might strongly effect the structure formation. The study of the assembly of surfactants in vacuum, where hydrophobic effect is hindered, thus provides a case for the design and production of new materials.

In order to study the crystal growth mechanism of SDS in vacuum, the molecules in the gas phase were deposited onto surfaces in high vacuum and in UHV by IBD. To

ensure that the ion beams contain only the desired materials, the beam composition was monitored prior to the deposition by ESI-TOF. Sublimation processing was reported to induce decomposition of SDS molecules.[149] After IBD, ex situ AFM was employed to characterize the surface at ambient condition while STM was applied for the in situ analysis in UHV. Additionally chemical characterization of the modified surfaces were carried out ex situ by MALDI to check the integrity of the chemical components on surfaces upon depositions.

## 4.1 Gas Phase SDS Clusters

### ES-TOF Mass Spectrometry

In order to check the material content of the ion beam before the deposition, a precise chemical beam characterization is needed. Here, the formation of SDS clusters in the gas phase was studied quantitatively by ESI-TOF MS. An aqueous solution of SDS equivalent to those used for liquid deposition, prepared at the concentration of  $10^{-2}M$  was used as electrospray solution. A series of mass spectra for various declustering potentials ( $V_{decl}$ ) was recorded by ESI-TOF in order to fragment the clusters and gain access to their subunits. Fig. 4.1a shows the series of mass spectra up to 7000 Th, from top down, obtained for increasing  $V_{decl}$  from 110 V to 560 V. In each spectrum, several series of peaks with equal neighboring distances can be observed. At low  $V_{decl}$ , a broad feature with low intensity without any resolved peaks appears in the  $m/z$  range above 3500 Th. At high  $V_{decl}$ , the peak series continue into this  $m/z$  range and the number of series reduce with the increasing  $V_{decl}$ . Note that at 360 V, the broad feature still exists as a background of the peak series at high  $m/z$  range above 4000 Th.

Fig. 4.1b displays a part of the spectrum in Fig.4.1a for  $V_{decl} = 110$  V, in the  $m/z$  range of 1700-2650 Th. The number assigned for each peak corresponds to the lowest possible charge of the clusters the peak represents. Apart from the smallest cluster with minimum charge, each peak also belongs to larger clusters of the same  $m/z$ . For the single-charged series (**1**), the equivalent distance between adjacent peaks corresponds to one SDS molecular mass (228 u) per one charge, i.e. the cluster size increases by gathering of more SDS molecules. In general SDS clusters can be written in the form of  $zNa^+(SDS)_n$  where  $z$  is the charge of a cluster and  $n$  is the number of SDS molecules contained in the cluster.

The broad feature at high  $m/z$  of the low  $V_{decl}$  spectra in Fig. 4.1a could be attributed to unresolved highly charged large SDS clusters. The neighboring distances between adjacent peaks at high  $m/z$  become very low. Therefore the peaks cannot be resolved due to instrumental limitation and isotopic broadening. As  $V_{decl}$  increases, especially these highly charged large clusters gain energy for the collision with the

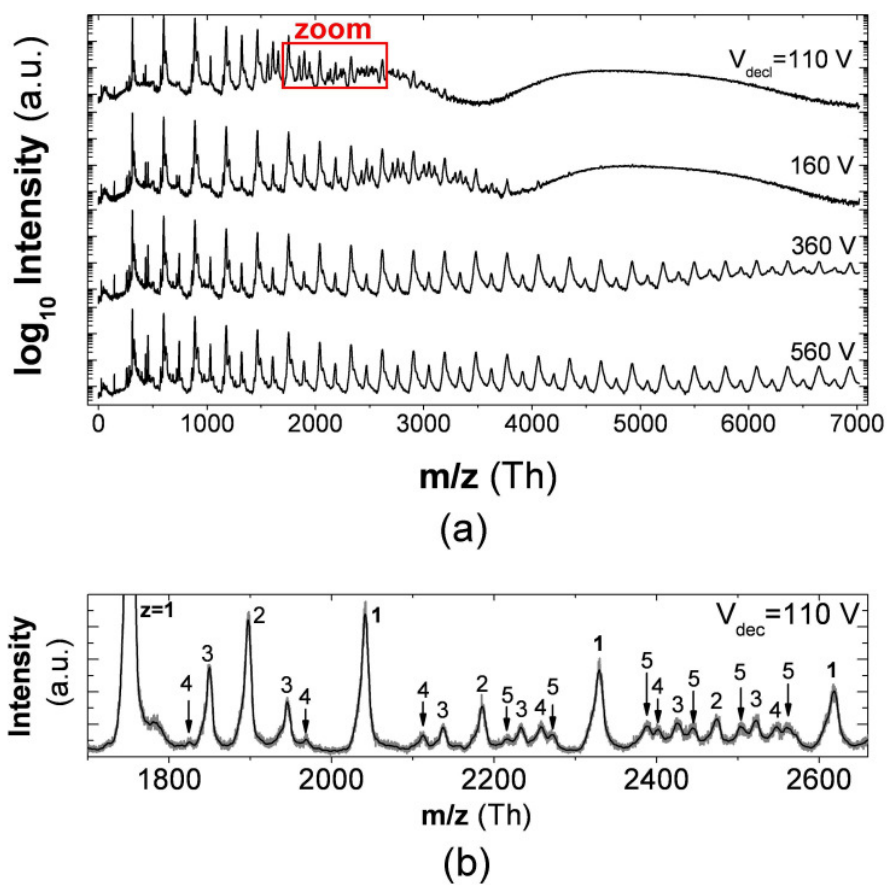


Figure 4.1: (a) ESI-TOF mass spectra of charged SDS clusters for various declustering potentials (b) a zoom-in spectrum for  $V_{\text{decl}} = 110$  V

background gas and break into lower charged smaller clusters. This agrees with the observation for the spectra at high  $V_{decl}$  where the lowly charged cluster peaks appear again in the  $m/z$  region up to 7000 Th. From this result it can be concluded that the ion beam can be created with a high purity, containing large highly charged SDS clusters.

## Matrix-Assisted Laser Desorption Ionization (MALDI)

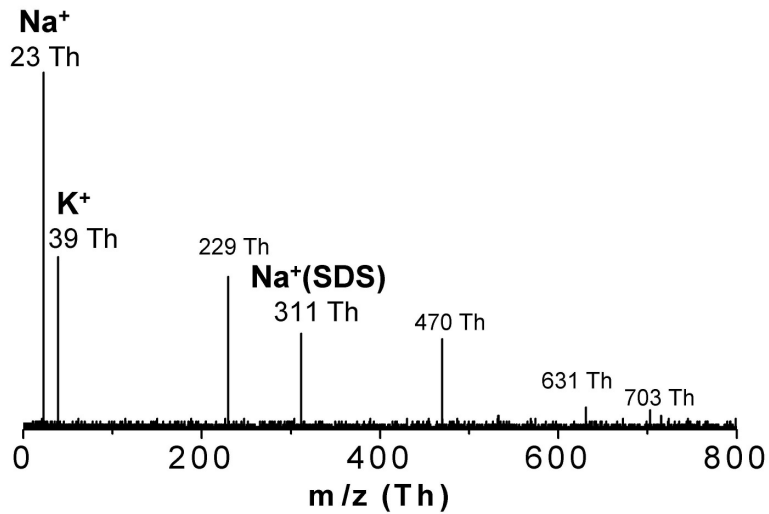


Figure 4.2: **LDI spectra of single-charged SDS clusters** deposited on Si surface by IBD at 28 eV incidence energy. The peaks at 23 Th and 39 Th corresponds to  $\text{Na}^+$  and  $\text{K}^+$ , respectively. The one at 311 Th belongs to the smallest cluster of  $\text{Na}^+(\text{SDS})$ . Other peaks could be originated from fragmentation of the clusters.

In order to check the integrity of SDS molecules after being soft-landed onto a surface, MALDI-TOF was employed to characterize the surface after deposition. No matrix molecules were used in this experiment (LDI). SDS was deposited on a  $\text{SiO}_x$  surface in high vacuum by IBD. The ion beam mainly contains SDS clusters of single charge along with small amount of those with double and triple charges in the  $m/z$  range of 500-3000 Th. After the deposition at the incidence energy of 28 eV, the sample was characterized ex situ by MALDI-TOF. Fig. 4.2 shows the LDI mass spectrum obtained from the surface characterization. Several peaks can be observed up to 800 Th. The first two peaks at 23 and 39 Th belong to  $\text{Na}^+$  and  $\text{K}^+$ , respectively. The peak at 311 Th corresponds to a single charged SDS with  $\text{Na}^+$  as charge carrier. Other peaks at higher and lower  $m/z$  range could result



from contamination or from laser excitation during desorption of molecules from the surface, by which many fragments could be created.

The appearance of the primary singly-charged clusters of SDS ( $Na^+(SDS)$ ) in the LDI spectrum confirms that the SDS molecules remain intact on the surface upon IBD at 28 eV incidence energy.

## 4.2 Crystalline Growth on Surfaces in Vacuum

### Structure Formation on $SiO_x$ and Graphite

To study the crystallization process in the absence of liquid, SDS clusters were deposited on  $SiO_x$  and on graphite surfaces by IBD in high vacuum. The SDS structures formed on surfaces by cluster ion beam deposition in high vacuum remain stable for several days with a slow evolution under ambient conditions. Therefore they can be studied by ex-situ AFM, which is performed immediately after deposition and after being kept for a few days in air.

All the AFM images shown here are obtained immediately after deposition. The surface characterization by AFM after exposure to air for a few days reveals larger domains of the same structures. However, the observed small shifts of the structure height could possibly be caused by the incorporation of water molecules from the surrounding.

Topographies of the modified graphite and  $SiO_x$  surfaces are shown in Figs. 4.3a, d and 4.4a, b, respectively. In both cases flat islands of  $3.7 \pm 0.4$  nm are observed with submonolayer coverage. These islands stack up with the same height to form higher layers at increasing coverage (Figs. 4.3e and 4.4c). The island sizes in the range of 50-500 nm are observed independent of coverage. The homogeneous size and density of the islands show that the ion beam is well-defined and only gas-phase SDS molecular clusters are deposited on the surfaces. The well-defined morphology of the island together with the presence of straight edges suggests crystalline ordering of the SDS molecules on the substrates. While this feature appears rather weak for  $SiO_x$  (Fig. 4.4b inset), it can be clearly observed in the case of low coverage for graphite (Fig. 4.5a). Elongated islands with two long parallel edges are the main observed feature. Additionally, the alignment of the islands on graphite shows three different directions related by  $60^\circ \pm 3^\circ$  with respect to one another (Fig. 4.5b). This indicates an anisotropic growth of the islands along the crystals' principle directions.

A different feature observed between the structures on graphite and  $SiO_x$  is the height of the interface layers. At low coverage on graphite the interface layer is only  $0.6 \pm 0.2$  nm high (Fig. 4.3b) and disappears at high coverage. On the other hand, this first layer on  $SiO_x$  has a height of  $3.0 \pm 0.4$  nm and is always present for all coverages.

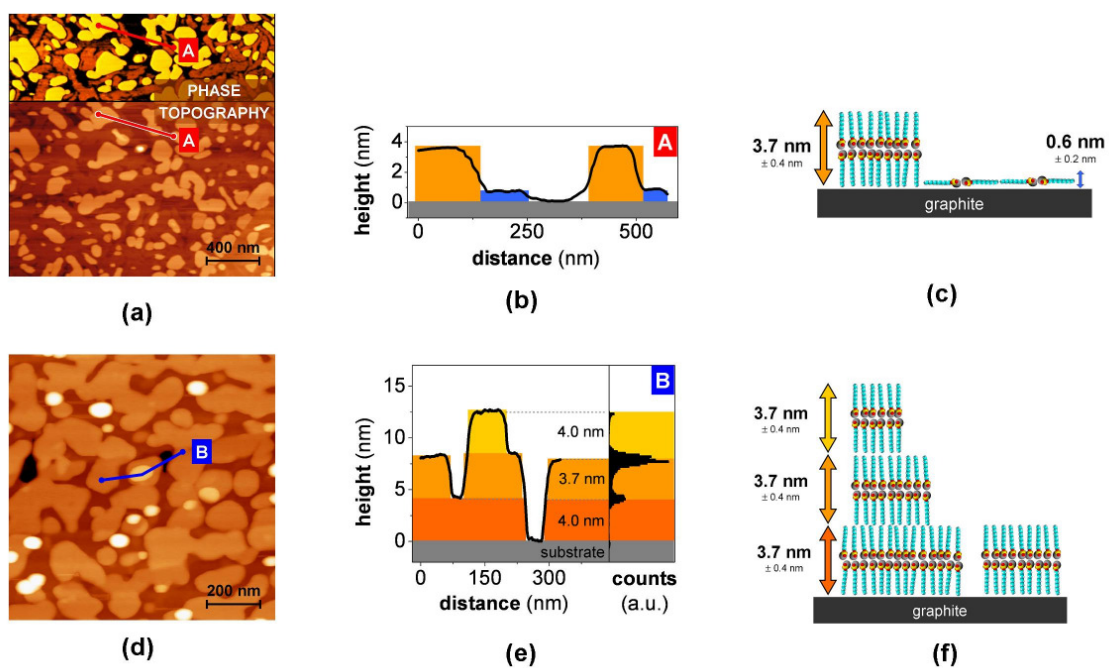


Figure 4.3: (a, d) AFM images of SDS on graphite by IBD in high vacuum, (b, e) line profiles of the structures marked by A and B, (c, f) suggested growth models corresponding to A and B

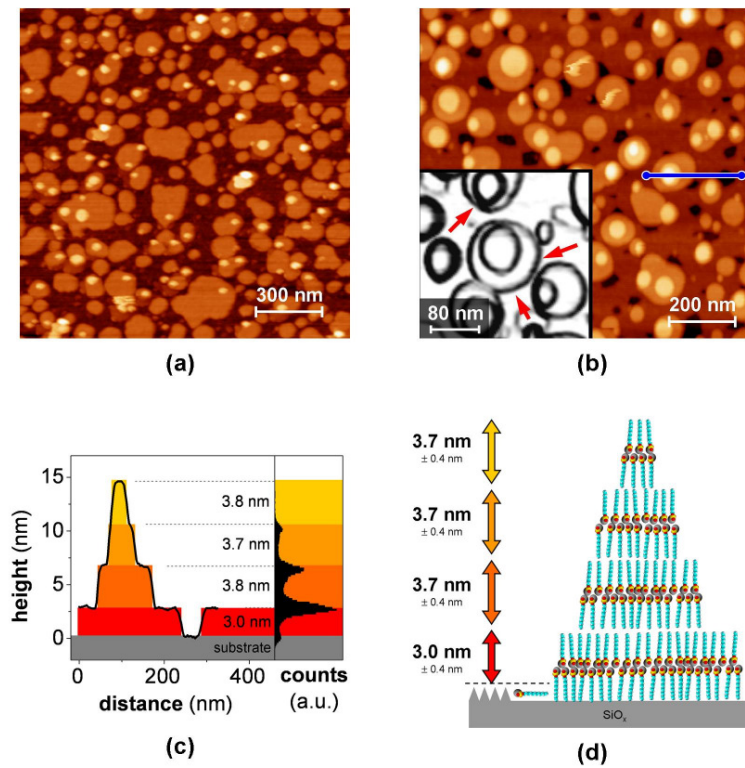


Figure 4.4: (a, b) AFM images of SDS on  $SiO_x$  by IBD in high vacuum red arrows in the inset marked crystalline edges, (c) line profile of the structure marked in (b), (d) suggested growth model

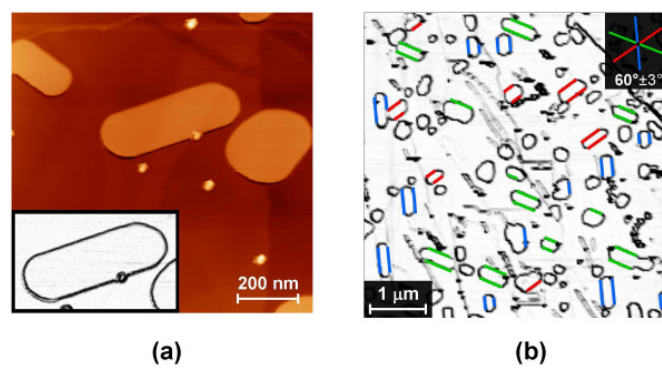


Figure 4.5: (a) AFM image of SDS on graphite by IBD in high vacuum, (b) orientation of SDS crystals on the surface in three different directions following crystals' symmetries of graphite.

In order to determine the molecular interactions and structure of the fabricated films it is useful to compare the morphology observed in AFM to the anhydrous forms of bulk SDS crystals grown from solution.[148, 149] All SDS crystals grown in solution are  $\{100\}$  platelets with alternating polar and apolar regions reminiscent of typical surfactant bilayers, where molecules are ordered in a head to head and tail to tail manner.[148, 149] The main axis of the molecules within each layer is oriented almost perpendicular to the  $\{100\}$  face resulting in approximately 3.8 nm spacing between the bilayers.

Two major binding forces responsible for the growth of SDS crystals are ionic/dipole occurring in the polar region, and van-der-Waals bonding occurring in the apolar region. The combination of these two forces results in a significantly lower surface energy of the metal-sulfate terminated  $\{100\}$  planes and therefore in the observed plate-like crystal morphology.

The size of the unit cell of SDS crystals measured by X-ray diffraction [150], which is approximately 3.8 nm, agrees well with the measured layer thickness of  $(3.7 \pm 0.4)$  nm on graphite and  $SiO_x$ . However, due to the absence of hydrophobic interaction in vacuum, the ionic/polar interaction dominates. Therefore, in contrast to a solution grown crystal with surfaces terminated by polar groups, an inverse bilayer configuration terminated by apolar chains is the more plausible model (Figs. 4.3c, f and 4.4d).

Compared to the bilayers the height of  $3.0 \pm 0.4$  nm of the interface layer on  $SiO_x$  is significantly larger than half, yet slightly lower than the full height (Fig. 4.4c). Since the morphology suggests a layered structure, the possible explanation for the molecular arrangement of this layer is a bilayer of molecules exhibiting reduced height. This could result from the roughness of  $SiO_x$  surface which is in the range of 1.0 nm, or from the presence of a closed monolayer of 0.6 nm height between the terraces, similar to that observed on graphite (Fig. 4.4d).

The interface layer of 0.6 nm height observed on graphite at low coverage can be interpreted as a crystalline structure formed by flat-laying double rows of molecules in a head-to-head and tail-to-tail manner, which agrees with the size of the unit cell.[148] In addition, coatings of flat-laying amphiphilic molecules are also well-known at liquid-solid interfaces and at surfaces in vacuum.[151, 152, 153] The detailed investigation of the flat-laying structure on Cu(100) will be discussed in the following.

## Crystal Growth on a Metal Surface in UHV

After the deposition of large SDS clusters on graphite and  $SiO_x$ , layers of upright standing molecules are observed, with the exception of a 0.6 nm thick layer in between the SDS submonolayer islands on graphite and on  $SiO_x$ . In order to further explore this possibility for the vacuum growth of SDS at the molecular level, SDS clusters was deposited on a Cu(100) surface in UHV for in situ analysis by STM. To avoid

a thick insulating film which can be difficult for STM characterization, only small clusters ( $m/z < 5000 \text{ Th}$ ) were mass-selected and deposited with a submonolayer coverage. The depositions were also performed on Au(111) and graphite surfaces but the molecules are too mobile and a stable STM images are difficult to obtained.

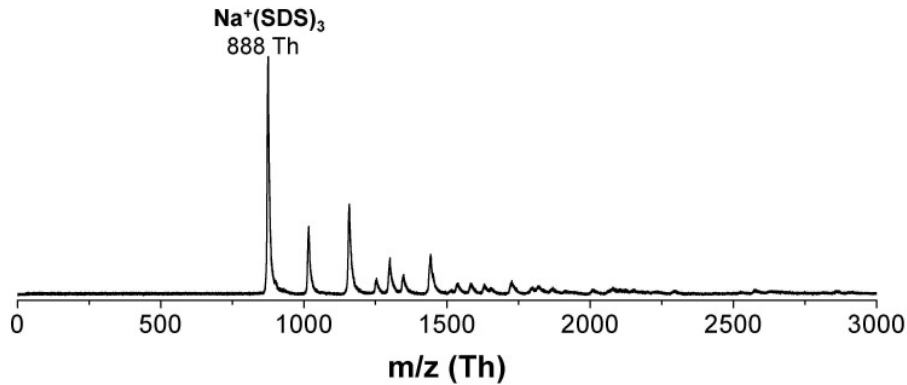


Figure 4.6: **ESI-TOF mass spectrum of charged SDS clusters ( $m/z < 5000 \text{ Th}$ ) contained in the beam for UHV deposition**

ESI-TOF was employed for beam characterization prior to the depositions. The obtained mass spectrum is shown in Fig. 4.6. Here, the SDS clusters with  $m/z$  below 880 Th and above 3000 Th was cut off. The strongest peak at 888 Th corresponds to the single-charged SDS cluster consisting of three SDS molecules and a  $Na^+$  as charge carrier. ( $Na^+(NaDS)_3$ ). Charge states of all the observed peaks are ranging from +1 to +4. The observed spectrum confirms that the beam contains only SDS clusters of the chosen sizes required for the deposition. The fluence for the deposition is 20 pAh which corresponds to 360 SDS molecules per area of  $100 \times 100 \text{ nm}^2$ . This leads to approximately 2% coverage.

After the deposition of the selected beam on Cu(100) surface in UHV, characterization of the modified surface was performed in situ by STM at room temperature and at 43 K. The topographic images obtained at room temperature are shown in Fig. 4.7 for a large scale (a) and a zoom-in (b). In Fig. 4.7a, thin parallel suppression lines are observed along two certain directions near step edges. While the lines along one direction can be more clearly observed and have a distance of approximately 4.2 nm between the adjacent lines, those along another direction appear in a weaker contrast. A zoom-in image displaying an area, where only the lines in the second direction are present, is shown in Fig. 4.7b. This allows to measure the distance between the adjacent lines, which are about 5-6 nm.

A similar characteristic compared to the observed structure were previously shown from the studies of the adsorption of SDS and a similar surfactant on surfaces by

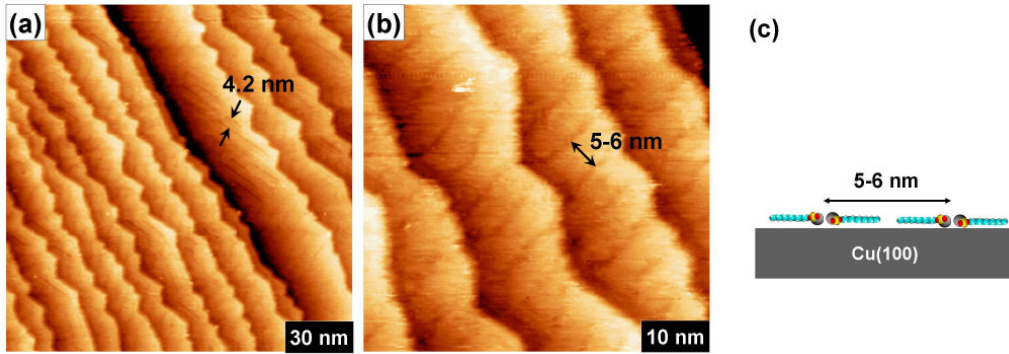


Figure 4.7: (a, b) STM images of SDS clusters on Cu(100) surface by IBD in UHV scanned at room temperature, (c) suggested growth model

electrochemical STM (EC-STM).[154, 155] Three rotational domains were observed from the adsorption of SDS on Au(111) electrode. [155] The width of the protrusion was  $5.0 \pm 0.4 \text{ nm}$ . The structure was proposed to be formed by an array of SDS hemimicelles. However, the growth phase was found to depend on the applied potential. At a graphite-solution interface, the same array morphology was reported.[154] The height of the protrusion was 0.1-0.2 nm, which is in a similar range to our observation. Due to the low height, formation of micelle structure is less probable compared to the geometry in which SDS molecules align horizontally on the surface. However, the observed distance larger than the SDS unit cell could result from the low packing density which is illustrated as a suggested model in Fig. 4.7c. This could be the result of different interactions and growth speed compared to the formation of bulk SDS crystals.

For the STM characterization at 43 K, a slightly different morphology was observed. Fig. 4.8a shows crystalline domains of flatly adsorbed SDS on the copper surface as a dark contrast, indicating the lower density of states of the molecular layer. Here the islands also have a characteristic elongated shape that indicates crystalline ordering of the molecules. On the two fold symmetric Cu(100) surface four growth directions are observed. Fig.4.8b displays a zoom-in image of the domain structure. Within one domain, a set of parallel protrusions is observed. The width of one protrusion is 3.7 nm. Fig.4.8c is a fourier transform of Fig.4.8b. The parameter  $d$  calculated from the fourier transform image represents the distance of a molecular double row as shown in the model in Fig. 4.8d, which also suggests the head-to-head and tail-to-tail configurations. This flat-laying molecular phase also support the interpretation of the 0.6 nm thick submonolayer phase on graphite (Fig. 4.3a-c).

The crystal growth of SDS by IBD in UHV allows characterization of the substructure in a different environment than previously studied. The results show that

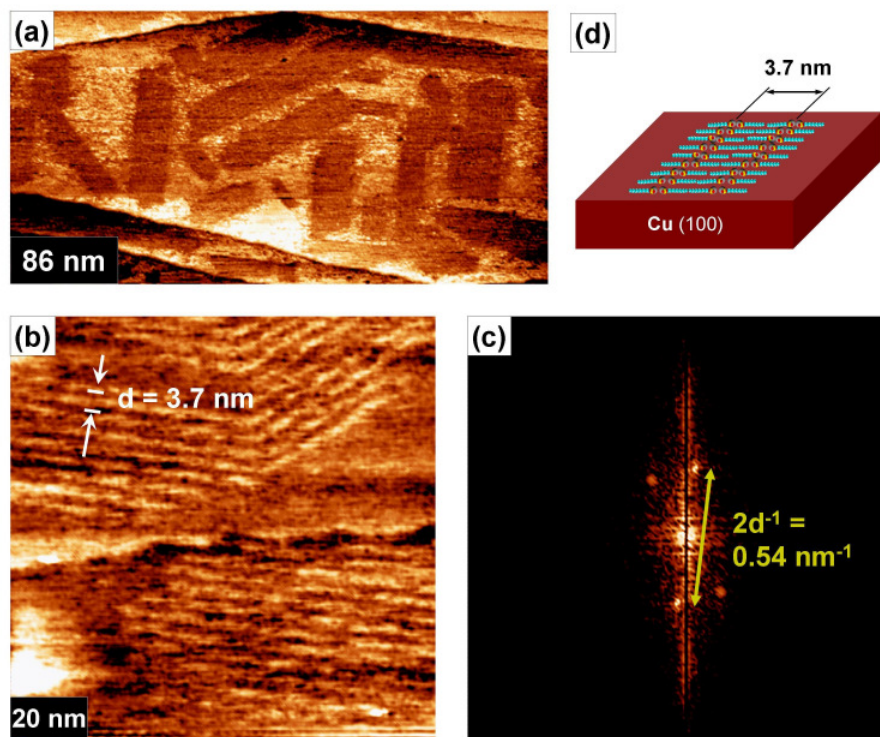


Figure 4.8: (a, b) STM images of SDS clusters on Cu(100) surface by IBD in UHV scanned at 43 K, (c) fourier transform image of (b), (d) corresponding growth model

crystallization, which leads to a homogeneous layer formation, is obtained despite the absence of liquid. The ability of SDS molecules to diffuse on the copper surface at room temperature could be accounted for the observed excessive distances of the double rows and the fuzzyness of the images. At 43 K, due to the limitation in the mobility of SDS, stable domains are formed and a molecular resolution is obtained.

Although the upright standing phase cannot be observed by STM characterization, its existence cannot be excluded. Fast tip degradation together with the fuzzyness of the images shows either the mobility of the molecules on the surface or the presence of a second phase.

### 4.3 Crystal Growth on Surfaces in Solution

Surfactant bilayer membranes made by liquid cast coating of SDS molecules from an aqueous solution are shown in Fig. 4.9. The liquid was deposited on  $SiO_x$  and graphite surfaces and the samples were blown dry in air before the AFM measurements at ambient condition. Fig. 4.9a, c show the modified surface morphology of  $SiO_x$  for low and high coverage. Fig. 4.9b, d display those for graphite.

Flat islands are observed on both surfaces. For  $SiO_x$ , the islands grow in random directions and the layer height is 3.0-3.7 nm. For graphite, at low concentration the growth follows crystal structure of the surface (Fig. 4.9b), while multilayers are formed inhomogeneously at high concentration. The first layer height is 1.6-1.9 nm and each of the upper layers is 3.7-3.8 nm high. The observed features for graphite resembles the growth of SDS on mica previously reported.[156] The inhomogeneous coverage was suggested to originate from the drying process. Since the molecules aggregate at liquid-air interface at a hydrophobic surface, the region which is dry later has high concentration of molecules, resulting in multilayer islands. Figs. 4.9e and f show tentative model of the molecular structure of SDS on both surfaces. On  $SiO_x$  a surfactant bilayer is likely to be formed, while on graphite a single layer of SDS with apolar chains adsorbed on the surface is more probable for monolayer coverage. Due to the variation in the observed height of the layers, SDS could form an upright standing or a tilted molecular arrangement, which would correspond to different degrees of incorporation of more molecules in the film.[148] The upper layer on graphite for high coverage could be formed by stacking up of surfactant bilayers, as observed for  $SiO_x$ .

The growth of SDS based on solution processing leads to inhomogeneous surface coating. The coverage as well as contamination level are difficult to be controlled. In order to achieve a clean homogeneously coated surface of well-defined coverage organic crystal layers, a surface preparation technique with more control is needed that is ES-IBD.



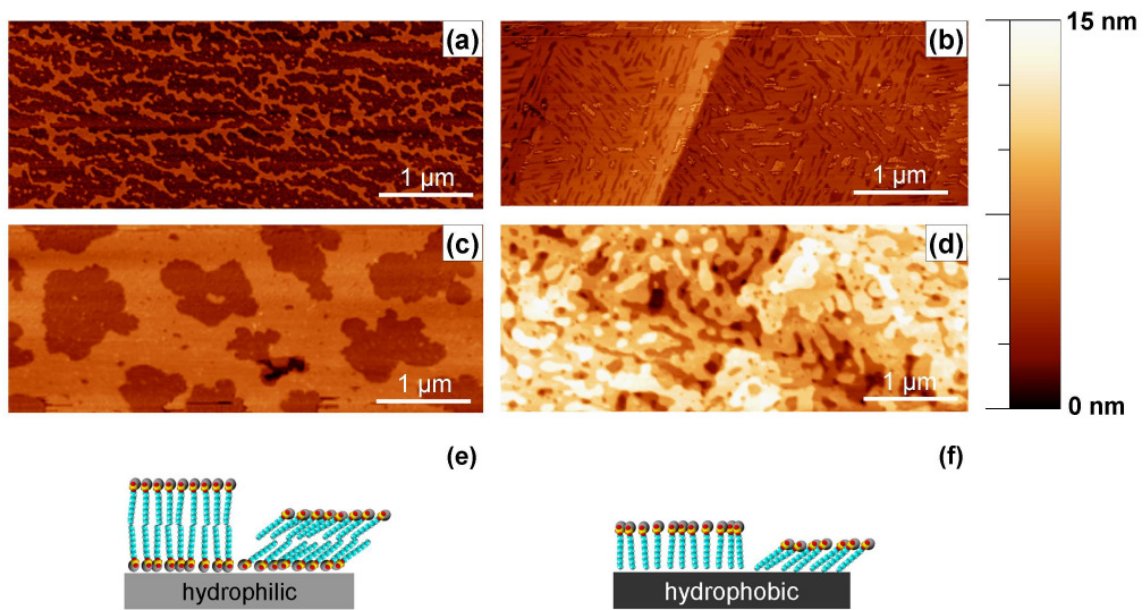


Figure 4.9: **AFM images of SDS clusters deposited on  $SiO_x$  (a, c) and on graphite (b, d) by liquid drop casting at low and high concentration.** Dendritic flat island is observed on  $SiO_x$ . On graphite, the island growth follows surface structure at low concentration and forms multi-layers with inhomogeneous coverage at high concentration. **(e, f) corresponding growth models** suggest surfactant bilayer on  $SiO_x$  and single layer on graphite with either upright standing or tilted molecular arrangement

## 4.4 Conclusions

The hierarchy of molecule-surface and intermolecular interactions strongly reflects on the morphology and structure of the SDS crystals on surfaces. The basic structural feature, which is a molecular double row results from the combination of strong attractive interaction between the sodium-sulfonate groups and weak interaction between the alkyl chains enforcing a stable head-to-head and tail-to-tail ordering. This structural feature is observed both in solution and in vacuum, and even dominates upon an increasing molecule-surface attraction from graphite to copper, which nevertheless leads to altered texture and morphology.

IBD of SDS clusters on  $SiO_x$  and graphite results in slightly different features of the first layer. While on graphite almost perfect horizontally laying SDS double rows are observed as the first layer in vacuum (Fig. 4.3c), on  $SiO_x$  surface without liquid environment more than one situation can account for the formation of the interface layer: the roughness of the surface and the presence of the flat-laying phase. Newly formed SDS surfaces only weakly interact with the next layers, which therefore preferably grow as SDS bilayers (Fig. 4.4d). Finally, the strongly adsorbed SDS molecules on the Cu(100) surface also show a head-to-head and tail-to-tail ordering in the form of a double row structure complying with hierarchical interactions that govern the self-organized crystalline growth of SDS.

The interaction of the polar  $SiO_x$  surface and the SDS molecule is strong in comparison to only weak binding forces that act on the double layer growing on top of the graphite surface or on a double layer of SDS terminated by aliphatic chains. The enhanced mobility on the graphite surface thus leads to a strong expression of the characteristic crystalline shape of SDS and to an epitaxial relation between the SDS layer and the graphite surface, as indicated in Fig. 4.5b. Moreover AFM tip-induced deformation of islands is observed as a consequence of the weak molecule surface interaction. On graphite, therefore, the AFM investigations had to be carried out extremely gentle, i.e. at low cantilever amplitude and with a high tip-surface distance. The strong molecules surface interaction between the sulfonate group and the  $SiO_x$  surface suppresses the diffusion and thus only in higher layers, weak signs of crystalline facets can be identified.

At last, also the soft deposition of large inverse-micelle clusters is influential to the structure formation. In this configuration the aliphatic chains point to the outside where they bind weakly to the substrate surface. We hypothesize that during deposition the adsorbed clusters are mobile as a whole and preferably fuse into larger islands of upright standing SDS molecules in an inverse membrane configuration.

In summary, ion beam deposition proves to be a suitable tool for the growth of crystalline molecular structures on surfaces. The deposition of SDS cluster ion beams on solid surfaces in vacuum resulted in stable films of material on the surface, which were observed by ex-situ AFM and in-situ STM. Inverted double-membranes

as well as a flat laying phase were obtained, all exhibiting characteristic features of crystalline ordering such as a constant layer thickness of 3.7 nm, low roughness, and characteristic domain shape. The hydrophilic-hydrophobic interaction is not present in vacuum environment, yet the hierarchy of bond strength given by the molecular structure of the amphiphiles leads to the growth of nanostructures that follow the head-to-head and tail-to-tail design principle of surfactants in aqueous environment.



## Chapter 5

# Grafting of Preformed Host-Guest Complexes

Host-guest interaction is one of the major fields of research in supramolecular chemistry, [157, 158, 46] and plays a fundamental role in many chemical and biological processes. Functional surfaces based on host-guest complexes are thus desirable for many applications, such as molecular recognition, ion sensing, heterogenous catalysis or molecular switching.[159, 160, 161, 162] Macrocycles are particularly attractive for the fabrication of templates with tunable functionality. The variety of shapes and chemical compositions characterizing the ring moiety and central ion allows for the fabrication of templates with properties that are tuned by the modification of the independent functional groups at the inner and outer sides of the macrocycle or by the exchange of the central ion.[163]

Crown ethers are an important class of macrocycles due to their highly selective ion-affinity which depends on the cavity size.[50] Ever since the development of supramolecular chemistry, research on host-guest interactions of crown ethers has been carried out extensively in solution [164] and in the gas phase [165]. At the solid-liquid interface densely packed crown ether layers were imaged with electrochemical STM.[166, 167]

Here, the host-guest interactions between a large crown ether, Dibenzo-24-crown-8 (DB24C8) and three different cations are investigated. Fig. 5.1 shows a structural model of DB24C8 and of the incorporated ions. Size comparison is given based on the diameters.

In situ Scanning Tunneling Microscopy (STM) is employed to study the complex structures deposited on a surface in UHV. Two different approaches were applied to grow the host-guest complexes on a surface. One approach is the co-sublimation of DB24C8 and cations by organic molecular beam epitaxy (OMBE), which is shown to be limited by the thermal stability of the complex. The alternative approach is to preform the complexes in solution and deposit them as gaseous ions on the surface

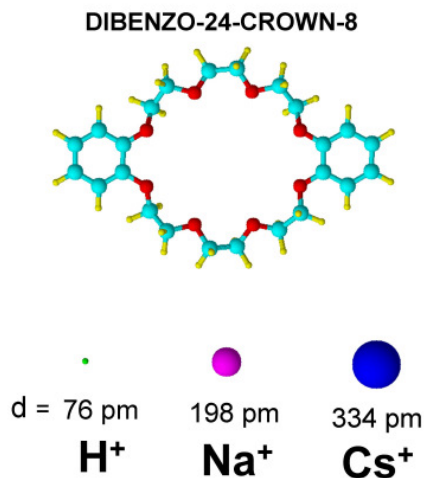


Figure 5.1: **Structural model of DB24C8 and of the incorporated ions** (diameter given).

by ion beam deposition (IBD).[36, 99] Time-of-flight mass spectrometry (TOF-MS) is employed to characterize the beam composition in situ prior to the deposition. Matrix-assisted laser desorption ionization mass spectrometry (MALDI-MS) is utilized for chemical characterization of the surface after the deposition to confirm the integrity of the deposited complexes. The structure of the formed complexes are observed by in situ STM. In addition, density functional theory (DFT) calculations are carried out to interpret the experimental results.

## 5.1 Limitation of Thermal Sublimation

DB24C8 and cesium are co-deposited to a surface using organic molecular beam epitaxy (OMBE) and a cesium dispenser in order to test the host-guest complex formation. As a reference, sublimation of DB24C8 alone is also performed to compare the behavior of the pristine DB24C8 molecules at the surface to that of charged cationic complexes.

The molecules were deposited onto an atomically clean Cu(100) surface. The sublimation temperature between 350 K and 400 K was applied for the depositions, while the surface remained at room temperature. The sublimation temperature is kept low to avoid the thermal decomposition of the molecules. For the same reason, the degassing temperature of the molecular source was set only as high as 400 K, resulting in an order of magnitude higher pressure ( $10^{-9}$  mbar) than usual in the

preparation chamber during the experiments due to additional degassing during the evaporation.

After the deposition, the Cu(100) surface is characterized by in situ STM. At room temperature, a stable structure is difficult to achieved due to the high mobility of the molecules at the surface. Therefore, cooling of the surface during the STM measurements is necessary. All the results from these experiments are obtained when the surface is cooled down to 43 K.

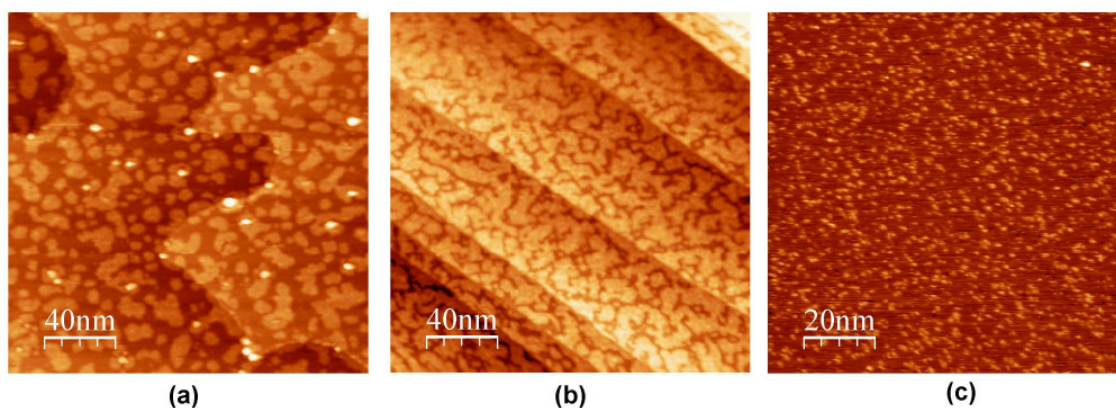


Figure 5.2: STM topographies of (a) DB24C8 evaporated on Cu(100) and (b), (c) after the co-deposition of Cs atoms for high and low coverage

Fig. 5.2 shows the observed structures on Cu(100) surface for three different experimental conditions. Fig. 5.2c shows the STM results from the co-deposition of DB24C8 and cesium at low coverage. In this case small islands with extremely high mobility are obtained. Even at 43 K no immobilized complexes are observed by STM. At higher coverage with (Fig. 5.2b) and without Cs atom dosing (Fig. 5.2a), unordered fractal structures are generally observed at the surface. Neither single molecules or complexes nor ordered domains could be identified. Added to that, the characteristics of the observed structures changed significantly throughout several experiments. The cleanliness of the surface is also difficult to control due to the high pressure (in the range of  $10^{-9}$  mbar) in the deposition chamber resulting in some additional big islands as in Fig. 5.2a.

Unlike IBD, where a beam characterization can be performed prior to the deposition, the status of the evaporated materials in OMBE cannot be obtained in situ. Therefore, it cannot be assumed that the molecules remain intact upon sublimation and adsorption. This means that in general the thermal processing of crown ether complexes is difficult due to limited stability and low evaporation temperature. The latter inhibits proper degassing of the evaporator and the purification of the com-

pound in UHV.

## 5.2 ES-Mass Spectrometry of Host-Guest Complexes

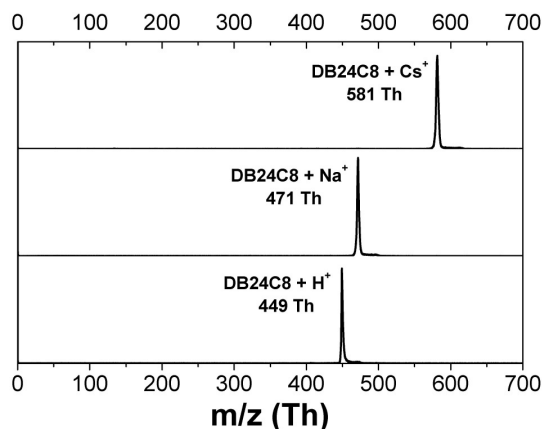


Figure 5.3: **ESI-TOF mass spectra of DB24C8- $Cs^+$ , DB24C8- $Na^+$ , and DB24C8- $H^+$  ion beams used for IBD**

Ion beams of three different DB24C8-cation complexes were prepared, characterized and deposited on a Cu(100) surface in UHV by IBD (see chapter 2). Before deposition the ion beam composition is characterized by the ESI-TOF. The incorporation of cations  $Cs^+$ ,  $Na^+$  and  $H^+$  in the complex was achieved by adding CsI, NaCl and formic acid to a solution of DB24C8. Mass spectra shown in Fig. 5.3 were acquired by a built-in time-of-flight (TOF) mass spectrometer prior to deposition to assure the purity of the beam. From top down, mass spectra of  $DB24C8 - Cs^+$ ,  $DB24C8 - Na^+$  and  $DB24C8 - H^+$  complexes are displayed, respectively. In each mass spectrum, only one dominant peak is observed. The corresponding  $m/z$  of the three peaks are 581 Th, 471 Th and 449 Th, which correspond to singly charged complexes of DB24C8 with one  $Cs^+$ ,  $Na^+$  or  $H^+$  ion as respective charge carrier.[168] The absence of any other peaks of significant intensity in the mass spectra indicates the high purity of the beams, i.e. only the desired complexes will be deposited on the surface.

## 5.3 Proof of Soft Landing by MALDI-MS

In order to confirm soft landing of the DB24C8-cation complexes upon IBD, ex situ MALDI-TOF was employed on samples prepared in high vacuum. (see chapter 2)



The  $Cs^+$  complex was chosen for this experiment because it can only originate from ion beam deposition. In contrast, the  $Na^+$  or  $H^+$  complex can be formed as well by DB24C8 with an  $H^+$  from a proton donor or  $Na^+$  contamination that unavoidable in ex situ characterization. DB24C8 –  $Cs^+$  ion beams were deposited at various incidence energies on a surface covered by 7, 7, 8, 8-Tetracyanoquinodimethane (TCNQ), which acts as a matrix.[124, 125] The integrity of the host-guest macromolecular complex, DB24C8- $Cs^+$  on the surface upon IBD was tested by MALDI. The effect of incidence energy on dissociation of the complex was studied. Incidence energies were adjusted to 5 eV, 36 eV and 56 eV for each deposition.

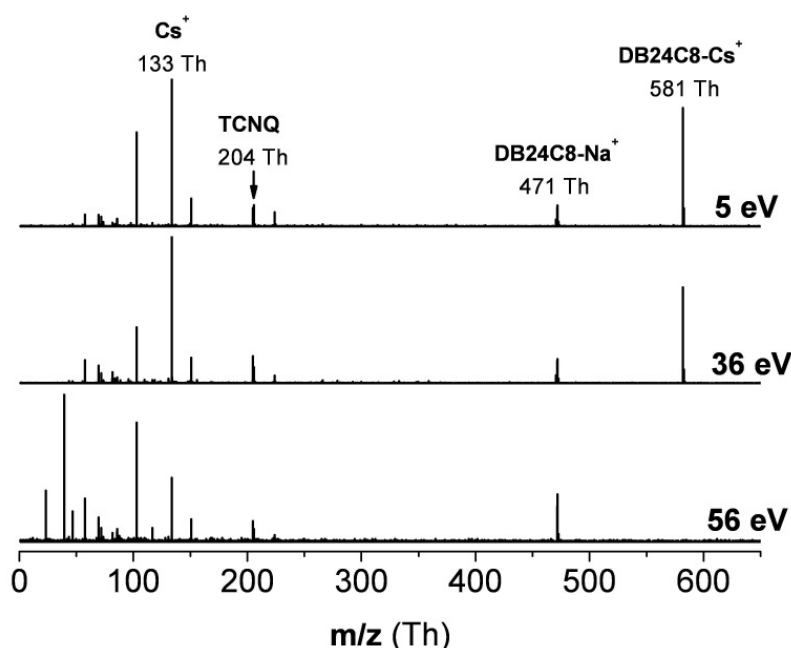


Figure 5.4: **MALDI-TOF mass spectra of DB24C8 –  $Cs^+$  complexes from IBD in high vacuum** at the beam energy of 5 eV, 36 eV and 56 eV. TCNQ (204 u) is used as a matrix. For 5 eV and 36 eV deposition energy the peaks at 133 Th, 581 Th and 471 Th can be identified as  $Cs^+$ ,  $DB24C8 + Cs^+$  and  $DB24C8 + Na^+$ . For 56 eV the peak at 581 Th disappears and additional peaks in the low  $m/z$ -range occur with high intensity.

Soft landing deposition can safely be assumed for a low deposition energy of 5 eV, set for all the IBD experiments in UHV, based on the experience obtained by many other experiments in our [99] and other labs [95, 129, 93, 135]. The presence of a regular feature for the majority of structures on the surface observed by STM (see Fig. 5.5) suggests that intact molecular complexes have been deposited to the

surface. However, at higher deposition energy the bonds within the complex can break and cause molecular disintegration.

Fig. 5.4 shows MALDI-TOF mass spectra for three different incidence energies. The peaks at 102 Th, 133 Th, 204 Th, and 471 Th can be observed for all spectra. The peak at 581 Th occurs only at the incidence energy of 5 eV and 36 eV. For 56 eV, the 581 Th peak is absent along with the rising of some additional peaks in the low  $m/z$  range.

The peak at 204 Th belongs to TCNQ, which is used as a matrix. Fragmentation of TCNQ due to laser irradiation results in a peak at 102 Th. The peak at 133 Th and 471 Th corresponds to  $Cs^+$  and  $DB24C8 + Na^+$ , while the 581 Th peak is attributed to  $DB24C8 + Cs^+$ , the original components of the deposited complex. The disappearance of the  $DB24C8 + Cs^+$  peak at 56 eV could be explained by disintegration of the complex upon collision at the surface. The increase in the intensities of some low  $m/z$  fragment peaks also supports this explanation. The excess of single  $Cs^+$  ions for 5 eV and 36 eV incidence energies could be caused by laser excitation. During the adsorption process, it is possible that some complexes lose their  $Cs^+$  counter ions and catch  $Na^+$  from the environment. Therefore, the  $Cs^+$  and  $DB24C8 + Na^+$  peaks are observed in the mass spectra even though they were not contained in the beam prior to the deposition. At 56 eV, the host-guest complexes could already be disintegrated at the surface by collisional-induced dissociation (CID) (see chapter 3). However, some remaining DB24C8 molecules were still capable of catching  $Na^+$  ions from the environment, expressed by the presence of  $DB24C8 + Na^+$  peak in the mass spectrum. The status of the DB24C8 molecules in this case cannot be determined. They could still remain intact or the rings could break open and some could be disintegrated into fragments.

It can be concluded from the observation that upon IBD at the incidence energy up to 36 eV, the host-guest complexes of large crown ether and cations remain intact at the surface. At high incidence energy of 56 eV, the complexes are disintegrated by CID.

## 5.4 Atomic Structures at the Surface

After deposition of a desired coverage of the complex in UHV, the Cu(100) sample was transferred in situ to the STM. Fig. 5.5 shows STM topographs obtained after cooling the sample to 43 K, whereas at room temperature the molecules were highly mobile and a well-defined molecular structure could not be observed. At low temperature the general feature observed for all three complexes is the presence of an oval-shaped structure of an apparent height of  $(1.8 \pm 0.2) \text{ \AA}$  with a lateral size of 12-15  $\text{\AA}$  along the short axis, and 16-21  $\text{\AA}$  along the long axis (see Fig. 5.5g). Long and short axis are defined by connecting the maxima of the submolecular features in the topography.

For the alkali ion complexes of DB24C8 with  $Cs^+$  and  $Na^+$ , molecular substructure consisting of four lobes is visible. Due to the fact that crown ethers are not shape-persistent, small variations in shape can occur, which is reflected in the observed distributions for the length of axes of approximately  $\pm 1.5$  Å.

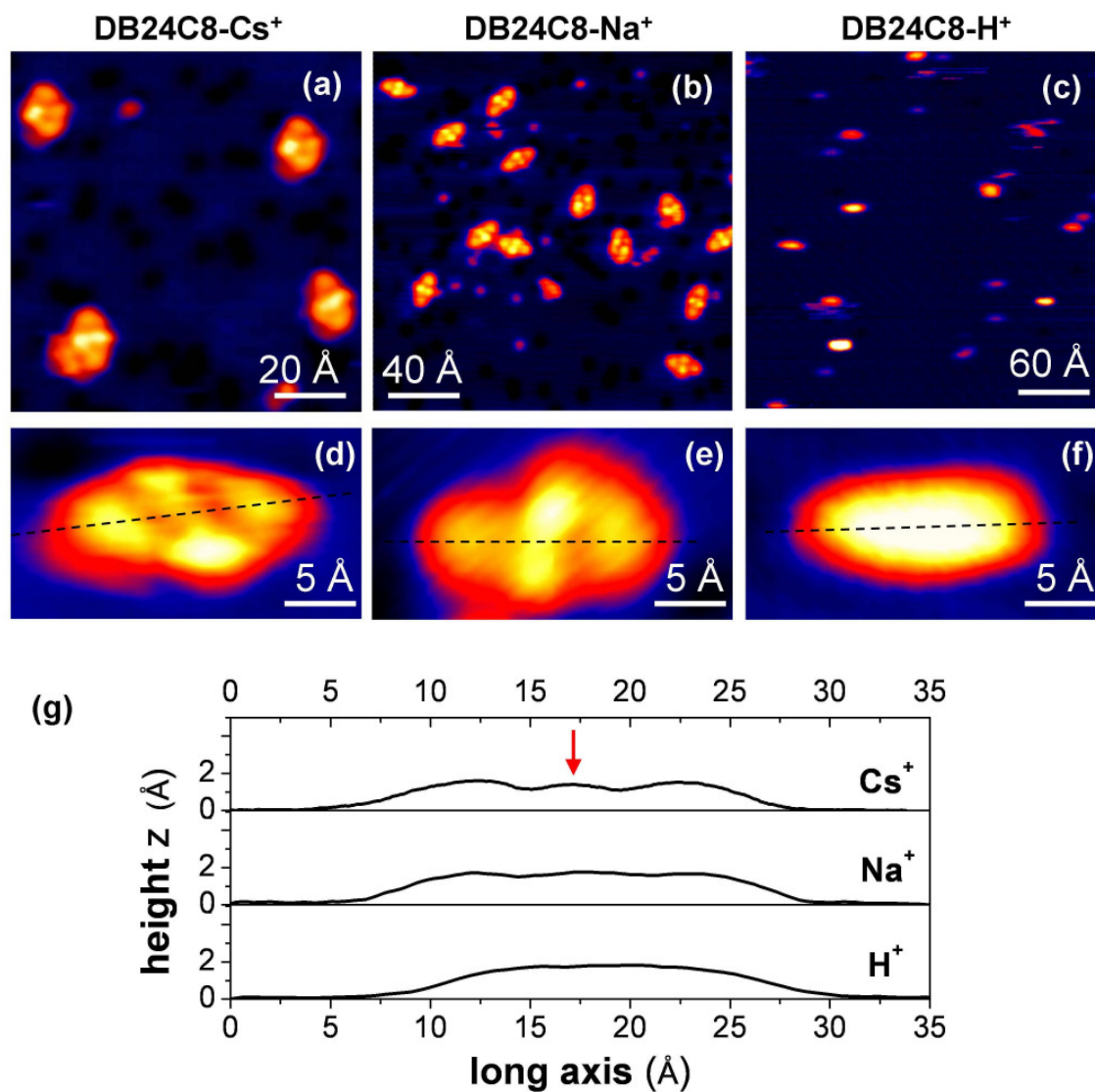


Figure 5.5: Overview and magnified single complex STM topographies of DB24C8-cations complexes on Cu(100) prepared by IBD (a, d) DB24C8 –  $Cs^+$ , (b, e) DB24C8 –  $Na^+$ , (c, f) DB24C8 –  $H^+$  (g) line profiles along the long axis displayed at an equal lateral and vertical scale

In the  $DB24C8 - Cs^+$  complexes (Fig. 5.5d) an additional bright feature in the center can be observed (red arrow in Fig. 5.5g). Also, one of the lobes on the short axis is typically found to be significantly brighter than the others. For  $Na^+$ , both lobes on the short axis are equally bright and their relative positions are very close. The structure appears to be more elongated than the  $Cs^+$  complex and an additional feature in the center cannot be observed.

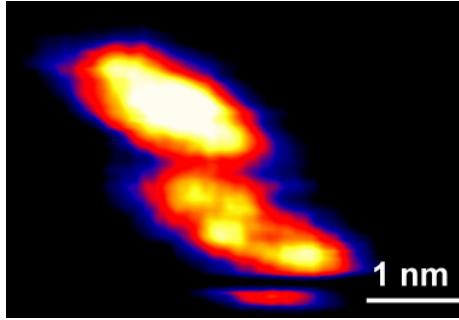


Figure 5.6: **an STM image of a Cu(100) surface deposited by  $DB24C8 - H^+$  ion beam** Four-lobe complexes similar to  $DB24C8 - Na^+$  are observed occasionally as contamination.

For  $DB24C8 - H^+$  complexes, a single bright lobe without any substructure is observed. Since the  $DB24C8 - H^+$  ion beam was occasionally contaminated by a small amount of  $DB24C8 - Na^+$  complexes, some STM topographs show 4-lobe features of the  $Na^+$  complex together with the single lobe structures that correspond to the  $H^+$  complex, proving that the absence of an internal structure in the  $DB24C8 - H^+$  complexes is not due to poor STM-tip condition (Fig. 5.6).

Apart from the main observed structures, some dark hollows and small spherical islands, which can be seen in Fig. 5.5a and b are also present on the surface. The hollows could be attributed to the oxygen vacancies, which generally appear when the surface has been left in the chamber for a certain time.[169] The small spherical islands, which occur mostly in the case of  $DB24C8 - Na^+$  complex, could be originated from parts of the disintegrated structures or contaminations due to a long deposition time. Since  $Cs^+$  fits better in the cavity of DB24C8 than  $Na^+$ ,  $DB24C8 - Na^+$  complexes are less rigid and have more flexibility to move, thus the higher amount of defect structures for  $DB24C8 - Na^+$  can be expected.

In order to interpret the observed structures after ion beam deposition, theoretical modeling of the DB24C8-cation complexes, adsorbed at the surface, was carried out from DFT-based calculations (see Appendix i). The obtained adsorption geometries for the  $DB24C8 - Cs^+$ ,  $-Na^+$  and  $-H^+$  complexes are illustrated in Fig. 5.7. For the most stable structures of the adsorbed DB24C8 complexes, STM images were

computed by integrating the density of states between the bias potential (-1.3 eV) and the Fermi energy, following the Tersoff-Hamann approach. [170, 171] A comparison of the resulting images at a tip height of about 1.2 Å above the molecule is shown in Fig. 5.7.

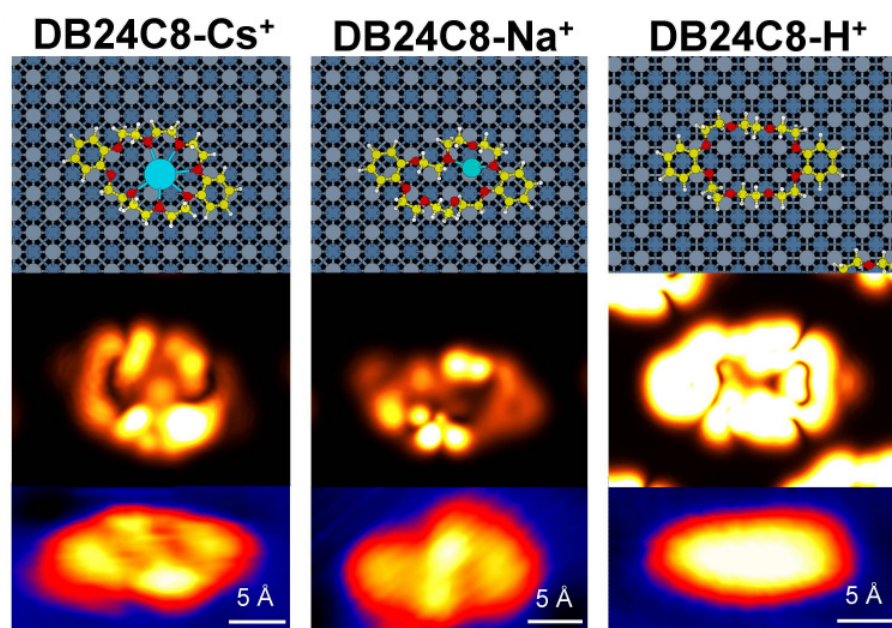


Figure 5.7: (top row) **Geometry of the DB24C8 complex at the Cu(100) surface**  $DB24C8 - Cs^+$ ,  $-Na^+$  and  $-H^+$  from left to right (middle row) **Simulated STM images** according to the above structures (bottom row) **Magnified STM topographs of single complexes**

The images reflect the DB24C8 geometrical structure, with the benzene rings located at the edges of the longer axis. Due to their vicinity to the surface they are imaged as fainter areas in contrast to the lifted ether chains, which in turn give rise to the bright spots near the center of the structures. The  $Cs^+$  complex exhibits a centrosymmetric disposition of the bright lobes, with one brighter side corresponding to a higher position of the ether chain. The  $Na^+$  complex displays an S-shaped pattern with the central lobes having comparable intensity. In the sodium complex the resulting structure is strongly asymmetric. The folding of one side of the chain towards the center of the ring leads to an S-shaped central cavity. The corresponding STM image appears more elongated than the one for the cesium complex which shows a more compact, oval-shaped conformation. The simulated images also differ in the middle of the cavity region, where the ion is located. While  $Na^+$  is virtually not

imaged, the larger  $Cs^+$  is mapped as a light spot in the center of the simulated image.

Based on the good agreement between the experimental and theoretical STM images, the calculations strongly support the experimental evidence of complex formation between alkali ions and DB24C8 via coordination around the central cavity. The absence of self-assembled domains as well as the results from the DFT calculations suggest that the complex, which has been deposited as an ion, retains its positive charge.

Depending on the size of the ion and its interactions with the host molecule, the location of the ion inside the ring cavity and the morphology of the complex vary. In the STM topographies the size of the central cavity is found to scale with the size of the ions, i.e.  $Cs^+ > Na^+$ , in particular for  $H^+$  the substructure cannot be observed.

The most stable adsorption geometry for the  $DB24C8 - Na^+$  complex suggests that the  $Na^+$  ion is coordinated to four oxygen atoms near one of the two benzene rings. For the  $DB24C8 - Cs^+$  complex the alkali center is coordinated to six oxygen atoms. The proton in the  $DB24C8 - H^+$  complex was found to hardly affect the adsorption geometry and the consequent STM imaging. Nevertheless, its presence in the complex at the surface is indicated by the different behavior of the  $DB24C8 - H^+$  (Fig. 5.5c) complex compared to evaporated DB24C8 (Fig. 5.2a).

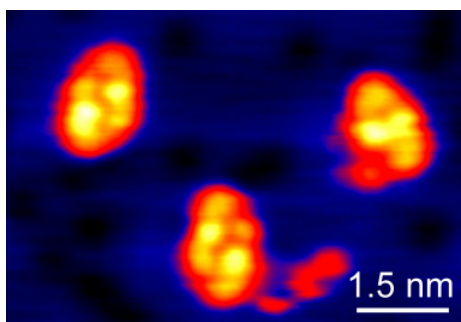


Figure 5.8: **Two uncommon structures found for the  $DB24C8 - Na^+$  complexes** compared to a regular 4-lobe conformation

For a large molecule many conformational states of similar adsorption energies are expected. In the experiment a few structures with small differences in shape compared to those most commonly observed were found for  $DB24C8 - Na^+$  complexes (Fig. 5.8). DFT calculations show that the potential energy surface for the adsorbed systems is relatively flat, as witnessed by the presence of numerous local minima within less than 0.1 eV. This gives rise to many possible orientations on the surface and small deviations in shape. Minima on the potential energy landscape differ by small displacements of the metal center or parts of the organic ring with respect to

the Cu(100) surface. While the main bonding occurs via chemisorption of the alkali ions, the rest of the complex is less interacting with the copper and consequently retains some degrees of freedom. Strong deviation from the typical shape as shown in Fig. 5.8 might result from catching additional guest atoms in the cavity since  $Na^+$  does not fill it entirely. This could also explain why such uncommon structure is not observed in the case of  $DB24C8 - Cs^+$  complex, where the guest ion fits well in the cavity.

Physisorption of pure DB24C8 on Cu(100) is mostly affected by the interaction of the benzene rings with the metal surface. The well-known inadequacies in the DFT description of Van-der-Waals-interactions prevent a detailed analysis of the adsorption mechanism, which is however estimated as being exothermic for about 0.2-0.3 eV. The coordination of an alkali ion into the DB24C8 instead results in a much more favored adsorption on Cu(100). The adsorption energies for the  $DB24C8-Na^+$  and  $-Cs^+$  complexes were calculated as 1.17 eV and 1.72 eV, respectively. Compared to the value for DB24C8 alone, this explains the experimental evidence of a significant difference in mobility between the coordinated and uncoordinated crown ether.

## 5.5 Conclusions

Crown ether complexes, which are large and fragile functional molecular systems, were successfully deposited on a surface by means of ES-IBD, where conventional sublimation processes failed to produce reproducible results. In particular, the fabrication of crown ether complexes at the surface by co-evaporation of the constituents proved to be erratic, indicating that no well-defined surface modification is achieved.

ES-IBD, on the other hand, is able to pre-produce the desired complex by mixing its constituents in solution under ambient conditions, and deposit it onto the surface in UHV in a well-defined way. Beam-characterization prior to the deposition indicates the high purity of the beams containing only the desired complex species. Low energy deposition under soft landing condition keeps the complexes intact at the surface as confirmed by ex situ chemical analysis.

Structural investigation by STM at 43 K with submolecular resolution allowed to identify the type and conformation of the complexes, which was confirmed by DFT calculations. It is found that the crown ether is adsorbed flat on the Cu(100) substrate, with the cation placed within the cavity. Substructure of the complexes can be observed when alkali ions are incorporated in the complexes. DFT calculations show that the deposition as preformed complex by IBD enables a strong binding to the surface. Moreover, the charge of the molecular complex is retained after deposition. In order to deposit three different complexes, the same methodology can be applied while the only difference in the procedure is the preparation of the solution.





# Chapter 6

## Folded and Unfolded Proteins in UHV

### 6.1 Introduction

Proteins are highly complex biological polymers, which are composed of a fixed sequence of amino acids. Their function is directly related to their conformation, into which they fold by self assembly in their natural environment. In living systems proteins can act as catalysts, transporters, storage for other molecules, provide immune protection, generate movement or transmit nerve impulses.[172] Due to the complexity of the protein molecule and its microscopic dimensions, it is a challenging task to understand the processes involved in its functions. Since proteins operate on the single molecular level, analysis at this resolution is required.

Mass spectrometry provides one of the most powerful tools for protein characterization and identification, since the mass of a protein as well as its amino acid sequence can be precisely determined.[173] ESI- and MALDI- mass spectrometry are techniques commonly employed for this task.[174, 175] The mass spectrometry approach allows also limited access to the three dimensional protein structure by combining it with cross section measurements in ion mobility spectrometers.[176] More precisely, the three-dimensional protein structures can be measured by X-ray crystallography of protein crystals [177, 178], while NMR spectroscopy reveals the structure of protein assemblies in solution.[179, 180] Additionally, advanced computational methods are often used to support these results.[181, 182]

X-ray crystallographic structures of large biological entities such as ribosomes have also been extensively investigated relating to their functions, leading to the Nobel prize in chemistry in 2009. In the last decade, a resolution of a few Angstrom was achieved for the ribosomes' structures.[183, 184] An approach to combine cryo-electron microscopy with the diffraction technique to obtain a high structural resolu-

tion had also been shown earlier.[185]

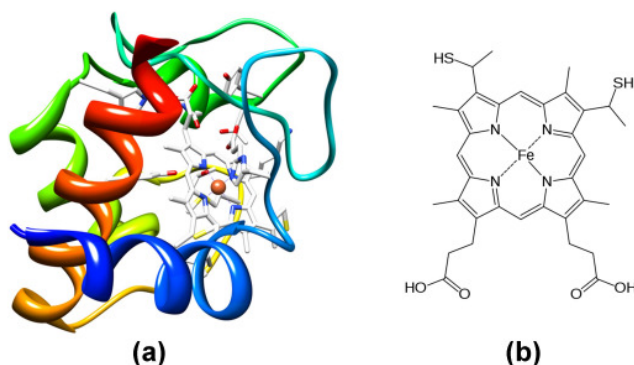


Figure 6.1: **(a) Structure of horse heart Cytochrome c** (Resource for Biocomputing, Visualization, and Informatics at the University of California, San Francisco), **(b) heme c**

The various, highly resolving investigation techniques summarized here are always probing a manifold of identical proteins. The analysis of proteins by scanning probe techniques is unusual and rarely carried out on the individual molecule at submolecular level. One reason for that is the difficulty in sample preparation. An approach to characterize an array of nanoparticle-protein complexes on a surface fabricated by micro-contact printing has been carried out recently by STM.[186] Electrical detection was performed through the tunneling current for a quantitative analysis of the biological binding events. In order to achieve submolecular-resolved complex structures by STM, vacuum deposition of the single proteins on surfaces is favorable.

To bring proteins softly into vacuum, ESI can be employed. One of the main reasons for the success of this technique is that proteins can generally be transferred intact into gas phase by this process.[111] A combination of ESI and soft-landing techniques was used to study the mass-selected deposition of a protein microarray. Mass spectrometry of the rinse solutions from the deposited proteins shows a set of results matching the mass of the initial compounds and biological activity was found for the redissolved proteins.[96, 187] Previous work from our lab showed that proteins can be deposited to clean surfaces by ES-IBD and retain a globular shape.[188]

In this study, ES-IBD together with in situ mass spectrometry and STM are employed for the surface deposition and characterization of proteins in UHV. In principle, the structure and conformation of single proteins on surfaces can be explored by STM with submolecular resolution. As a result chemical interactions of individual proteins can be monitored in vacuum. For instance, the complex behavior of proteins and the interactions at the surface could lead to conformational change or ordering.

Additionally, an attempt is made towards the understanding of protein stability in vacuum influenced by external parameters, such as elevated temperature or impact energy upon collision at the surface. In general, for proteins to function properly, their native conformation has to be maintained. Due to the close relationship between the conformation and function, the study of protein conformation is an important step to understand the biological process behind the complex functionality.

Positive ion beams of proteins are created from electrospraying aqueous solutions containing the proteins. Whether folded or unfolded conformations are deposited is controlled by the pH value of the solution and mass selection of low- and high- charge states respectively. Time-of-flight (TOF) mass spectrometry is used to characterize the beams chemically before deposition and to monitor the mass selection. The beam is deposited on surfaces prepared in an adjacent UHV chamber right before the deposition (see chapter 2). After the deposition the samples are transferred in situ into the STM, where they are measured at room temperature or 40 K.

The protein which is investigated in this thesis is Cytochrome c (CytC), a heme containing protein, consisting of 104 amino acids (AAs) adding up to a molecular weight of 12,384 Da. It has been investigated widely with regard to its function and conformation under physiological conditions [189], as well as its behavior in the gas phase by electrospray mass spectrometry [190, 191]. CytC is particularly interesting since it is central to several processes in electron transfer and apoptosis.[192] Oxidation and reduction occurring at the iron center of the heme complex are responsible for the main function of CytC in the electron transport chain.

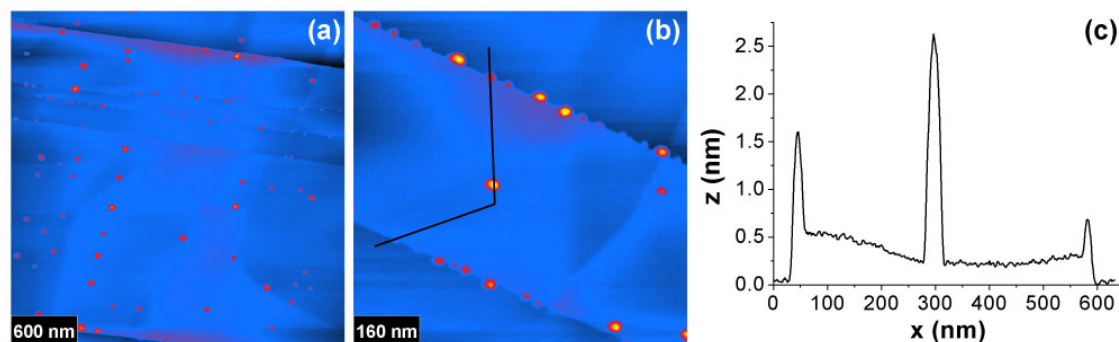


Figure 6.2: (a, b) AFM images of CytC deposited on graphite by IBD in high vacuum, (c) line profile across the structures as marked on the image. Globular islands of several sizes can be observed on the surface.

Vacuum depositions of proteins bovine serum albumin (BSA) were previously carried out in our laboratory.[188] Topographic analysis of the surface by AFM revealed homogeneously adsorbed patterns on a clean surface. For CytC, AFM investigation

was carried out prior to STM analysis to check the feasibility of the experiment and the cleanliness of the modified surface *ex situ*. In Fig. 6.2a and b, the results of the AFM characterization of the vacuum deposition of CytC on graphite are shown. Globular islands of diameters between 10-85 nm and height between 0.4-2.4 nm can be observed on the otherwise clean surface. Fig. 6.2c displays the line profile across the structures marked in Fig. 6.2b. According to this result, a clean, protein-coated surface can be achieved by ES-IBD allowing a scanning probe technique to be utilized for structural characterization. A direct visualization of single proteins or even sub-molecular resolution cannot be achieved by AFM in atmosphere, and thus the more advanced analysis, that is UHV-STM, is required.

## 6.2 ES-MS of Folded and Unfolded Proteins

Denaturing of proteins is the change of their conformation from the folded to an unfolded structure (see chapter 1). The denaturing of proteins can be induced by various external parameters, e.g. temperature, mechanical stress or pH value of the surrounding. Two CytC solutions with different pH values were prepared for ESI-TOF mass spectrometry by adding different amount of formic acid (FA) to the electrospray solutions. ESI charges proteins by attaching multiple protons, a process, which can be enhanced by acidifying the solution.[193]

Fig. 6.3 shows ESI-TOF mass spectra from two types of CytC solutions. The spectrum in Fig. 6.3a was obtained when 0.1 % acid was added to the CytC solution. The peaks appearing in the  $m/z$  range between 1000-3000 Th correspond to charge states between +5 to +12 (blue curve). After 5 % formic acid was added to the solution, the characteristic dark red color of the solution vanishes, indicating protein denaturation. The peaks in the mass spectrum (Fig. 6.3b) shift towards lower  $m/z$  range, revealing charge states up to +20 (red curve). The measured mass of  $12,385 \pm 6$  Da confirms the intactness of the CytC molecules.

The decrease in the pH value by adding acid to the solution results not only in an increased beam current, but also the observed charge per molecule increase. The relation between the charge state of the gas phase ion and the conformation of the protein, has been intensively studied for CytC by ion-neutral collision cross section measurements and H/D exchange dynamics.[191, 194, 195] The results suggest three main conformational states: Unfolded proteins preferably form high charge state ions ( $z > 10$ ), while folded and partially unfolded proteins are found in low charge states ( $z < 8$ ). Consequently, ES-IBD offers a way to prepare ion beams of a defined protein conformation by  $m/z$ -range selection of the corresponding charge states, enhanced by adjusting the FA concentration.

To investigate the structures of folded and unfolded proteins, two distinctly different CytC ion beams were prepared for deposition from the solution containing 0.1 %

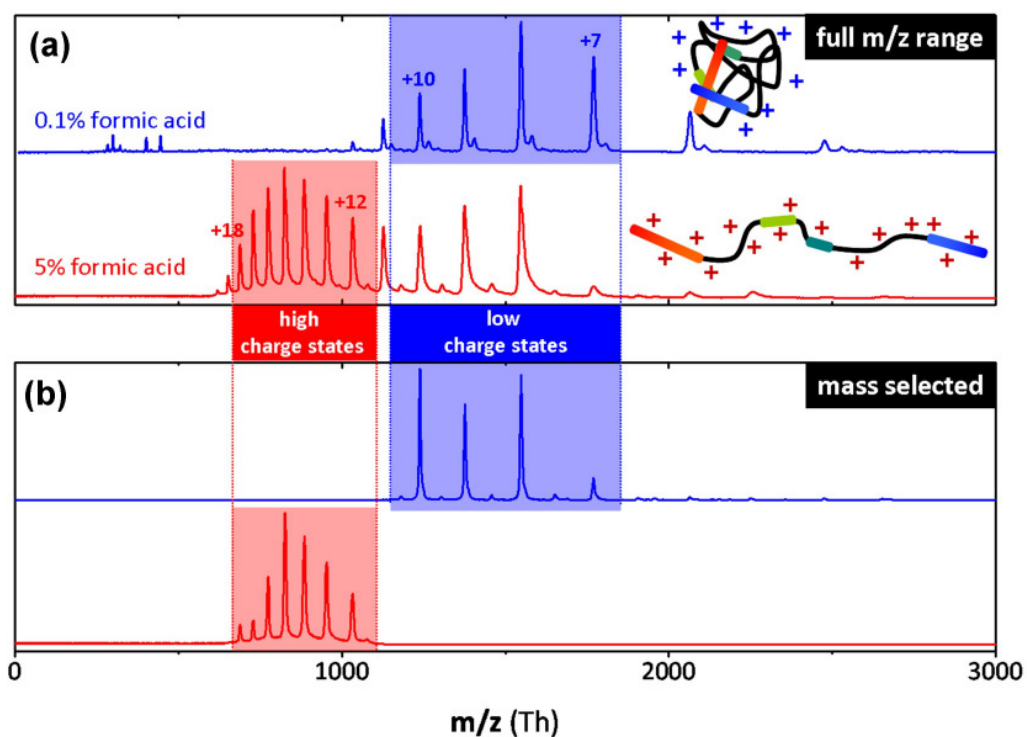


Figure 6.3: **ESI mass spectra of equine cytochrome c** from a  $H_2O/MeOH$  solution containing 0.1 % (blue) and 5 % (red) formic acid. **(a)** without mass selection low charge states from +5 to +12 are found for low FA concentration. High charge states up to +20 are observed for high FA concentration. **(b)** Mass selection of high ( $z = +12 - +18$ ) and low ( $z = +7 - +10$ ) charge states yields beams that contain preferably unfolded or folded protein ions, respectively.

and 5 % formic acid. A small amount of acid increasing the  $H^+$  concentration in a solution is often helpful to increase the ion beam current, however, it has to be limited in order to prepare a solution containing folded CytC. Ion beams of high and low charge state were mass selected in the ranges of 600-1200 Th ( $z = +12 - +18$ ) and 1250-2000 Th ( $z = +7 - +10$ ) with a quadrupole ion guide in addition to the adjustment of the pH-value (see Fig. 6.3b). At the target in UHV deposition currents of 15-60 pA can be achieved, which relates to a deposition time of 0.5-3 hours for a submonolayer coverage of 5-20 % of the surface area.

The results of mass spectrometry of CytC shows that different types of ion beams can be prepared. The beam components vary, when adjusting influential parameters such as pH value of the electrospray solutions. In the following, the influence of the gas phase conformation on the morphology of CytC deposited on different surfaces is studied.

### 6.3 Folded and Unfolded Proteins at Surfaces

The interaction with the surface plays an important role for the assembly and structure formation of adsorbate molecular layers. Since proteins contain many different functional groups, it is possible that their specific interactions with different surfaces influences the mobility and thus the molecular structure and arrangement. To investigate the structure of proteins after IBD, the two prepared ion beams (mass spectra in Fig. 6.3b) were deposited on surfaces in UHV. In situ STM characterization was carried out directly after the deposition.

Low charge state, folded CytC beams were deposited on three surfaces: Cu(100) is a strongly interacting surface, on which the molecules are expected to be fully immobilized already at room temperature. Au(111) is less interactive except at the elbow sites of the reconstruction [196] that can act as pinning centers. Finally the boron-nitride nanomesh (BN), an insulating monoatomic BN layer on Rh(111), interacts weakly, yet offers a regularly modulated surface of approximately 2 nm pitch, which can serve as a template for ordering.[197]

Figure 6.4 shows the three surfaces after the deposition of a submonolayer coverage of low charge state, folded CytC ions. On all surfaces two types of structural features can be distinguished: i) high, globular structures of 1.0-1.8 nm height with lateral dimensions of 2-4 nm, and ii) low height, string-like features (on Cu and BN) or patches (on Au) with a height of 0.2-0.3 nm (see line profiles Fig. 6.4d). It is evident, that the strings found on Cu(100) and BN correspond to unfolded protein strands, on Au(111) agglomerated into a compact patch. The globular features resemble the shape and size of the three-dimensionally folded protein,[198] taken into account the limitations imposed by the STM method. Here in particular, large organic structures appear less high due to a lower electronic density of states as compared to the metal,

while the lateral dimensions of high aspect ratio structures are overestimated due to the convolution with the tip shape.

The interaction of the folded protein with the surface does not induce unfolding. This is indicated by the observation of a similar ratio of folded and unfolded proteins on all surfaces and confirms the observation of former protein soft-landing studies that observe enzymatic activity after soft landing.[96, 199] The observed features can thus be rationalized by the configurations illustrated in Fig. 6.4e. Since the ion beam of low charge state CytC contains folded as well as partially and completely unfolded proteins,[191, 195] globular features of heights above 1 nm will be observed, when a folded or partially folded protein is present, while the features of 0.25 nm height correspond to unfolded proteins, that appear isolated as strands or patch-like agglomerations. Partially unfolded proteins are imaged as a mixture of flat and globular structures in the vicinity of each other.

Even though the surface does not induce unfolding, it has a distinct influence on the distribution of the deposited material. Measured at room temperature, on Cu(100) only minor step edge decoration is observed, which indicates that diffusion is inhibited and thus the molecules stick where they landed. On the less interactive Au(111) and BN surfaces measurements have to be performed at low temperature 40 K to reduce the surface mobility enough to observe individual proteins. Consequently, the step edge and the elbow sites of the reconstruction act as a pinning centers on Au(111), where folded and unfolded molecules are attached. The surface mobility also accounts for the observation of the compact patches as discussed in detail later. In contrast to Au(111), the BN nanomesh reconstruction provides a template of much smaller length scale, trapping the molecules on the terraces and moreover limiting the free motion of the unfolded protein strands, which hinders the formation of compact patches.

Agglomerations of globular features observed on Au(111) and Cu(100) suggest a higher surface mobility for folded as compared to unfolded proteins (see inset of Fig. 6.4a). Intuitively, the smaller contact area of the surface with a folded protein rationalizes this observation. However, the relatively large height of the globular structures combined with its insulating nature causes frequent interaction with the STM tip. As a consequence, the resolution and imaging quality of globular protein structures is limited, which is apparent in the missing submolecular detail or inverted contrast as seen in the inset of Fig. 6.4a. Present high resolution AFMs, however, will be able to image the topography of those objects without this problem, providing valuable data about the shape of a protein surface.[200] Moreover, local force fields mapped with AFM can provide chemical information. Especially in combination with functionalized tips, this could allow to answer the question what of the original functionality is present in vacuum.[201, 202]

To this point, it can be concluded that folded proteins can be introduced into vacuum and retain their shape upon deposition. The structure formation of un-

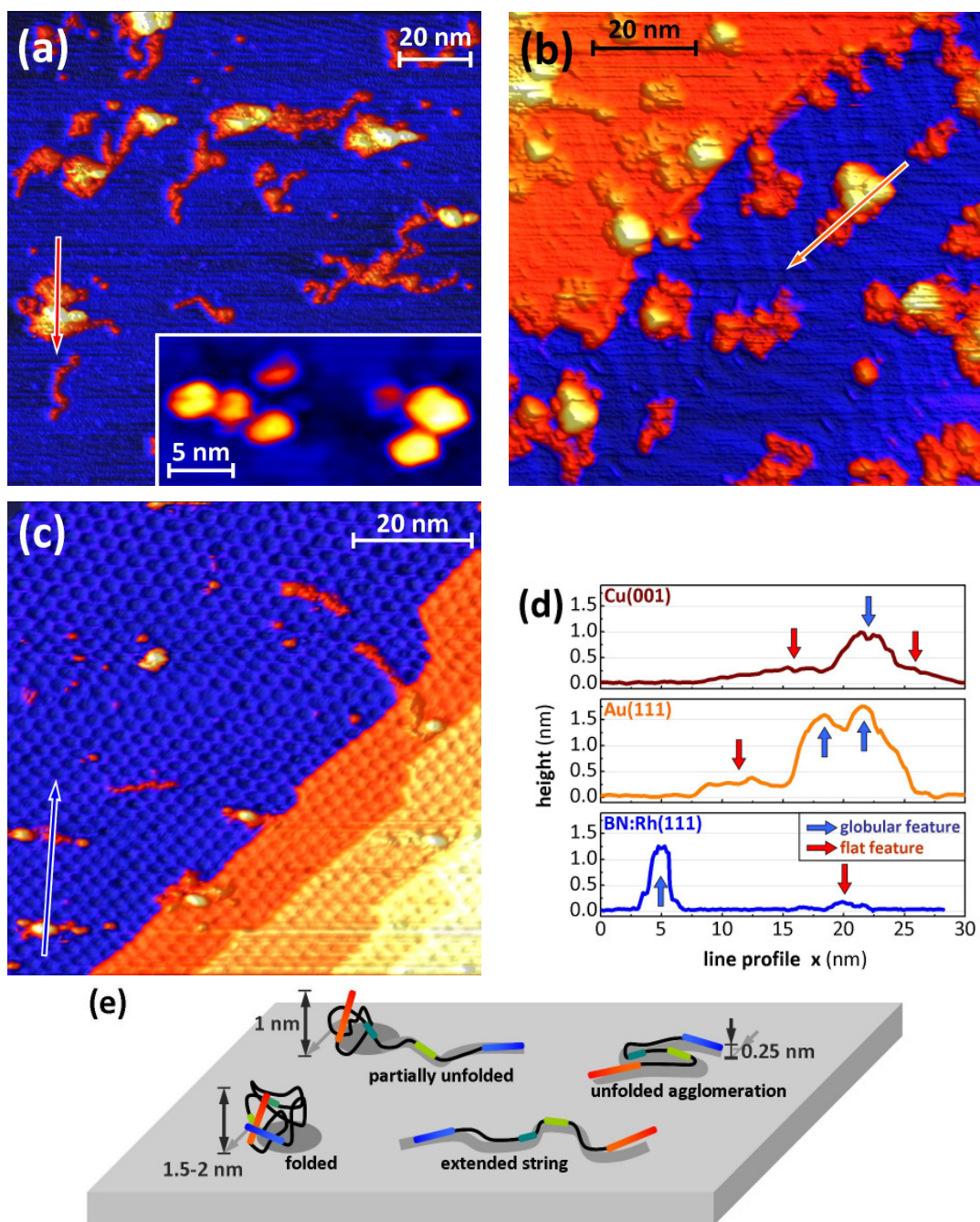


Figure 6.4: **STM topography of folded proteins after the deposition of low charge state CytC ion beams.** (a) on Cu(100). (b) on Au(111). (c) BN/Rh(111) boron nitride nanomesh. (d), Line profiles showing completely and partially folded proteins as high, globular features and unfolded proteins as low features. (e) Sketch of possible protein configurations: several nanometer high features result from partially or completely folded proteins, strings or patches of 0.25 nm height correspond to unfolded protein strands.



folded proteins is interesting for vacuum based nanotechnology. In particular the self-assembly of a protein via folding from an unfolded AA chain seems highly unlikely to occur under UHV conditions at a metal surface. We studied the behavior of unfolded CytC using the mass selected ion beams of high charge state in order to deposit purely unfolded proteins (see Figure 6.3b, red spectra).

The results of the depositions resemble the observations after the deposition of low charge state with the globular structures entirely absent. String shaped adsorbates are observed on the otherwise clean Cu(100) surface after the deposition of a 0.05 ML coverage of high charge state CytC ( $z > 12$ ) (Fig. 6.5a). A statistical analysis yields a length of  $25 \pm 3$  nm, which is significantly shorter than the expected length of 35.5 nm of the entirely unfolded protein. Considering, however, the high stability of the secondary structure in vacuum leads to intact  $\alpha$ -helices,[203] the expected length may be obtained as the following.

The unfolded CytC strands on Cu(100) may be described by wormlike chains with a contour length  $L$ . In the case of an extended polypeptide chain in  $\beta$ -configuration the contour length is given by

$$L_{\beta} = (n - 1) \times 0.345 \text{ nm} = 35.5 \text{ nm} , \quad (6.1)$$

where  $n = 104$  is the number of amino acid residues. However, one has to take into account that CytC contains 47 amino acid residues with  $\alpha$ -helical arrangement [177]. Therefore, the contour length of a chain molecule with both extended  $\beta$ -configurations and  $\alpha$ -helices is given by

$$L_{\alpha,\beta} = (n - 1 - 47) \times 0.345 \text{ nm} + \frac{47 \times 0.54}{3.6} \text{ nm} = 26.4 \text{ nm} , \quad (6.2)$$

where an  $\alpha$ -helix has 3.6 residues per turn and the corresponding pitch length is 0.54 nm. Since STM image analysis yields  $L = 25 \pm 3$  nm (Fig.6.5c), based on this calculation we conclude that the  $\alpha$ -helices have not been unfolded during the experiment.

On Cu(100) at room temperature no pair of CytC molecules with the exactly same adsorption configuration can be found. In principle, the flexibility of the polymer chain allows for an enormous amount of possible configurations in three dimensions and also when the confinement to the surface reduces the degrees of freedom. However, purely unfolded CytC on Cu(100) shows no sign of surface mobility such as step edge decoration, agglomeration or ordering. As a consequence, unfolded CytC protein ions are immobilized immediately upon contact with the strongly interacting Cu(100) surface. The observed geometry thus resembles the gas phase ion's configuration projected to the surface. Caused by the coulomb repulsion, highly charged protein ions have an extended chain conformation. Our data from the analysis of the distribution of intermolecular distances (see Fig. 6.5d) matches the behavior of a

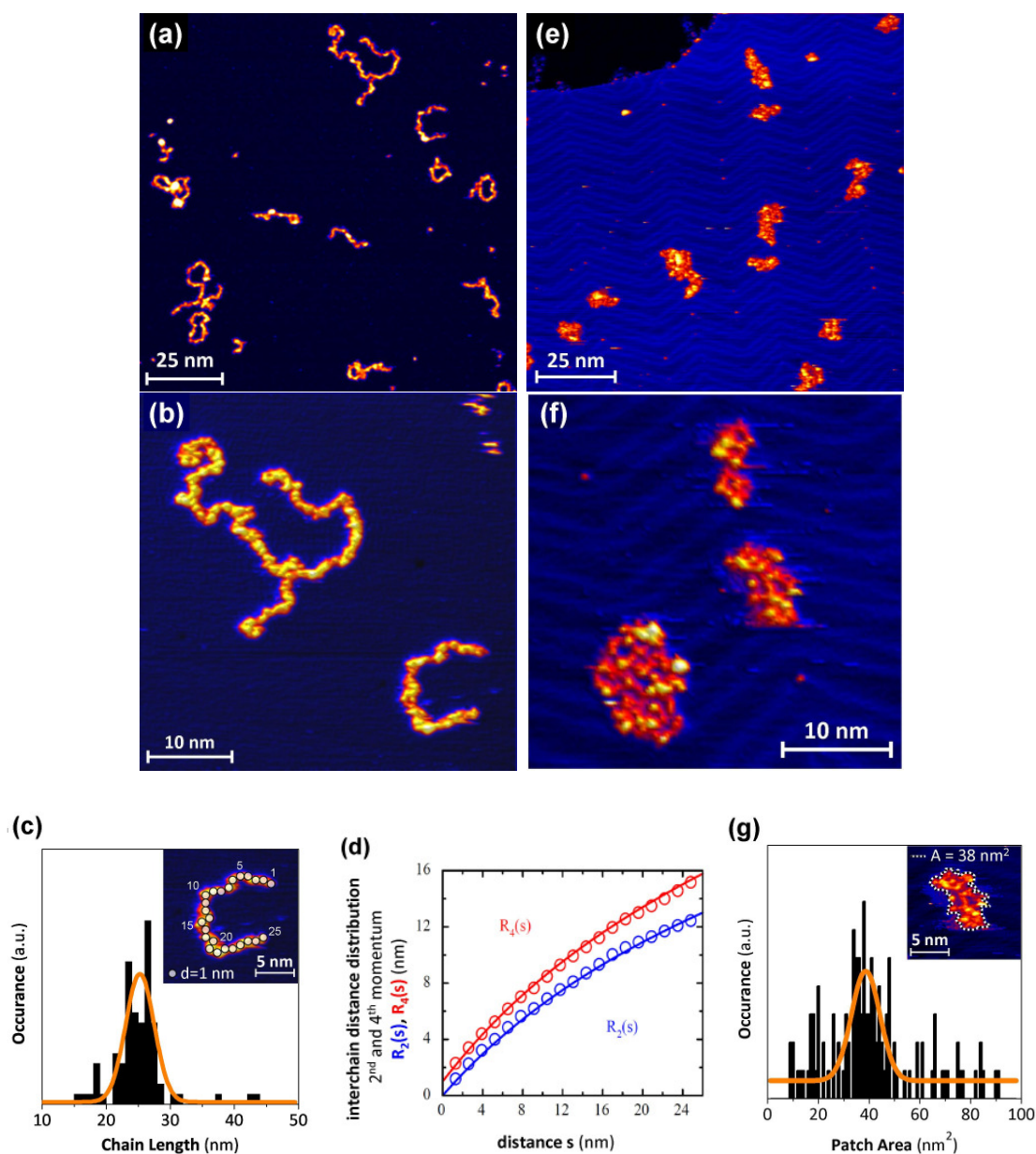


Figure 6.5: **STM topographies of unfolded cytochrome c** deposited from ion beams of high charge state. (a) CytC on Cu(100), large scale image. (b) high resolution image from (a) showing three peptide stands. (c) Histogram of the chain length on Cu(100) showing a length of  $25 \pm 3$  nm, which fits with an unfolded protein with intact  $\alpha$ -helices. (d) The second and fourth momentum of the interchain distance measured from STM images (hollow circles) fits the wormlike chain model for a noninteracting polymer (straight lines). (e) Unfolded CytC on Au(111). (f) Magnification of compact patches of cytochrome c. Two small patches of approx.  $40 \text{ nm}^2$  represent one protein each, the large patch  $80 \text{ nm}^2$  comprises two strands. (g) The histogram of the patch area.

three-dimensional worm-like chain with a persistence length of 6 nm projected onto a surface (see Appendix ii).[204]

In contrast, after the deposition of high charge state CytC ion beams on Au(111), compact patches that cover an area of approximately  $39 \pm 4 \text{ nm}^2$  are observed (Figs. 6.5e, f). The compact patches are found at the step edges and at the elbow sites of the reconstruction, indicating surface mobility of the unfolded proteins on gold. The compact structure is a result of attractive intramolecular interactions. In contrast to the gas phase, on a metal surface charged sites are either neutralized or effectively screened. While the protein is initially immobilized at one or only few points – for instance via opened disulfide bonds or a carboxylic acid group – the rest of the chain is mobile and able to find an energetically favorable position, which is in the vicinity of another part of the chain. The characteristic pseudo diameter of these patches in the plane of the Au(111) surface is determined by the aforementioned persistence length of the unfolded CytC proteins. This mechanism is sufficient to explain the occurrence of irregular patches and suggests that the intrachain interactions are unspecific, since no identical patches are found.

The primary structure of CytC is imaged as a set of protrusions. The height of the structures on Au(111) of 0.15-0.35 nm (Fig. 6.5f) is found to be higher than the height of 0.15 - 0.25 nm of the string-shaped adsorbates on Cu(100). In the close-packed patches, not all side groups of the AA are laying flat on the surface. Protrusions above 0.3 nm height are thus attributed to the side groups of AAs pointing out of the surface plane. Three individual peptide chains on Cu(100) are shown in Fig. 6.5b, each composed of many protrusions of varying size or equivalent pitch of 0.5-0.8 nm. This length corresponds to the size of two or three AAs. Accordingly, the number of 30-60 lobes is found to be a fraction of the number of AAs. On Au(111) the distribution and size of submolecular protrusions is consistent with CytC on copper. However, since the CytC chain interacts with itself, the number of observed protrusions is reduced to 20-30 per patch. The variation of the intensity in the lobes is related to the different density of states for each AA group, which suggests the investigation by inelastic tunneling spectroscopy with the ultimate goal to identify the AA sequence.[205]

## Submolecular Structure of Protein/Peptide Adsorbates

The amino acid sequence determines the three-dimensional structure of a protein and thus its functionality. Therefore, sequencing proteins, as the identification of a single amino acid and its position in the chain, is central to the study of proteins. In the presented STM images of unfolded CytC (Figs. 6.5) lobes are observed, which correspond to one to three amino acids, which demonstrates that STM provides enough resolution to in principle identify amino acids.

In the following, STM is employed to characterize the structure of unfolded CytC

on Au(111) and Cu(100) in detail. We investigate the variation in contrast of the CytC submolecular features upon variation of the bias, because differences in local density of states (LDOS), which are characteristic to the proteins' structural elements could allow for an identification. In a comparable system, guanine bases in a single stranded DNA can be distinguished from other nucleotides due to the appearance of distinct bright spots along the chain.[205] However, our experiment on a much more complex system, composed of 20 different units, requires additional information which is gained by the variation of the gap voltage. This could allow to identify the structural elements of proteins by the local change of contrast within the observed structure once a complete set of tunneling spectra for amino acids is known. In the following this possibility is studied.

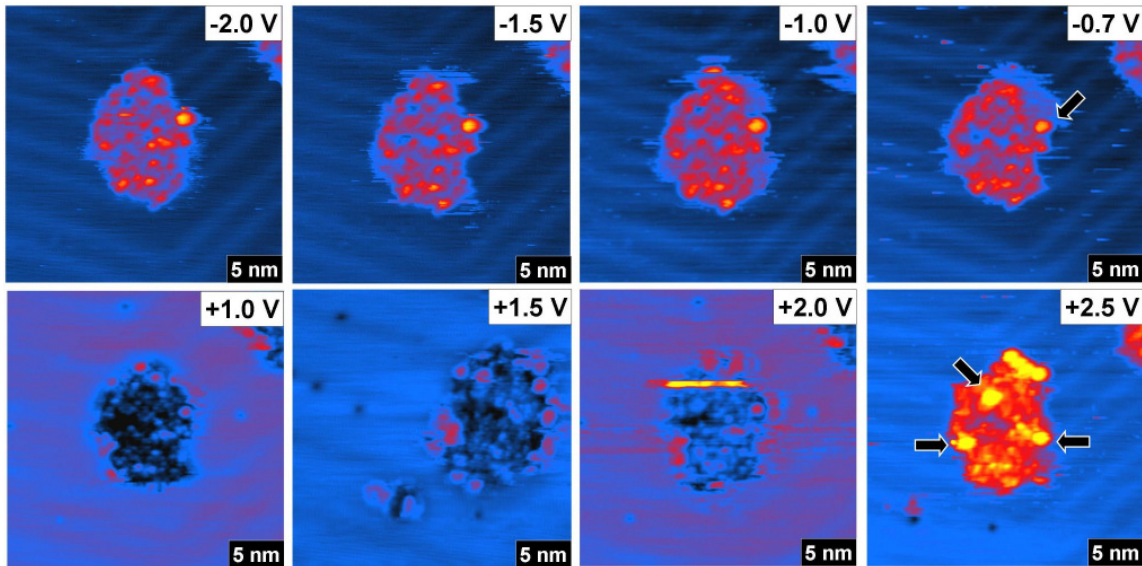


Figure 6.6: **STM images of high-charge CytC on Au(111) at various tunneling voltages** Negative voltages provide similar compact structure with a bright spot on the right. Contrast changes are observed when the bias voltages are positive.

A set of topographic images of the same selected area, displayed in Figs. 6.6 and 6.7 for unfolded CytC on Au(111) and Cu(100) respectively, is obtained by varying the bias voltage. The observed structures agree with the observations made before. With each set a contrast inversion of the protein chain is found at a certain bias.

In Fig. 6.6, the structures obtained from negative bias have a similar two-dimensional compact configuration. A bright spot can be observed on the right side of the compact structure as marked by the arrow in the panel for -0.7 V. As the bias changes towards positive voltage, the shape of the structure remains unchanged,

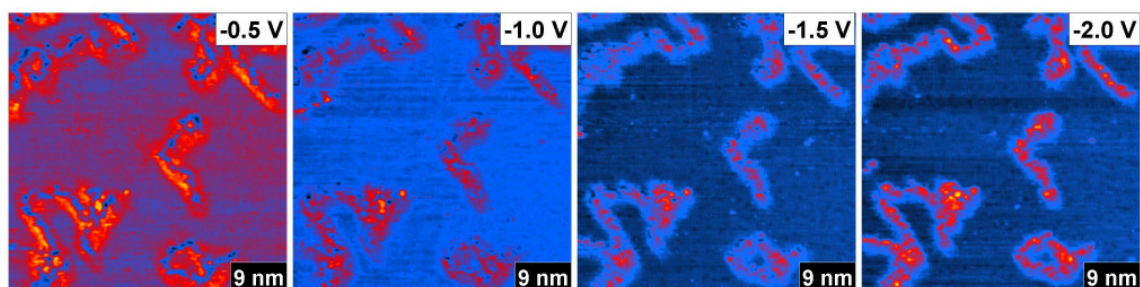


Figure 6.7: **STM images of high-charge CytC on Cu(100) at various tunneling voltages** Similar chain conformations with contrast changes are observed at bias voltages between -0.5 and -2.0 V.

while the contrast with respect to the other lobes changes. In general, at positive bias, the lobe pattern shows an overall different contrast. For instance at +2.5 V other distinctly bright spots appear at completely different positions than for negative bias.

For Cu(100) only the negative range of bias voltages is imaged, since a stable image could not be obtained at positive bias. However, a similar result is found. STM images of the same area on the surface show that the chain conformations look similar for all voltages. In contrast to Au(111), by changing towards positive bias the whole chain inverts in contrast already at low negative bias. Again the relative intensity of the lobe pattern changes.

This change of contrast on different lobes as the bias changes indicates the distinct difference in the density of states of the submolecular units, which correspond to one or several amino acids. This suggests a possibility to identify the amino acid residues in the proteins. Tunneling spectroscopy can be employed to obtain the above information with better resolution. An unambiguous identification, however, will only be possible if the conformation on the surface is clear, in particular since several amino acids contribute to one lobe observed. This will require tip manipulation to obtain a reproducible configuration. Moreover, an extremely huge reference data for all 20 amino acids in different sequences and for all possible configurations will have to be obtained. Although this approach requires a tremendous effort, it may be practical for smaller systems.

## 6.4 Parameters Influencing the Protein Conformation on the Surface

During surface preparation and characterization, several parameters can influence the adsorbed protein conformations. The pH value of the solution and the presence of

organic solvents or acid can induce unfolding in the electrospray solution. In vacuum, the structure formation of adsorbates can be influenced by thermal treatment. In addition, the collisions of the molecules with the surface in IBD are energetic enough to influence the state of the protein, for instance induce unfolding. In the following, the effect of elevated surface temperature and deposition energy on the structure of adsorbed CytC is studied.

### 6.4.1 Influence of Thermal Treatment

Elevated temperature is well-known to cause most proteins to denature in solution starting at temperatures above 40 °C. Therefore, the CytC coated surface was temperature treated to test this influence on the adsorbed proteins in vacuum. Moreover, an increase in temperature can result in an increased mobility of the adsorbates on the surface, which may result in self-organized structures.

To perform this test, an ion beam containing folded CytC was deposited on the Cu(100) surface by IBD (corresponding to the blue mass spectrum in Fig. 6.3b). As shown before, in situ STM characterization revealed the globular islands, which are attributed to the folded part, and unfolded chain aggregates beneath those structures (Fig. 6.8a).

The Cu(100) substrate with folded and partially unfolded proteins was annealed stepwise to 393 K and 473 K. STM characterization (Fig. 6.8) shows the decrease in size of the globular islands at the surface, while the amount of the unfolded chains covering the surface is increasing. The initial sizes of the globular islands in Fig. 6.8a are  $4 \pm 1$  nm in diameter and the height is  $0.7 \pm 0.2$  nm. These values reduce to  $2.5 \pm 0.5$  nm in diameter and  $0.4 \pm 0.2$  nm in height in Fig. 6.8b. The further increase in temperature to 473 K results in substantial amount of small features (below 2 nm diameter and below one Angstrom height) on an overall rough surface on which neither large globular features nor long chains can be observed (Fig. 6.8c).

This behavior complies with a strong molecule surface interaction characteristic for Cu(100) mostly inhibiting adsorbate diffusion. Instead, small fragments are created by unfolding the intact protein and subsequent disintegration of the unfolded chains. The results indicate that proteins can be unfolded or denatured on surfaces in UHV by raising the surface temperature.

According to the above discussion, the unfolded CytC can further disintegrate at the temperature above 400 K. Especially no enhanced diffusion was observed. In order to confirm this observation, the effect of temperature on the readily unfolded CytC on Cu(100) surface was studied. This time, the temperature was kept at 400 K to check whether the mobility of the unfolded chains will induce structural organization. In this experiment, the ion beam containing only high charge states was used for IBD (Fig. 6.3b, red spectrum). After the deposition, the Cu(100) surface was annealed at 400 K for 1 min, followed by the second annealing for 10 min at the same temperature.

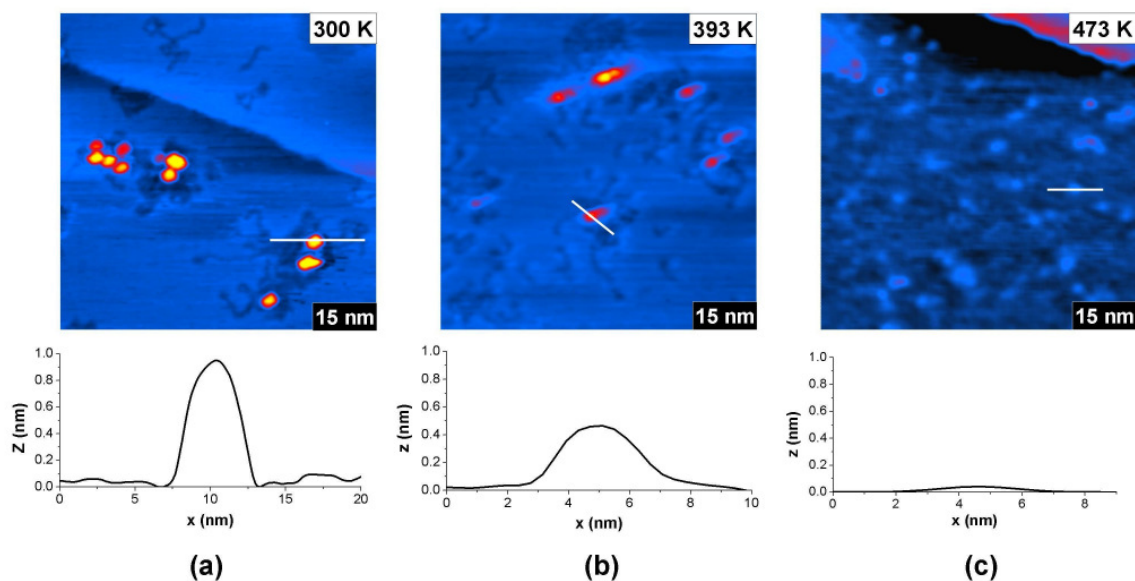


Figure 6.8: STM images of low charge-state CytC on Cu(100) deposited by IBD in UHV: (a) as deposited, (b) annealed at 393 K and (c) at 473 K. Size reduction of globular islands and extended amount of unfolded chains are observed after annealing at 393 K. Further annealing to 473 K results in small elevated spots on an overall rough surface.

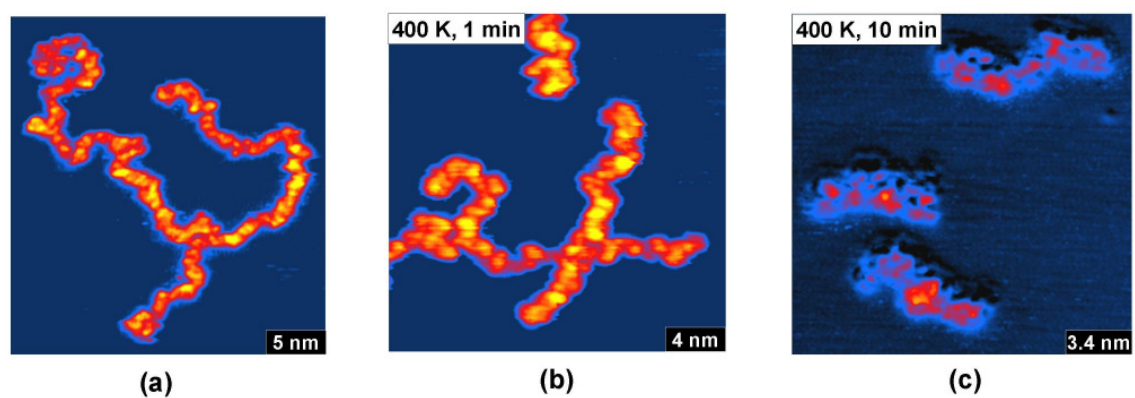


Figure 6.9: STM images of high charge-state CytC on Cu(100) deposited by IBD in UHV as grown (a), flash annealed (b) and 10-min annealed (c) at 400 K. The length of the unfolded chains decreases after each annealing step.

Fig. 6.9 shows the structures of the chains as deposited, and after each annealing step. The change in size of the chains upon annealing can be observed. The width of the chains does not change significantly. The length of the strands decreases upon further annealing from 25 nm to 16 nm and 7 nm at average as a consequence of fragmentation.

The changes in configuration of the unfolded CytC upon annealing can be compared to the ones observed for folded CytC (Fig. 6.8) In both cases, the long chains could not be found after the second annealing at the temperature of 400 K or above, however, the limited mobility is still observed. In contrast to CytC on the gold surface, which is mobile at room temperature and thus forms compact patches, the strong interaction of CytC with the copper substrate inhibits such ordering.

### 6.4.2 Influence of the Deposition Energy

As discussed in chapter 3, the incidence energy upon deposition has a direct influence on the soft landing efficiency.[84] It is assumed that large and fragile biological molecules require a deposition with low incidence energy in order to retain the integrity on the surface, which is generally referred to as soft landing. For proteins it has been shown that this is possible on specially prepared soft surfaces, such as functionalized self-assembled monolayer (SAM) surfaces [95] or glycerol-based liquid surfaces [96].

To study the effect of surface collision on the structure of CytC on a metal surface in the low incidence energy-range, two otherwise identical IBD experiments were performed varying only the incidence energy. The goal is to test soft landing of proteins and whether the energy leads to deformation of the structure, unfolding or higher mobility on the surface.

Fig. 6.10 shows STM images of Cu(100) surface deposited by the beam containing low-charge states of CytC at the incidence energy of 5 eV (a) and 27 eV (b) per charge. These correspond to kinetic energies per molecule for the charge states +7-+10 of 35-50 eV and 189-270 eV, respectively. At this energy fragmentation or unfolding is possible. However, a similar topography was obtained for both cases. The structures observed on the surface consist of globular islands with unordered chain aggregates in the vicinity, which is interpreted as either partly-unfolded CytC or folded CytC immobilized by binding to unfolded adsorbed CytC strands. This result shows that an incidence energy in the range of 5-27 eV per charge does not lead to the disintegration or unfolding of the molecules.

For comparison, the impact energy of 1 eV per atom was found to ensure soft landing of nanoparticles on a metal surface.[136] Since proteins are much larger particles – 1669 atoms for CytC – the disintegration should be induced by a very high impact energy according to this rule. Soft landing experiments with other molecules, including peptides, confirmed that the rule of thumb of 1eV per atom is correct also



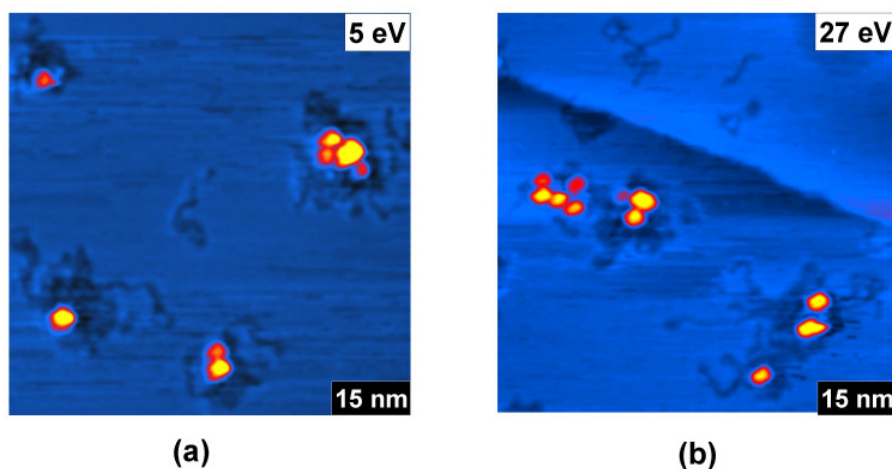


Figure 6.10: **STM images of low charge-state CytC on Cu(100) deposited at the incidence energy of 5 and 27 eV per charge** Depositions at both energies reveal similar structures of globular islands underlying by unordered chain aggregates.

for molecules.[99, 37, 93] Still, deformation and unfolding can occur at lower energy without breaking covalent bonds. The identical morphology and general structural features found for low and high deposition energy show that this is, however, not the case. Moreover, an enhancement of the mobility upon increasing the impact energy is not observed either.

## Summary and Conclusions

The study of proteins by STM in a UHV environment proved the feasibility of using IBD in combination with in situ analysis for large, functional, fragile molecules. Surface coatings can be produced in a controlled manner resulting in homogeneous coverage of proteins on an otherwise clean surfaces. Single proteins of folded and unfolded conformation can be visualized. IBD allows to steer, which configuration of the protein is deposited. The deposition of low-charge CytC results in large three-dimensional globular islands, which are folded proteins with the unfolded string aggregates nearby. The deposition of high-charge states results in flat lying chain-like conformations of unfolded proteins or two-dimensional folding. By changing the gap voltage, the relative intensity of the submolecular features was changed, which might allow to identify structural elements of the adsorbed proteins. The observed mixture between the folded and unfolded structures for the low-charge CytC on different surfaces is constant and thus is only the consequence of partially unfolding occurring

before the deposition in solution or in the electrospray. Hence, the surface does not influence the folded state, that is it is stable in vacuum, however might not exactly represent the native state of the protein.

Besides the unambiguous identification of the protein sequence, two-dimensional self-assembly of oligopeptide- or even protein chains is another vision conveyed by this study. Due to the limited thermal stability, up to now peptide self-assembly at surfaces in vacuum was limited to mono- and dipeptides. Nevertheless, complex behavior and effects such as chiral recognition could be demonstrated.[206, 207, 54]

The self-assembly of the peptide strand into compact, yet irregular patches observed on the Au(111) surface, illustrates the possibility of two dimensional folding. Not surprisingly, the CytC sequence evolved to be folded in aqueous solution, did not yield regular assemblies. However, other sequences might do so.[203] Compact patches of CytC formed by unspecific interactions are weakly bound and thus only form at low temperatures. However, this suggests that it might be possible to form deterministic structures at room temperature by exploiting a hierarchical self-assembly approach that leads to stronger specific bonds in the folded structure. Finding appropriate sequences will require substantial theoretical and experimental effort, yet it promises to add to the understanding of self-assembly by folding as well as opening the possibility for protein-like two-dimensional functional structures at surfaces.

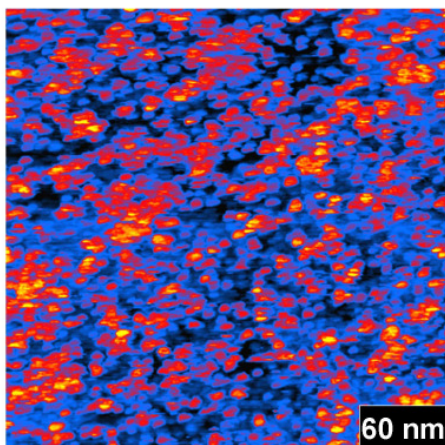


Figure 6.11: **STM images of high coverage folded CytC on Au(111)**

Apart from the well-known influences causing denaturing of proteins in solution and in the gas phase, unfolding of CytC on a surface in UHV by raising the surface temperature was demonstrated. Surface interactions play an important role in the conformations of the adsorbed proteins. The unfolded chains can retain their gas-phase conformations on Cu(100) or fold into compact two-dimensional coils on

Au(111). The incidence energies of 5 and 27 eV per charge upon depositions reveal similar structure of adsorbed CytC on the surface. Therefore, collision energies in this range do not lead to protein unfolding.

This study shows that proteins are compatible with vacuum technology and thus paves the way towards the development of technological applications of proteins on surfaces. For this either folded or unfolded proteins can be used. The fabrication of 2D- and 3D-functional nanostructures on surfaces by folding of tailored peptides on the surface can be envisioned. Fig. 6.11 shows a high coverage of folded CytC on Au(111) surface, which was achieved by only a few hours of deposition. This shows that IBD is capable as a method allowing surface modification by a full monolayer of proteins in UHV. This opens up the opportunity to provide biofunctional thin films on surfaces in a clean environment.



Part III

Summary and Outlook



This thesis covers studies of a broad range of functional molecules on surfaces in UHV. Due to the thermal instability or lack of vapor pressure of many nanoscopic particles, the combination of electrospray ion beam deposition (ES-IBD) and in situ STM analysis enables submolecular resolved investigations under well controlled UHV conditions. This thesis intends to cover a range of new possibilities: experiments start from small molecules, continue over coordination compounds and epitaxy and finally show the application of our approach to biological macromolecules.

To initially characterize the experimental approach of ES-IBD, Rhodamine 6G, an organic dye is deposited on surfaces. The STM analysis shows a homogeneous layer of the molecules on otherwise clean surfaces for different coverage. Collision-induced dissociation (CID) of the molecular ions was studied. The declustering potential is adjusted to vary the collision energy with the background gas and thus the level of molecular fragmentation. In this manner, intact molecules or fragments can be chosen as the composition in the ion beam. Surface deposition by the ion beams containing either intact molecules or fragments is confirmed by secondary ion mass spectrometry (SIMS) and matrix-assisted laser desorption ionization (MALDI). The results show that the adsorbed chemicals on the surface correspond to the substances contained in the initial beams.

Based on these initial study of CID in the gas phase, the fragmentation of molecules by collisions at a surface could be investigated. Several parameters can be adjusted during the deposition to explore a variety of structure formations and interactions, which could occur. One important parameter is the kinetic energy upon deposition, which is varied by biasing the target sample. Above 60 eV collision energy, substantial amounts of fragments are detected on the surface by SIMS. This result not only ensures that intact deposition can be reliably performed below that value, but also allows further investigations on the effect of collision energy upon the structure formation on surfaces.

The collision energy is an important factor for reactive landing, which takes place in the hyperthermic energy range. Chemical reactions at the surface can be induced by the impact of molecules or molecular fragments. Covalently bound molecular networks of functional molecules is one possible application of this approach. The molecular fragments can be created from selective dissociation either in the gas phase or at the surface. These radical ions are highly reactive and thus lead to chemical interactions on the surface to form stable covalent-bonded networks.[208]

Hydrophobic interactions have a major influence on the ordering of amphiphilic molecules such as sodium dodecyl sulfate (SDS), the model system for the following study. Layered growth of SDS is found on surfaces from aqueous solution and in vacuum, however, different molecular arrangement of the crystalline structures are found. In the electrospray, the SDS molecules aggregate and form large, highly charged clusters. Vacuum deposition of these resulted in inverted bilayers on graphite and  $SiO_x$  surfaces, in contrast to normal membranes formed under the influence of

the hydrophobic interaction. In vacuum the dominating structural motive is a head-to-head arranged SDS dimer, which is the basis for all observed structures including flat-laying double rows on Cu(100) observed by in-situ STM.

The study of SDS deposition shows that ES-IBD represents a deposition method equivalent to molecular beam epitaxy (MBE). The high quality molecular multilayers fabricated show that ES-IBD could be applied to fabricate layers that can serve as the basis for devices. Moreover, the amphiphilic bilayers are also interesting as artificial membranes with unusual properties. The experiment could be extended towards embedding of functional substances similar to proteins in real membranes, or receptors, which are only softly bound in the membrane to allow rearrangement that would support properties like chemical binding and recognition processes.

Large functional molecules, for which vacuum deposition by thermal sublimation cannot be applied, were successfully deposited on surfaces by ES-IBD. Coordination compounds represent an increasing level of complexity. Host-guest complexes of a macrocyclic crown ether, dibenzo-24-crown-8 (DB24C8) and various cations are formed in electrospray solutions and transferred to a Cu(100) surface in UHV by ES-IBD. Chemical characterization of the surface by MALDI confirmed the integrity of the adsorbed complex. STM at low temperature provides the molecular substructure of the complexes on the surface. The difference in the structure between the complexes formed by DB24C8 and  $Cs^+$ ,  $Na^+$  and  $H^+$  is visible with submolecular resolution showing the cavity of DB24C8. In combination with density functional theory (DFT) calculations, binding energy and interactions of the three different host-guest complexes at the surface are explained. The results show that DB24C8-alkali ion complexes stick to the Cu(100) surface while the DB24C8- $H^+$  complex is very mobile even at low temperatures.

This study provides the basis for the investigation of more complex host-guest macrocyclic systems. Due to the independence of functional groups interior and exterior of macrocycles, chemical modification of the molecules can be performed to manipulate the intermolecular interaction without interfering their host-guest functionality and vice versa. The modification of the interior functional groups can be performed to achieve, for instance molecular recognition or chiral interaction between the host and the guest molecules, where the exterior functional groups can be modified to obtain two-dimensional arrangements on surfaces. According to this unique property of macrocycles, two dimensional networks of macrocycles can be fabricated with various functionalities.

The final part of the thesis involves the investigation of a complex biological molecule that is a protein, Cytochrome c (CytC). Two different configurations of CytC: folded and unfolded, are successfully deposited and studied on surfaces. Similar to the crown ether experiment, the preparation of the electrospray solution turns out to be a simple way to define the structure of the deposited species. Unfolded proteins are prepared by adding formic acid and organic solvents to the electrospray



solution. In order to create an ion beam containing either folded or unfolded protein ions, mass selection is performed in the gas phase to select either the low or the high charge-state range. Characterized by STM, the deposition of low charge states results in three dimensional islands, observed isolated and as clusters together with flat chain aggregates nearby. High charge-state deposition yields only chain-like structure on the surface. The three dimensional islands and the chains correspond to folded and unfolded CytC, respectively. The observed chains for low charge-state deposition, could result from partially unfolding in the electrospray solution. The unfolded protein is imaged with submolecular resolution and their structural features, which could be attributed to single or multiple amino acids, can be resolved.

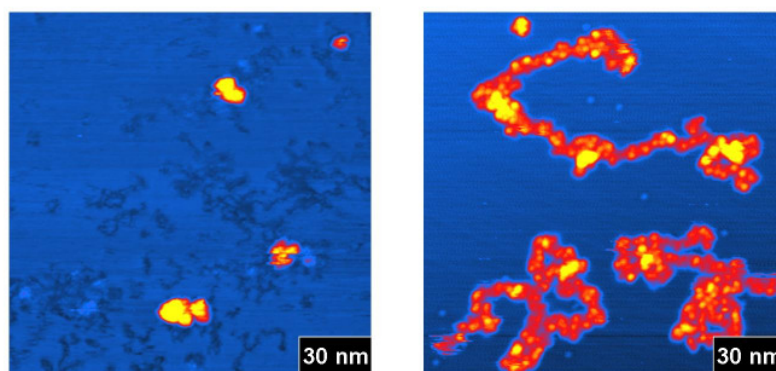


Figure 6.12: **Topographic images of folded and unfolded (left) and only unfolded (right) BSA on Cu(100) surface**

In addition to the unfolding of proteins in solution, other parameters, which may cause proteins to unfold are studied in vacuo. Increasing of the surface temperature after the deposition caused the adsorbed proteins to unfold followed by subsequent disintegration, while the impact energy of 27 eV per charge still yields intact deposition. Furthermore, the surface has a great influence on the adsorbed protein conformation. Folded CytC is very mobile until a binding site defined by the surface or aggregates of other molecules is found. The limitation in mobility of the unfolded chains on Cu(100) leads to a structure, which is the projection of their gas phase configuration. On Au(111), where pinning is only given at the elbow sites, the chains are folded into two-dimensional compact structures.

This study is currently continued by other proteins such as bovine serum albumin (BSA). The difference between folded and unfolded structures resemble the results obtained from CytC (Fig. 6.12). The result implies that a homogeneous layer of different types of proteins can be prepared by ES-IBD on a clean surface. The possibility to deposit gas-phase proteins on surfaces opens up manifold opportunities. The

creation of two and three dimensional protein crystals of selected conformation is one future goal of paramount importance. A further investigation into the functionality of the adsorbed proteins could also provide the possibility to mimic the biological process occurring in nature and study them with the unprecedented resolution of the STM. Moreover, self-organization of unfolded proteins or peptides can also be explored on surfaces by the deposition of high charge-state proteins or adjusting the influencing parameters such as surface temperature. This study could provide a step closer to the two-dimensional folding of proteins into a well-defined structure, which supports structural characterization and enables further growth of three-dimensional protein crystals.

In summary, the results obtained in this thesis from the investigation of many classes of functional molecules ranging from small organic to large biological substances show many different ways towards the design and controlled fabrication of new materials from nonvolatile compounds. The combination of ES-IBD and in situ STM analysis allows a broad range of molecules to be studied on surfaces at submolecular level that were not available before. Molecular interactions and chemical processes in complex molecules happening at the nanoscale can now be investigated with unprecedented precision.

Future research will aim to explore the functional aspects of nanomaterials created from nonvolatile molecular substances. As molecules become bigger, their functions get more complex. As a result the interpretation of measurements becomes increasingly difficult. The fully controlled approach of ES-IBD thus is superior to other sample preparation techniques. For instance in contrast to evaporation it is always known what species is deposited. This knowledge is particularly important when scanning probe techniques are used, since they unfold their full potential, when it is known which molecule is observed. Therefore STM and AFM in combination with ES-IBD enable the study of chemical and physical effects of highest complexity at the submolecular scale. Interesting phenomena include molecular magnetism and other spin correlation effects in molecules, catalysis or optical activity.

As an example of this approach in our laboratory a prototype molecular magnet, Manganese-12-Acetate-16 (*Mn12*) has been studied as single molecule adsorbed on a thin-insulating surface, which is then transferred to a low-temperature (1.5 K) STM without leaving the UHV. The results suggest the preservation of molecular magnetism of *Mn12* on the surface. This study is an important step for further understanding of the properties of single molecular magnets on surface, which can be applied as a basis to create nanomagnetic devices.

In a similar way as the study of *Mn12*, the properties of other large functional molecules can be explored on surfaces in UHV. This provides an opportunity to discover molecules with exciting properties for vacuum-based applications.

In addition to being employed as individual, large highly functional molecules can also serve as building blocks to form well-defined nanostructures at surfaces with

desired functionalities. An attempt can be made to control the intermolecular interactions, which define the structure formation. Molecular self-assembly is a typical method to create molecular networks through noncovalent intermolecular forces. Due to the weak interactions, these networks are less stable compared to covalently bond networks. However, in order to build a covalent network, a more complicated procedure is required. Selective dissociation of molecules by temperature treatment into reactive radicals showed a possibility to produce covalent networks.[208] Reactive landing of molecular ions or fragments onto reactive surfaces is another approach, by which new covalent bonds can be created, such as peptides and self-assembled monolayers.[93]

Here, ES-IBD can be employed to create radical ions from large molecules either in the beam or on the surface to enable the formation of functional covalent networks. Among the large molecules, proteins and peptides are promising candidates, which support rational design and construction of preferred nanostructures. In addition to in situ STM characterization, the bulk properties of such systems are highly interesting for potential applications. In this context ES-IBD can be envisioned as a fabrication technique for conductive polymer layers, catalytically active layers or sensor surfaces.

In general, ES-IBD can be used as a tool equivalent to MBE to grow epitaxial layers of molecules for devices. The advantage of ES-IBD is that the molecular beams are more controlled and a broader range of molecules can be applied, while MBE is limited to atoms or volatile molecules. In this way, functional nonvolatile molecules can be utilized in vacuum-based technology, providing a great opportunity to develop more complex nanoscale devices.

The study of large nonvolatile substances can be extended from molecules to nanoparticles. Since nanoparticles have many different shapes and properties, thus can be assembled to form nanocrystals with new combined functionalities for applications in electronic, magnetic or optical devices. Carbon-based materials, such as carbon nanotubes and graphenes attracted great interests in molecular electronics.[209] These materials can be used for a controlled deposition in UHV combined with other nanoparticles or molecules to create a new device with novel functions.

This research shows the promising capability of ES-IBD as an unprecedented method for device and sample fabrication. New types of electronic and memory storage devices, high sensitivity sensors or biomimicking systems from nonvolatile molecules and nanoparticles are now possible.



# Appendix

## i) Density Functional Theory Calculations Description

DFT modelization of the adsorbed DB24C8 complexes on the Cu(100) surface [37] was carried out by means of the QuantumESPRESSO package [210], which makes use of plane-wave expansion of the system wave function in periodically repeated supercells. Here a  $21.6 \times 18.0 \times 18.0 \text{ \AA}^3$  tetragonal cell is used; the Cu(100) surface was modeled by just two Cu layers due to the large lateral extension of the cell, necessary to avoid interactions between adsorbates in adjacent periodic images. The positions of the copper atoms of the lowest layer were kept frozen at the equilibrium bulk geometry during the optimization processes. Calculations were performed with the Perdew-Burke-Ernzerhof exchange-correlation functional [211], using Vanderbilt-type ultrasoft potentials [212] with a kinetic energy cutoff of 40 Ry; this led to a nearest-neighbor Cu-Cu distance of  $2.55 \text{ \AA}$ , which is in good agreement with the experimental value. For cesium a norm-conserving Troullier-Martins pseudopotential [213] is used, due to the unavailability of ultrasoft potentials; convergence tests proved that the 40 Ry cutoff represents a satisfactory compromise between energetic/geometric accuracy and sensible computational time usage. The k-points sampling was limited to the Gamma point. The adsorption energies of the DB24C8-alkali complexes were determined by the deposition of the complex with a Cl<sup>-</sup> counterion to avoid computation of an overall charged supercell. STM images were simulated by means of the specific tool in the QuantumESPRESSO package, based on the Tersoff-Hamann approach.[170, 171] All images were produced using the XCrySDen program.[214]

*Density functional theory calculations were performed by Dr. Giacomo Levita, INFN-Democritos Modeling Center for Research in Atomistic Simulation, Trieste, Italy as collaboration in this project.*

## ii) Contour Length and Persistence Length of Highly Charged, Unfolded CytC Strands on Cu(100)

As suggested by the imaging data (see Fig. 6.5 of chapter 6), the highly charged, unfolded CytC strands on Cu(100) may be described by wormlike chains which are characterized by a contour length  $L$  and a persistence length  $l_p$ .

During deposition, the conformation of an unfolded CytC strand is modified by the transition from three dimensions in the ion beam gas phase to two dimensions on the surface of the substrate. The protein adsorbs without having equilibrated on the strongly interacting Cu(100) surface. Therefore, the resulting unfolded protein conformation resembles a projection of the actual conformation in three dimensions onto the surface, where the contour length is conserved. In order to determine the molecular stiffness, the unfolded CytC strands are represented as continuous space curves  $\mathbf{r}(s)$ , where  $s \in [0, L]$  is the contour coordinate along the wormlike chain. Using the contour length  $L = 26$  nm and the persistence length  $l_p = 6.4$  nm the calculated radius of gyration projected onto the surface of the substrate is given by (see Refs. [204, 215] and references therein)

$$\begin{aligned} r_g &= \frac{1}{L} \sqrt{\frac{1}{3} \int_0^L \int_0^L \langle (\mathbf{r}(s_1) - \mathbf{r}(s_2))^2 \rangle} \\ &= \sqrt{\frac{2}{3} \left( \frac{l_p L}{3} - l_p^2 + \frac{2l_p^3}{L} - \frac{2l_p^4}{L^2} (1 - e^{-L/l_p}) \right)} = 4.3 \text{ nm}, \end{aligned} \quad (6.3)$$

where  $\langle \dots \rangle$  denotes a statistical average. The corresponding STM image analysis of highly charged, unfolded CytC strands on Cu(100) unfolded CytC strands yields  $r_g = 4.5$  nm. Besides the usual molecular stiffness of a neutral chain molecules, electrostatic interactions between charged residues further stiffens the protein strand leading to the above mentioned persistence length.

Moreover, equilibrium properties of wormlike chains are characterized by the mean end-to-monomer distance projected onto the surface of the substrate

$$r_2(s) = \sqrt{\langle (\mathbf{r}(0) - \mathbf{r}(s))^2 \rangle} = \sqrt{\frac{2}{3} (2l_p s - 2l_p^2 (1 - e^{-L/l_p}))}, \quad (6.4)$$

and the corresponding fourth moment

$$r_4(s) = \langle (\mathbf{r}(0) - \mathbf{r}(s))^4 \rangle^{1/4} = \left( \frac{5}{3} \right)^{1/4} r_2(s). \quad (6.5)$$

Equation (6.5) follows from a Gaussian distribution of intramolecular distances  $\mathbf{r}(0) - \mathbf{r}(s)$ . Fig. 6.5d shows the calculated (lines) and measured (symbols) mean end-to-monomer distance  $r_2(s)$  (lower data set) and the fourth moment  $r_4(s)$  (upper data

set) as a function of the contour coordinate  $s$ . The upper data set has been shifted by adding the value 1 for better visibility. The comparison of the experimental and theoretical data validates the use of a wormlike chain model to analyze average conformational properties of highly charged, unfolded CytC strands on Cu(100). However, characteristic features of the well-defined sequence of  $\beta$ - and  $\alpha$ -configurations along the chain may lead to specific conformations of individual proteins. For example the short helix in the middle of the chain together with the  $\beta$ -configurations close to it may act as a hinge, while other charged segments are rather stiff.

*This analysis was performed by Dr. Ludgar Harnau, Max Planck Institute for Intelligent Systems, Stuttgart, Germany as collaboration in this project.*





# Bibliography

- [1] M. Goldberg, R. Langer, and X. Q. Jia. Nanostructured materials for applications in drug delivery and tissue engineering. *J. Biomater. Sci., Polym. Ed.*, 18(3):241–268, 2007.
- [2] A. Chung, J. Deen, J. S. Lee, and M. Meyyappan. Nanoscale memory devices. *Nanotechnology*, 21(41):412001, 2010.
- [3] S. S. Mao and X. B. Chen. Selected nanotechnologies for renewable energy applications. *Int. J. Energ. Res.*, 31(6-7):619–636, 2007.
- [4] R. F. Davis, G. Kelner, M. Shur, J. W. Palmour, and J. A. Edmond. Thin-film deposition and microelectronic and optoelectronic device fabrication and characterization in monocrystalline alpha and beta silicon-carbide. *P. IEEE*, 79(5):677–701, 1991.
- [5] J. Asmussen. Electron-cyclotron resonance microwave discharges for etching and thin-film deposition. *J. Vac. Sci. Technol., A*, 7(3):883–893, 1989.
- [6] G. Tallents, E. Wagenaars, and G. Pert. OPTICAL LITHOGRAPHY lithography at EUV wavelengths. *Nature Photon.*, 4(12):809–811, 2010.
- [7] C. Vieu, F. Carcenac, A. Pepin, Y. Chen, M. Mejias, A. Lebib, L. Manin-Ferlazzo, L. Couraud, and H. Launois. Electron beam lithography: resolution limits and applications. *Appl. Surf. Sci.*, 164:111–117, 2000.
- [8] G. M. Whitesides, J. P. Mathias, and C. T. Seto. Molecular self-assembly and nanochemistry - a chemical strategy for the synthesis of nanostructures. *Science*, 254(5036):1312–1319, 1991.
- [9] J. Steed. SELF-ASSEMBLY molecular recognition scaled up. *Nature Chem.*, 3(1):9–10, 2011.
- [10] M. Lorenz, A. Rahm, B. Q. Cao, J. Zuniga-Perez, E. M. Kaidashev, N. Zhakarov, G. Wagner, T. Nobis, C. Czekalla, G. Zimmermann, and

- M. Grundmann. Self-organized growth of ZnO-based nano- and microstructures. *Phys. Status Solidi B*, 247(6):1265–1281, 2010.
- [11] J. M. Lehn. Perspectives in supramolecular chemistry - from molecular recognition towards molecular information-processing and self-organization. *Angew. Chem., Int. Ed.*, 29(11):1304–1319, 1990.
- [12] G. Binnig, C. F. Quate, and C. Gerber. Atomic force microscope. *Phys. Rev. Lett.*, 56(9):930–933, 1986.
- [13] G. Binnig and H. Rohrer. Scanning tunneling microscopy. *Helv. Phys. Acta.*, 55(6):726–735, 1982.
- [14] M. Ohara, Y. Kim, and M. Kawai. Controlling the reaction and motion of a single molecule by vibrational excitation. *Chem. Phys. Lett.*, 426(4-6):357–360, 2006.
- [15] K. Petukhov, M. S. Alam, H. Rupp, S. Stromsdorfer, P. Muller, A. Scheurer, R. W. Saalfrank, J. Kortus, A. Postnikov, M. Ruben, L. K. Thompson, and J. M. Lehn. STM spectroscopy of magnetic molecules. *Coord. Chem. Rev.*, 253(19-20):2387–2398, 2009.
- [16] M. Forster, M. S. Dyer, M. Persson, and R. Raval. Probing conformers and adsorption footprints at the single-molecule level in a highly organized amino acid assembly of (S)-Proline on Cu(110). *J. Am. Chem. Soc.*, 131(29):10173–10181, 2009.
- [17] N. Oyabu, Y. Sugimoto, M. Abe, O. Custance, and S. Morita. Lateral manipulation of single atoms at semiconductor surfaces using atomic force microscopy. *Nanotechnology*, 16(3):S112–S117, 2005.
- [18] R. M. Penner. Nanometer-scale synthesis and atomic-scale modification with the scanning tunneling microscope. *Scanning Microscopy*, 7(3):805–813, 1993.
- [19] A. A. Tseng and Z. Li. Manipulations of atoms and molecules by scanning probe microscopy. *J. Nanosci. Nanotechnol.*, 7(8):2582–2595, 2007.
- [20] J. R. Arthur. Molecular beam epitaxy. *Surf. Sci.*, 500(1-3):189–217, 2002.
- [21] T. Sugaya, K. Komori, S. Yamauchi, and T. Amano. 1.3  $\mu\text{m}$  InAs quantum dots grown with an As-2 source using molecular-beam epitaxy. *J. Vac. Sci. Technol., B*, 23(3):1243–1246, 2005.
- [22] F. Besenbacher. Scanning tunnelling microscopy studies of metal surfaces. *Rep. Prog. Phys.*, 59(12):1737–1802, 1996.

- [23] M. P. de Jong, V. A. Dediu, C. Taliani, and W. R. Salaneck. Electronic structure of La<sub>0.7</sub>Sr<sub>0.3</sub>MnO<sub>3</sub> thin films for hybrid organic/inorganic spintronics applications. *J. Appl. Phys.*, 94(11):7292–7296, 2003.
- [24] P. Debbage. Targeted drugs and nanomedicine: Present and future. *Curr. Pharm. Des.*, 15(2):153–172, 2009.
- [25] C. Y. Zhang and L. W. Johnson. Single quantum-dot-based Aptameric nanosensor for cocaine. *Anal. Chem.*, 81(8):3051–3055, 2009.
- [26] D. Vuillaume. Molecular nanoelectronics. *Proc. IEEE*, 98(12):2111–2123, 2010.
- [27] M. C. Hersam, N. P. Guisinger, and J. W. Lyding. Silicon-based molecular nanotechnology. *Nanotechnology*, 11(2):70–76, 2000.
- [28] J. M. Tour. Transition to organic materials science. passive, active, and hybrid nanotechnologies. *J. Org. Chem.*, 72(20):7477–7496, 2007.
- [29] M. Sarikaya, C. Tamerler, A. K. Y. Jen, K. Schulten, and F. Baneyx. Molecular biomimetics: nanotechnology through biology. *Nat. Mater.*, 2(9):577–585, 2003.
- [30] D. R. Flower. The lipocalin protein family: Structure and function. *Biochem. J.*, 318:1–14, 1996.
- [31] J. J. Wendoloski, J. B. Matthew, P. C. Weber, and F. R. Salemme. Molecular-dynamics of a cytochrome-c cytochrome-b<sub>5</sub> electron-transfer complex. *Science*, 238(4828):794–797, 1987.
- [32] Z. D. Wang and Y. Lu. Functional DNA directed assembly of nanomaterials for biosensing. *J. Mater. Chem.*, 19(13):1788–1798, 2009.
- [33] K. C. U. Mugnol, R. A. Ando, R. Y. Nagayasu, A. Faljoni-Alario, S. Brochsztain, P. S. Santos, O. R. Nascimento, and I. L. Nantes. Spectroscopic, structural, and functional characterization of the alternative low-spin state of horse heart cytochrome c. *Biophys. J.*, 94(10):4066–4077, 2008.
- [34] L. Laporte, J. Stulz, and G. J. Thomas. Solution conformations and interactions of alpha and beta subunits of the *Oxytricha nova* telomere binding protein: Investigation by raman spectroscopy. *Biochemistry*, 36(26):8053–8059, 1997.
- [35] H. N. Ritland, P. Kaesberg, and W. W. Beeman. An X-ray investigation of the shapes and hydrations of several protein molecules in solution. *J. Chem. Phys.*, 18(9):1237–1242, 1950.

- [36] S. Rauschenbach. *Electrospray Ion Beam Deposition and Mass Spectrometry of Nonvolatile Molecules and Nanomaterials*. PhD thesis, Ecole Polytechnique Federal de Lausanne, Switzerland, 2007.
- [37] N. Thontasen, G. Levita, N. Malinowski, Z. Deng, S. Rauschenbach, and K. Kern. Grafting crown ether alkali host-guest complexes at surfaces by electrospray ion beam deposition. *J. Phys. Chem. C*, 114(41):17768–17772, 2010.
- [38] J. V. Barth, J. Weckesser, N. Lin, A. Dmitriev, and K. Kern. Supramolecular architectures and nanostructures at metal surfaces. *Appl. Phys. A: Mater. Sci. Process.*, 76(5):645–652, 2003.
- [39] D. Ecija, M. Trelka, C. Urban, P. de Mendoza, E. Mateo-Marti, C. Rogero, J. A. Martin-Gago, A. M. Echavarren, R. Otero, J. M. Gallego, and R. Mirandat. Molecular conformation, organizational chirality, and iron metalation of meso-tetramesitylporphyrins on copper(100). *J. Phys. Chem. C*, 112(24):8988–8994, 2008.
- [40] R. Ohmann, G. Levita, L. Vitali, A. De Vita, and K. Kern. Influence of subsurface layers on the adsorption of large organic molecules on close-packed metal surfaces. *Acs Nano*, 5(2):1360–1365, 2011.
- [41] J. W. Steed and J. L. Atwood. *Supramolecular Chemistry*. John Wiley & Sons, Ltd, West Sussex, 2009.
- [42] D. Chandler. Interfaces and the driving force of hydrophobic assembly. *Nature*, 437(7059):640–647, 2005.
- [43] G. A. Petsko and D. Ringe. *Protein Structure and Function*. New Science Press Ltd, London, 2004.
- [44] X. M. He and D. C. Carter. Atomic-structure and chemistry of human serum-albumin. *Nature*, 358(6383):209–215, 1992.
- [45] K. Dill, S. Bromberg, K. Z. Yue, K. M. Fiebig, D. P. Yee, P. D. Thomas, and H. S. Chan. Principles of protein-folding - a perspective from simple exact models. *Protein Sci.*, 4(4):561–602, 1995.
- [46] J.-M. Lehn. *Supramolecular Chemistry*. VCH, Weinheim, 1995.
- [47] J. M. Lehn. Toward complex matter: Supramolecular chemistry and self-organization. *Proc. Natl. Acad. Sci. U. S. A.*, 99(8):4763–4768, 2002.

- [48] E. P. Kyba, R. C. Helgeson, K. Madan, G. W. Gokel, T. L. Tarnowski, S. S. Moore, and D. J. Cram. Host-guest complexation .1. concept and illustration. *J. Am. Chem. Soc.*, 99(8):2564–2571, 1977.
- [49] D. J. Cram. Preorganization - from solvents to spherands. *Angew. Chem., Int. Ed. Engl.*, 25(12):1039–1057, 1986.
- [50] C. J. Pedersen. Cyclic polyethers and their complexes with metal salts. *J. Am. Chem. Soc.*, 89(26):7017–7036, 1967.
- [51] R. D. Hancock. Chelate ring size and metal-ion selection - the basis of selectivity for metal-ions in open-chain ligands and macrocycles. *J. Chem. Educ.*, 69(8):615–621, 1992.
- [52] A. Kuhnle. Self-assembly of organic molecules at metal surfaces. *Curr. Opin. Colloid Interface Sci.*, 14(2):157–168, 2009.
- [53] Y. Wang, M. Lingenfelder, T. Classen, G. Costantini, and K. Kern. Ordering of dipeptide chains on Cu surfaces through 2D cocrystallization. *J. Am. Chem. Soc.*, 129(51):15742, 2007.
- [54] M. Lingenfelder, G. Tomba, G. Costantini, L. C. Ciacchi, A. De Vita, and K. Kern. Tracking the chiral recognition of adsorbed dipeptides at the single-molecule level. *Angew. Chem., Int. Ed.*, 46(24):4492–4495, 2007.
- [55] F. Frederix, K. Bonroy, G. Reekmans, W. Laureyn, A. Campitelli, M. A. Abramov, W. Dehaen, and G. Maes. Reduced nonspecific adsorption on covalently immobilized protein surfaces using poly(ethylene oxide) containing blocking agents. *J. Biochem. Biophys. Methods*, 58(1):67–74, 2004.
- [56] K. Nishimura, M. Hasegawa, Y. Ogura, T. Nishi, K. Kataoka, H. Handa, and M. Abe. 4 degrees C preparation of ferrite nanoparticles having protein molecules immobilized on their surfaces. *J. Appl. Phys.*, 91(10):8555–8556, 2002.
- [57] H. Sota, Y. Hasegawa, and M. Iwakura. Detection of conformational changes in an immobilized protein using surface plasmon resonance. *Anal. Chem.*, 70(10):2019–2024, 1998.
- [58] L. Baugh, T. Weidner, J. E. Baio, P. C. T. Nguyen, L. J. Gamble, P. S. Slayton, and D. G. Castner. Probing the orientation of surface-immobilized protein G B1 using ToF-SIMS, sum frequency generation, and NEXAFS spectroscopy. *Langmuir*, 26(21):16434–16441, 2010.

- [59] S. Monari, G. Battistuzzi, M. Borsari, G. Di Rocco, L. Martini, A. Ranieri, and M. Sola. Heterogeneous electron transfer of a two-centered heme protein: Redox and electrocatalytic properties of surface-immobilized cytochrome c(4). *J. Phys. Chem. B*, 113(41):13645–13653, 2009.
- [60] J. Zhang, Q. Chi, A. M. Kuznetsov, A. G. Hansen, H. Wackerbarth, H. E. M. Christensen, J. E. T. Andersen, and J. Ulstrup. Electronic properties of functional biomolecules at metal/aqueous solution interfaces. *J. Phys. Chem. B*, 106(6):1131–1152, 2002.
- [61] B. Bonanni, D. Alliata, A. R. Bizzarri, and S. Cannistraro. Topological and electron-transfer properties of yeast cytochrome c adsorbed on bare gold electrodes. *ChemPhysChem*, 4(11):1183–1188, 2003.
- [62] Z. H. Cheng, L. Gao, Z. T. Deng, N. Jiang, Q. Liu, D. X. Shi, S. X. Du, H. M. Guo, and H. J. Gao. Adsorption behavior of iron phthalocyanine on Au(111) surface at submonolayer coverage. *J. Phys. Chem. C*, 111(26):9240–9244, 2007.
- [63] Z. H. Cheng, L. Gao, Z. T. Deng, Q. Liu, N. Jiang, X. Lin, X. B. He, S. X. Du, and H. J. Gao. Epitaxial growth of iron phthalocyanine at the initial stage on Au(111) surface. *J. Phys. Chem. C*, 111(6):2656–2660, 2007.
- [64] O. G. Lutsenko, G. P. Shaposhnikov, and V. P. Kulinich. Synthesis and properties of tetra- and octasubstituted metal phthalocyanines with alkylsulfamoyl groups. *Russ. J. Gen. Chem.*, 74(2):300–304, 2004.
- [65] O. Costisor and W. Linert. Metal directed reactions toward heteroatomic macrocycles: Phthalocyanines, porphyrins and corroles. *Rev. Inorg. Chem.*, 26(5):443–470, 2006.
- [66] J. V. Barth. Molecular architectonic on metal surfaces. *Annu. Rev. Phys. Chem.*, 58:375–407, 2007.
- [67] J. V. Barth, G. Costantini, and K. Kern. Engineering atomic and molecular nanostructures at surfaces. *Nature*, 437(7059):671–679, 2005.
- [68] J. Zeleny. The electrical discharge from liquid points, and a hydrostatic method of measuring the electric intensity at their surfaces. *Phys. Rev.*, 3(2):69–91, 1914.
- [69] J. Zeleny. Instability of electrified liquid surfaces. *Phys. Rev.*, 10:1–6, 1917.
- [70] V. G. Drozin. The electrical dispersion of liquids as aerosols. *J. Colloid Sci.*, 10:158–164, 1955.

- [71] M. Dole, L. L. Mack, and R. L. Hines. Molecular beams of macroions. *J. Chem. Phys.*, 49(5):2240–&, 1968.
- [72] M. Yamashita and J. B. Fenn. Electrospray ion-source - another variation on the free-jet theme. *J. Phys. Chem.*, 88(20):4451–4459, 1984.
- [73] R. B. Cole. *Electrospray Ionization Mass Spectrometry*. John Wiley and Sons, Inc., 1997.
- [74] R. J. Pfeifer and Hendrick.cd. Parametric studies of electrohydrodynamic spraying. *AIAA J.*, 6(3):496, 1968.
- [75] G. Taylor. Disintegration of water drops in electric field. *Proceedings of the Royal Society of London Series A-mathematical and Physical Sciences*, 280(1380):383, 1964.
- [76] M. Cloupeau and B. Prunetfoch. Electrohydrodynamic spraying functioning modes - a critical-review. *J. Aerosol Sci.*, 25(6):1021–1036, 1994.
- [77] Lord Rayleigh. *Philos. Mag.*, 14:184, 1882.
- [78] P. Kebarle and L. Tang. From ions in solution to ions in the gas-phase - the mechanism of electrospray mass-spectrometry. *Anal. Chem.*, 65(22):A972–A986, 1993.
- [79] J. V. Iribarne and B. A. Thomson. Evaporation of small ions from charged droplets. *J. Chem. Phys.*, 64(6):2287–2294, 1976.
- [80] B. A. Thomson and J. V. Iribarne. Field-induced ion evaporation from liquid surfaces at atmospheric-pressure. *J. Chem. Phys.*, 71(11):4451–4463, 1979.
- [81] R. P. Andres J. B. Anderson and J. B. Fenn. *Advances in Atomic and Molecular Physics*. Academic Press Inc., New York, 1965.
- [82] R. Campargue. Progress in overexpanded supersonic jets and skimmed molecular-beams in free-jet zones of silence. *J. Phys. Chem.*, 88(20):4466–4474, 1984.
- [83] S. A. Shaffer, D. C. Prior, G. A. Anderson, H. R. Udseth, and R. D. Smith. An ion funnel interface for improved ion focusing and sensitivity using electrospray ionization mass spectrometry. *Anal. Chem.*, 70(19):4111–4119, 1998.
- [84] V. Grill, J. Shen, C. Evans, and R. G. Cooks. Collisions of ions with surfaces at chemically relevant energies: Instrumentation and phenomena. *Rev. Sci. Instrum.*, 72(8):3149–3179, 2001.

- [85] Y. I. Alivov, D. C. Look, B. M. Ataev, M. V. Chukichev, V. V. Mamedov, V. I. Zinenko, Y. A. Agafonov, and A. N. Pustovit. Fabrication of ZnO-based metal-insulator-semiconductor diodes by ion implantation. *Solid-State Electron.*, 48(12):2343–2346, 2004.
- [86] Y. Otani, Y. Itayama, T. Tanaka, Y. Fukuda, H. Toyota, T. Ono, M. Mitsui, and K. Nakagawa. Fabrication of Ta<sub>2</sub>O<sub>5</sub>/GeN<sub>x</sub> gate insulator stack for Ge metal-insulator-semiconductor structures by electron-cyclotron-resonance plasma nitridation and sputtering deposition techniques. *Appl. Phys. Lett.*, 90(14):142114, 2007.
- [87] S. J. Pearton, C. R. Abernathy, P. W. Wisk, and F. Ren. Ion-implantation and dry-etching characteristics of ingaasp ( $\lambda=1.3\text{-}\mu\text{m}$ ). *J. Appl. Phys.*, 74(3):1610–1615, 1993.
- [88] R. D. Beck, C. Warth, K. May, and M. M. Kappes. Surface impact induced shattering of C-60. detection of small C-m fragments by negative surface ionization. *Chem. Phys. Lett.*, 257(5-6):557–562, 1996.
- [89] H. G. Busmann, T. Lill, and I. V. Hertel. Near specular reflection of C-60 ions in collisions with an HOPG graphite surface. *Chem. Phys. Lett.*, 187(5):459–465, 1991.
- [90] R. C. Mowrey, D. W. Brenner, B. I. Dunlap, J. W. Mintmire, and C. T. White. Simulations of C60 collisions with a hydrogen-terminated Diamond (111) surface. *J. Phys. Chem.*, 95(19):7138–7142, 1991.
- [91] B. Gologan, J. R. Green, J. Alvarez, J. Laskin, and R. G. Cooks. Ion/surface reactions and ion soft-landing. *Phys. Chem. Chem. Phys.*, 7(7):1490–1500, 2005.
- [92] V. H. Wysocki, K. E. Joyce, C. M. Jones, and R. L. Beardsley. Surface-induced dissociation of small molecules, peptides, and non-covalent protein complexes. *J. Am. Soc. Mass Spectrom.*, 19(2):190–208, 2008.
- [93] J. Laskin, P. Wang, and O. Hadjar. Soft-landing of peptide ions onto self-assembled monolayer surfaces: an overview. *Phys. Chem. Chem. Phys.*, 10(8):1079–1090, 2008.
- [94] V. Franchetti, B. H. Solka, W. E. Baitinger, J. W. Amy, and R. G. Cooks. Soft landing of ions as a means of surface modification. *Int. J. Mass Spectrom. Ion Processes*, 23(1):29–35, 1977.
- [95] S. A. Miller, H. Luo, S. J. Pachuta, and R. G. Cooks. Soft-landing of polyatomic ions at fluorinated self-assembled monolayer surfaces. *Science*, 275(5305):1447–1450, 1997.



- [96] Z. Ouyang, Z. Takats, T. A. Blake, B. Gologan, A. J. Guymon, J. M. Wiseman, J. C. Oliver, V. J. Davisson, and R. G. Cooks. Preparing protein microarrays by soft-landing of mass-selected ions. *Science*, 301(5638):1351–1354, 2003.
- [97] H. J. Räder, A. Rouhanipour, A. M. Talarico, V. Palermo, P. Samori, and K. Müllen. Processing of giant graphene molecules by soft-landing mass spectrometry. *Nat. Mater.*, 5(4):276–280, 2006.
- [98] W. P. Peng, G. E. Johnson, I. C. Fortmeyer, P. Wang, O. Hadjar, R. G. Cooks, and J. Laskin. Redox chemistry in thin layers of organometallic complexes prepared using ion soft landing. *Phys. Chem. Chem. Phys.*, 13(1):267–275, 2011.
- [99] S. Rauschenbach, R. Vogelgesang, N. Malinowski, J. W. Gerlach, M. Benyoucef, G. Costantini, Z. T. Deng, N. Thontasen, and K. Kern. Electrospray ion beam deposition: Soft-landing and fragmentation of functional molecules at solid surfaces. *ACS Nano*, 3(10):2901–2910, 2009.
- [100] C. G. Gu and V. H. Wysocki. Ion-surface reactions involving isotopically labeled Langmuir-Blodgett films. *J. Am. Chem. Soc.*, 119(49):12010–12011, 1997.
- [101] J. W. Shen, C. Evans, N. Wade, and R. G. Cooks. Ion-ion collisions leading to formation of C-C bonds at surfaces: An interfacial Kolbe reaction. *J. Am. Chem. Soc.*, 121(41):9762–9763, 1999.
- [102] P. Wang, O. Hadjar, P. L. Gassman, and J. Laskin. Reactive landing of peptide ions on self-assembled monolayer surfaces: an alternative approach for covalent immobilization of peptides on surfaces. *Phys. Chem. Chem. Phys.*, 10(11):1512–1522, 2008.
- [103] Q. C. Hu, P. Wang, and J. Laskin. Effect of the surface on the secondary structure of soft landed peptide ions. *Phys. Chem. Chem. Phys.*, 12(39):12802–12810, 2010.
- [104] R. G. Cooks, T. Ast, and A. Mabud. Collisions of polyatomic ions with surfaces. *Int. J. Mass Spectrom.*, 100:209–265, 1990.
- [105] T. Pradeep, D. E. Riederer, S. H. Hoke, T. Ast, R. G. Cooks, and M. R. Linford. Reactions of metal-ions at fluorinated surfaces - formation of MF(n)(+) (M=Ti, Cr, Fe, Mo, and W, n=1-5). *J. Am. Chem. Soc.*, 116(19):8658–8665, 1994.
- [106] J. A. Burroughs, S. B. Wainhaus, and L. Hanley. Impulsive excitation of Cr(CO)(6)(+) during surface-induced dissociation at organic monolayers. *J. Phys. Chem.*, 98(42):10913–10919, 1994.

- [107] J. A. Burroughs, S. B. Wainhaus, and L. Hanley. Impulsive excitation of FeCp(2)(+) and SiMe(3)(+) during surface-induced dissociation at organic multilayers. *J. Chem. Phys.*, 103(15):6706–6715, 1995.
- [108] C. G. Gu, V. H. Wysocki, A. Harada, H. Takaya, and I. Kumadaki. Dissociative and reactive hyperthermal ion-surface collisions with Langmuir-Blodgett films terminated by CF<sub>3</sub>(CH<sub>2</sub>)<sub>n</sub>-, n-perfluoroalkyl, or n-alkyl groups. *J. Am. Chem. Soc.*, 121(45):10554–10562, 1999.
- [109] R. L. Beardsley, C. M. Jones, A. S. Galhena, and V. H. Wysocki. Noncovalent protein tetramers and pentamers with "n" charges yield monomers with n/4 and n/5 charges. *Anal. Chem.*, 81(4):1347–1356, 2009.
- [110] Z. B. Yang, E. R. Vorpapel, and J. Laskin. Influence of the charge state on the structures and interactions of Vancomycin antibiotics with cell-wall analogue peptides: Experimental and theoretical studies. *Chem.–Eur. J.*, 15(9):2081–2090, 2009.
- [111] J. B. Fenn, M. Mann, C. K. Meng, S. F. Wong, and C. M. Whitehouse. Electrospray ionization for mass-spectrometry of large biomolecules. *Science*, 246(4926):64–71, 1989.
- [112] E. C. Lynn, M. C. Chung, and C. C. Han. Characterizing the transmission properties of an ion funnel. *Rapid Commun. Mass Spectrom.*, 14(22):2129–2134, 2000.
- [113] D. X. Zhang and R. G. Cooks. Doubly charged cluster ions [(NaCl)<sub>m</sub>(Na)<sub>2</sub>]<sup>2+</sup>: magic numbers, dissociation, and structure. *Int. J. Mass Spectrom.*, 195:667–684, 2000.
- [114] M. P. Ince, B. A. Perera, and M. J. Van Stipdonk. Production, dissociation, and gas phase stability of sodium fluoride cluster ions studied using electrospray ionization ion trap mass spectrometry. *Int. J. Mass Spectrom.*, 207(1-2):41–55, 2001.
- [115] N. Thontasen. Electrospray ionization mass spectrometry and vacuum deposition of very low energy molecular ion beams. Master's thesis, Stuttgart University, 2006.
- [116] I. Horcas, R. Fernandez, J. M. Gomez-Rodriguez, J. Colchero, J. Gomez-Herrero, and A. M. Baro. WSXM: A software for scanning probe microscopy and a tool for nanotechnology. *Rev. Sci. Instrum.*, 78(1):013705, 2007.

- [117] S. Berner, M. Corso, R. Widmer, O. Groening, R. Laskowski, P. Blaha, K. Schwarz, A. Goriachko, H. Over, S. Gsell, M. Schreck, H. Sachdev, T. Greber, and J. Osterwalder. Boron nitride nanomesh: Functionality from a corrugated monolayer. *Angew. Chem., Int. Ed.*, 46(27):5115–5119, 2007.
- [118] R. Laskowski, P. Blaha, T. Gallauner, and K. Schwarz. Single-layer model of the hexagonal boron nitride nanomesh on the Rh(111) surface. *Phys. Rev. Lett.*, 98(10):106802, 2007.
- [119] A. Tanaka, Y. Ido, S. Akita, Y. Yoshida, and T. Yoshida. Detection of high mass molecules by laser desorption time-of-flight mass spectrometry. In *Proceedings of the Second Japan-China Joint Symposium on Mass Spectrometry*, pages 185–188, 1987.
- [120] M. Karas and F. Hillenkamp. Laser desorption ionization of proteins with molecular masses exceeding 10000 Daltons. *Anal. Chem.*, 60(20):2299–2301, 1988.
- [121] K. Tanaka. The origin of macromolecule ionization by laser irradiation (Nobel lecture). *Angew. Chem., Int. Ed.*, 42(33):3860–3870, 2003.
- [122] I. A. Kaltashov and S. J. Eyles. *Mass Spectrometry in Biophysics: Conformation and Dynamics of Biomolecules*. John Wiley & Sons, Inc., New Jersey, 2005.
- [123] K. M. Downard, editor. *Mass Spectrometry of Protein Interactions*. John Wiley & Sons, Inc., New Jersey, 2007.
- [124] L. Przybilla, J. D. Brand, K. Yoshimura, H. J. Rader, and K. Mullen. MALDI-TOF mass spectrometry of insoluble giant polycyclic aromatic hydrocarbons by a new method of sample preparation. *Anal. Chem.*, 72(19):4591–4597, 2000.
- [125] A. Rouhanipour, M. Roy, X. L. Feng, H. J. Räder, and K. Müllen. Subliming the unsublimable: How to deposit nanographenes. *Angew. Chem., Int. Ed.*, 48:4602–4604, 2009.
- [126] A. Kabakchiev, K. Kuhnke, T. Lutz, and K. Kern. Electroluminescence from individual pentacene nanocrystals. *ChemPhysChem*, 11(16):3412–3416, 2010.
- [127] Y. L. Wang, S. Fabris, G. Costantini, and K. Kern. Tertiary chiral domains assembled by achiral metal-organic complexes on Cu(110). *J. Phys. Chem. C*, 114(30):13020–13025, 2010.

- [128] J. V. Barth, J. Weckesser, G. Trimarchi, M. Vladimirova, A. De Vita, C. Z. Cai, H. Brune, P. Gunter, and K. Kern. Stereochemical effects in supramolecular self-assembly at surfaces: 1-D versus 2-D enantiomorphic ordering for PVBA and PEBA on Ag(111). *J. Am. Chem. Soc.*, 124(27):7991–8000, 2002.
- [129] B. Gologan, Z. Takats, J. Alvarez, J. M. Wiseman, N. Talaty, Z. Ouyang, and R. G. Cooks. Ion soft-landing into liquids: Protein identification, separation, and purification with retention of biological activity. *J. Am. Soc. Mass Spectrom.*, 15(12):1874–1884, 2004.
- [130] A. R. Dongre, A. Somogyi, and V. H. Wysocki. Surface-induced dissociation: An effective tool to probe structure, energetics and fragmentation mechanisms of protonated peptides. *J. Mass Spectrom.*, 31(4):339–350, 1996.
- [131] M. D. A. Mabud, M. J. Dekrey, and R. G. Cooks. Surface-induced dissociation of molecular-ions. *Int. J. Mass Spectrom. Ion Processes*, 67(3):285–294, 1985.
- [132] R. G. Cooks and A. L. Rockwood. TheThomson - a suggested unit for mass spectroscopists. *Rapid Commun. Mass Spectrom.*, 5:93, 1991.
- [133] J. Alvarez, J. H. Futrell, and J. Laskin. Soft-landing of peptides onto self-assembled monolayer surfaces. *J. Phys. Chem. A*, 110(4):1678–1687, 2006.
- [134] F. Mazzei, G. Favero, M. Frasconi, A. Tata, N. Tuccitto, A. Licciardello, and F. Pepi. Soft-landed protein voltammetry: A tool for redox protein characterization. *Anal. Chem.*, 80(15):5937–5944, 2008.
- [135] K. Ikemoto, S. Nagaoka, T. Matsumoto, M. Mitsui, and A. Nakajima. Soft-landing experiments of Cr(benzene)(2) sandwich complexes onto a carboxyl-terminated self-assembled monolayer matrix. *J. Phys. Chem. C*, 113(11):4476–4482, 2009.
- [136] K. Bromann, C. Felix, H. Brune, W. Harbich, R. Monot, J. Buttet, and K. Kern. Controlled deposition of size-selected silver nanoclusters. *Science*, 274(5289):956–958, 1996.
- [137] H. E. Katz, A. J. Lovinger, J. Johnson, C. Kloc, T. Siegrist, W. Li, Y. Y. Lin, and A. Dodabalapur. A soluble and air-stable organic semiconductor with high electron mobility. *Nature*, 404(6777):478–481, 2000.
- [138] J. S. Brooks. Organic crystals: properties, devices, functionalization and bridges to bio-molecules. *Chem. Soc. Rev.*, 39(7):2667–2694, 2010.
- [139] D. J. Gundlach. Low power, high impact. *Nature Mater.*, 6(3):173–174, 2007.

- [140] H. Klauk, U. Zschieschang, J. Pflaum, and M. Halik. Ultralow-power organic complementary circuits. *Nature*, 445(7129):745–748, 2007.
- [141] B. Kippelen and J. L. Bredas. Organic photovoltaics. *Energy Environ. Sci.*, 2(3):251–261, 2009.
- [142] D. Vaknin, S. Dahlke, A. Travesset, G. Nizri, and S. Magdassi. Induced crystallization of polyelectrolyte-surfactant complexes at the gas-water interface. *Phys. Rev. Lett.*, 93(21):218302, 2004.
- [143] C. Richard, F. Balavoine, P. Schultz, T. W. Ebbesen, and C. Mioskowski. Supramolecular self-assembly of lipid derivatives on carbon nanotubes. *Science*, 300(5620):775–778, May 2003.
- [144] J. S. Zhang, C. Lo, P. Somasundaran, S. Lu, A. Couzis, and J. W. Lee. Adsorption of sodium dodecyl sulfate at THF hydrate/liquid interface. *J. Phys. Chem. C*, 112(32):12381–12385, 2008.
- [145] B. G. Dzikovski and V. A. Livshits. EPR spin probe study of molecular ordering and dynamics in monolayers at oil/water interfaces. *Phys. Chem. Chem. Phys.*, 5(23):5271–5278, 2003.
- [146] V. Rajagopalan, H. Bagger-Jorgensen, K. Fukuda, U. Olsson, and B. Jonsson. Surfactant/water/oil system with weakly charged films: Dependence on charge density. *Langmuir*, 12(12):2939–2946, 1996.
- [147] R. Nagarajan and E. Ruckenstein. Theory of surfactant self-assembly - a predictive molecular thermodynamic approach. *Langmuir*, 7(12):2934–2969, 1991.
- [148] L. A. Smith, A. Duncan, G. B. Thomson, K. J. Roberts, D. Machin, and G. McLeod. Crystallisation of sodium dodecyl sulphate from aqueous solution: phase identification, crystal morphology, surface chemistry and kinetic interface roughening. *J. Cryst. Growth*, 263:480–490, 2004.
- [149] L. A. Smith, G. B. Thomson, K. J. Roberts, D. Machin, and G. McLeod. Modeling the crystal morphology of alkali-metal alkyl surfactants: Sodium and rubidium dodecyl sulfates. *Cryst. Growth. Des.*, 5:2164–2172, 2005.
- [150] L. A. Smith, R. B. Hammond, K. J. Roberts, D. Machin, and G. McLeod. Determination of the crystal structure of anhydrous sodium dodecyl sulphate using a combination of synchrotron radiation powder diffraction and molecular modelling techniques. *J. Mol. Struct.*, 554(2-3):173–182, 2000.

- [151] X. L. Yin, L. J. Wan, Z. Y. Yang, and J. Y. Yu. Self-organization of surfactant molecules on solid surface: an STM study of sodium alkyl sulfonates. *Appl. Surf. Sci.*, 240(1-4):13–18, 2005.
- [152] A. Langner, S. L. Tait, N. Lin, R. Chandrasekar, M. Ruben, and K. Kern. Ordering and stabilization of metal-organic coordination chains by hierarchical assembly through hydrogen bonding at a surface. *Angew. Chem., Int. Ed.*, 47(46):8835–8838, 2008.
- [153] S. Sek, M. H. Chen, C. L. Brosseau, and J. Lipkowski. In situ STM study of potential-driven transitions in the film of a cationic surfactant adsorbed on a Au(111) electrode surface. *Langmuir*, 23(25):12529–12534, 2007.
- [154] E. J. Wanless and W. A. Ducker. Organization of sodium dodecyl sulfate at the graphite-solution interface. *J. Phys. Chem.*, 100(8):3207–3214, 1996.
- [155] M. Petri and D. M. Kolb. Nanostructuring of a sodium dodecyl sulfate-covered Au(111) electrode. *Phys. Chem. Chem. Phys.*, 4(7):1211–1216, 2002.
- [156] J. S. Bernardes, C. A. Rezende, and F. Galembeck. Morphology and self-arranging of SDS and DTAB dried on mica surface. *Langmuir*, 26(11):7824–7832, 2010.
- [157] P. J. Cragg. *A Practical Guide to Supramolecular Chemistry*. Wiley, West Sussex, 2005.
- [158] J. W. Steed, D. R. Turner, and K. J. Wallace. *Core Concepts in Supramolecular Chemistry and Nanochemistry*. Wiley, West Sussex, 2007.
- [159] J. S. Bradshaw and R. M. Izatt. Crown ethers: The search for selective ion ligating agents. *Acc. Chem. Res.*, 30(8):338–345, 1997.
- [160] G. W. Gokel, W. M. Leevy, and M. E. Weber. Crown ethers: Sensors for ions and molecular scaffolds for materials and biological models. *Chem. Rev.*, 104(5):2723–2750, 2004.
- [161] M. Ruben, D. Payer, A. Landa, A. Comisso, C. Gattinoni, N. Lin, J.-P. Collin, J.-P. Sauvage, A. De Vita, and K. Kern. 2D supramolecular assemblies of benzene-1,3,5-triyl-tribenzoic acid: Temperature-induced phase transformations and hierarchical organization with macrocyclic molecules. *J. Am. Chem. Soc.*, 128:15644–15651, 2006.
- [162] D. Payer, S. Rauschenbach, M. Konuma, C. Virojanadara, U. Starke, C. Dietrich, J.P. Collin, J.P. and Sauvage, N. Lin, and K. Kern. Toward mechanical

- switching of surface-grafted [2]catenante by in-situ copper complexation. *J. Am. Chem. Soc.*, 129(0):15662–15667, 2007.
- [163] S. Leininger, B. Olenyuk, and P. J. Stang. Self-assembly of discrete cyclic nanostructures mediated by transition metals. *Chem. Rev.*, 100:853–908, 2000.
- [164] R. M. Izatt, K. Pawlak, J. S. Bradshaw, and R. L. Bruening. Thermodynamic and kinetic data for macrocycle interaction with cations and anions. *Chem. Rev.*, 91(8):1721–2085, 1991.
- [165] S. Maleknia and J. Brodbelt. Gas-phase selectivities of crown ethers for alkali-metal ion complexation. *J. Am. Chem. Soc.*, 114(11):4295–4298, 1992.
- [166] A. Ohira, M. Sakata, C. Hirayama, and M. Kunitake. 2D-supramolecular arrangements of dibenzo-18-crown-6-ether and its inclusion complex with potassium ion by potential controlled adsorption. *Org. Biomol. Chem.*, 1:251–253, 2003.
- [167] L.-P. Xu and L.-J. Wan. STM investigation of the photoisomerization of an Azobis-(benzo-15-crown-5) molecule and its self-assembly on Au(111). *J. Phys. Chem. B*, 110:3185–3188, 2006.
- [168] R. Franski. Complexes of large crown ethers with the lithium cation studied by electrospray ionization mass spectrometry. *Rapid Commun. Mass Spectrom.*, 23(21):3488–3491, 2009.
- [169] I. S. Hwang, R. L. Lo, and T. T. Tsong. Study of the dynamics of point defects at Si(111)-7x7 surfaces with scanning tunneling microscopy. *J. Vac. Sci. Technol., A*, 16(4):2632–2640, 1998.
- [170] J. Tersoff and D. R. Hamann. Theory and application for the scanning tunneling microscope. *Phys. Rev. Lett.*, 50(25):1998–2001, 1983.
- [171] J. Tersoff and D. R. Hamann. Theory of the scanning tunneling microscope. *Phys. Rev. B*, 31(2):805–813, 1985.
- [172] J. M. Berg, J. L. Tymoczko, and L. Stryer. *Biochemistry*. Freeman, New York, 6 edition, 2007.
- [173] J. R. Yates. Mass spectrometry and the age of the proteome. *J. Mass Spectrom.*, 33(1):1–19, 1998.
- [174] M. P. Rout, J. D. Aitchison, A. Suprapto, K. Hjertaas, Y. M. Zhao, and B. T. Chait. The yeast nuclear pore complex: Composition, architecture, and transport mechanism. *J. Cell Biol.*, 148(4):635–651, 2000.

- [175] J. R. Yates. Mass spectral analysis in proteomics. *Annu. Rev. Biophys. Biomol. Struct.*, 33:297–316, 2004.
- [176] E. Jurneczko and P. E. Barran. How useful is ion mobility mass spectrometry for structural biology? the relationship between protein crystal structures and their collision cross sections in the gas phase. *Analyst*, 136(1):20–28, 2011.
- [177] G. W. Bushnell, G. V. Louie, and G. D. Brayer. High-resolution 3-dimensional structure of horse heart cytochrome-c. *J. Mol. Biol.*, 214(2):585–595, 1990.
- [178] S. E. Martinez, D. Huang, A. Szczepaniak, W. A. Cramer, and J. L. Smith. Crystal-structure of chloroplast cytochrome-f reveals a novel cytochrome fold and unexpected heme ligation. *Structure*, 2(2):95–105, 1994.
- [179] L. Banci, I. Bertini, H. B. Gray, C. Luchinat, T. Reddig, A. Rosato, and P. Turano. Solution structure of oxidized horse heart cytochrome c. *Biochemistry*, 36(32):9867–9877, 1997.
- [180] L. Banci, I. Bertini, J. G. Huber, G. A. Spyroulias, and P. Turano. Solution structure of reduced horse heart cytochrome c. *J. Biol. Inorg. Chem.*, 4(1):21–31, 1999.
- [181] L. Holm and C. Sander. Mapping the protein universe. *Science*, 273(5275):595–602, 1996.
- [182] R. Luthy, J. U. Bowie, and D. Eisenberg. Assessment of protein models with 3-dimensional profiles. *Nature*, 356(6364):83–85, 1992.
- [183] N. Ban, P. Nissen, J. Hansen, P. B. Moore, and T. A. Steitz. The complete atomic structure of the large ribosomal subunit at 2.4 angstrom resolution. *Science*, 289(5481):905–920, 2000.
- [184] J. Harms, F. Schlutzen, R. Zarivach, A. Bashan, S. Gat, I. Agmon, H. Bartels, F. Franceschi, and A. Yonath. High resolution structure of the large ribosomal subunit from a mesophilic Eubacterium. *Cell*, 107(5):679–688, 2001.
- [185] N. Ban, B. Freeborn, P. Nissen, P. Penczek, R. A. Grassucci, R. Sweet, J. Frank, P. B. Moore, and T. A. Steitz. A 9 angstrom resolution x-ray crystallographic map of the large ribosomal subunit. *Cell*, 93(7):1105–1115, 1998.
- [186] W. Lee, J. H. Lee, B. K. Oh, and J. W. Choi. Detection of human serum albumin on protein array using scanning tunneling microscopy. *Ultramicroscopy*, 110(6):723–728, 2010.



- [187] T. A. Blake, O. Y. Zheng, J. M. Wiseman, Z. Takats, A. J. Guymon, S. Kothari, and R. G. Cooks. Preparative linear ion trap mass spectrometer for separation and collection of purified proteins and peptides in arrays using ion soft landing. *Anal. Chem.*, 76(21):6293–6305, 2004.
- [188] S. Rauschenbach, F. L. Stadler, E. Lunedei, N. Malinowski, S. Koltsov, G. Costantini, and K. Kern. Electrospray ion beam deposition of clusters and biomolecules. *Small*, 2(4):540–547, 2006.
- [189] I. Bartalesi, A. Rosato, and W. Zhang. Hydrogen exchange in a bacterial cytochrome c: A fingerprint of the cytochrome c fold. *Biochemistry*, 42(37):10923–10930, 2003.
- [190] S. K. Chowdhury, V. Katta, and B. T. Chait. Probing conformational-changes in proteins by mass-spectrometry. *J. Am. Chem. Soc.*, 112(24):9012–9013, 1990.
- [191] D. E. Clemmer, R. R. Hudgins, and M. F. Jarrold. Naked protein conformations - cytochrome-c in the gas-phase. *J. Am. Chem. Soc.*, 117(40):10141–10142, 1995.
- [192] R. K. Jain and A. D. Hamilton. Protein surface recognition by synthetic receptors based on a tetraphenylporphyrin scaffold. *Org. Lett.*, 2(12):1721–1723, 2000.
- [193] M. Mann, R. C. Hendrickson, and A. Pandey. Analysis of proteins and proteomes by mass spectrometry. *Annu. Rev. Biochem.*, 70:437–473, 2001.
- [194] L. Konermann and D. J. Douglas. Acid-induced unfolding of cytochrome c at different methanol concentrations: Electrospray ionization mass spectrometry specifically monitors changes in the tertiary structure. *Biochemistry*, 36(40):12296–12302, 1997.
- [195] F. W. McLafferty, Z. Q. Guan, U. Haupts, T. D. Wood, and N. L. Kelleher. Gaseous conformational structures of cytochrome c. *J. Am. Chem. Soc.*, 120(19):4732–4740, 1998.
- [196] J. V. Barth, H. Brune, G. Ertl, and R. J. Behm. Scanning tunneling microscopy observations on the reconstructed Au(111) surface - atomic-structure, long-range superstructure, rotational domains, and surface-defects. *Phys. Rev. B*, 42(15):9307–9318, 1990.
- [197] J. Zhang, V. Sessi, C. H. Michaelis, I. Brihuega, J. Honolka, K. Kern, R. Skomski, X. Chen, G. Rojas, and A. Enders. Ordered layers of Co clusters on BN template layers. *Phys. Rev. B*, 78(16):165430, 2008.

- [198] B. Lonetti, E. Fratini, S. H. Chen, and P. Baglioni. Viscoelastic and small angle neutron scattering studies of concentrated protein solutions. *Phys. Chem. Chem. Phys.*, 6(7):1388–1395, 2004.
- [199] M. Volny, W. T. Elam, A. Branca, B. D. Ratner, and F. Turecek. Preparative soft and reactive landing of multiply charged protein ions on a plasma-treated metal surface. *Anal. Chem.*, 77(15):4890–4896, 2005.
- [200] L. Gross. Recent advances in submolecular resolution with scanning probe microscopy. *Nature Chem.*, 3(4):273–278, 2011.
- [201] L. Gross, F. Mohn, N. Moll, P. Liljeroth, and G. Meyer. The chemical structure of a molecule resolved by atomic force microscopy. *Science*, 325(5944):1110–1114, 2009.
- [202] L. Gross, F. Mohn, N. Moll, G. Meyer, R. Ebel, W. M. Abdel-Mageed, and M. Jaspars. Organic structure determination using atomic-resolution scanning probe microscopy. *Nature Chem.*, 2(10):821–825, 2010.
- [203] P. G. Wolynes. Biomolecular folding in vacuo(). *Proc. Natl. Acad. Sci. U. S. A.*, 92(7):2426–2427, 1995.
- [204] L. Harnau, R. G. Winkler, and P. Reineker. Dynamic structure factor of semi-flexible macromolecules in dilute solution. *J. Chem. Phys.*, 104(16):6355–6368, 1996.
- [205] H. Tanaka and T. Kawai. Partial sequencing of a single DNA molecule with a scanning tunnelling microscope. *Nature Nanotech.*, 4(8):518–522, 2009.
- [206] S. M. Barlow, S. Louafi, D. Le Roux, J. Williams, C. Muryn, S. Haq, and R. Raval. Polymorphism in supramolecular chiral structures of R- and S-alanine on Cu(110). *Surf. Sci.*, 590(2-3):243–263, 2005.
- [207] A. Schiffrin, A. Riemann, W. Auwarter, Y. Pennec, A. Weber-Bargioni, D. Cvetko, A. Cossaro, A. Morgante, and J. V. Barth. Zwitterionic self-assembly of L-methionine nanogratings on the Ag(111) surface. *Proc. Natl. Acad. Sci. U. S. A.*, 104(13):5279–5284, 2007.
- [208] L. Grill, M. Dyer, L. Lafferentz, M. Persson, M. V. Peters, and S. Hecht. Nano-architectures by covalent assembly of molecular building blocks. *Nature Nanotechnol.*, 2(11):687–691, 2007.
- [209] A. K. Geim and K. S. Novoselov. The rise of graphene. *Nature Materials*, 6(3):183–191, 2007.

- [210] P. Giannozzi et al. QUANTUM ESPRESSO: a modular and open-source software project for quantum simulations of materials. *J. Phys.: Condens. Matter*, 21:395502, 2009.
- [211] J. Perdew, K. Burke, and M. Ernzerhof. Generalized gradient approximation made simple. *Phys. Rev. Lett.*, 77:3865, 1996.
- [212] D. Vanderbilt. Soft self-consistent pseudopotentials in a generalized eigenvalue formalism. *Phys. Rev. B*, 41(11):7892–7895, 1990.
- [213] N. Troullier and J. L. Martins. Efficient pseudopotentials for plane-wave calculations. *Phys. Rev. B*, 43:1993–2006, 1991.
- [214] A. Kokalj. Computer graphics and graphical user interfaces as tools in simulations of matter at the atomic scale. *Comp. Mater. Sci.*, 28:155, 2003.
- [215] C. Rivetti, M. Guthold, and C. Bustamante. Scanning force microscopy of DNA deposited onto mica: Equilibration versus kinetic trapping studied by statistical polymer chain analysis. *J. Mol. Biol.*, 264(5):919–932, 1996.



# Acknowledgement

I would not have accomplished my PhD without a tremendous support from the following people whom I would like to thank for their contribution.

First of all I would like to thank my supervisor, Prof. Klaus Kern for giving me the opportunity to enter the field of research in nanoscience; especially for a chance to work on an ambitious project, which requires a complex unprecedented method of which development I was also engaged in. During this time adequate equipments, materials as well as guidance and supervision were always provided.

I would like to thank the referees; Prof. Johannes Barth, Prof. László Forró and Prof. Thomas Jung for their time on thesis evaluation and the fruitful discussion during the exam.

This work would not have been achieved without considerable support from Dr. Stephan Rauschenbach, who is not only my team leader but also my predecessor and mentor from the very beginning until the very final stage of my work. He taught me everything I need comprehensively in both theoretical and practical aspects; including computation, experiments, writing and presentation. His day-to-day supervision and accompanying in the lab, including exceptional attention on the projects helped me to solve the encountered problems and complete this thesis. Additionally, he provided the possibility for regular or prompt openness discussions, which not only benefited the scientific results but also the working atmosphere.

Special thanks to Dr. Nikola Malinowski, my another mentor who had formerly been working with me in the lab at the beginning of my PhD study and joining our group sometimes as visiting scientist. I learned many things from him particularly mass spectrometry and working attitude, such as being patient and do not overlook the details. Equally I would like to thank Dr. Giovanni Costantini, my former team leader for the guidance and discussion during the beginning of my thesis.

There would be no success without a great team-work. I sincerely thank all the members of the ion beam deposition group. I thank Dr. Zhitao Deng and Gordon Rinke for working together and regular support in the lab, as well as for being my usual audience for rehearsals. Some parts of my dissertation was additionally proof-read by them and Dr. Matthias Pauly, who recently joined our group. Thereby, I received many good ideas and comments for writing. I also thank the former

members, Dr. Yeliang Wang and Dr. Magali Lingenfelder for the introduction to STM and sample preparation. Furthermore, I thank all the students temporarily worked in the group for their useful contributions in the projects.

The instrumental support for MALDI measurement was provided by Prof. Bill from the neighboring Max Planck Institute for Metal Research. Regarding this experimental technique, I also thank Dr. Nadja Amsharov for the discussion and recommendation of matrix molecules.

It would not be possible to carry on the research without technical support. I would like to thank Arthur Küster, Wolfgang Stiepany, and other technicians for their effort and help concerning the experimental apparatus and equipments.

Many works have been performed through internal and external collaboration. I thank all the collaborators especially Dr. Giacomo Levita for his theoretical contribution on the crown ether project by DFT calculations and Dr. Ludgar Harnau for the protein analysis.

Variational supports were also provided by the members of the nanoscale-science department; group leaders, postdocs, PhD students, Master students and interns. I thank them all for scientific discussion, answering questions, providing equipments or giving me support when I need to use additional devices and most importantly for creating a pleasant working environment.

Apart from the lab, the office is also an essential work space. I thank all the colleagues who were sharing the large office with me in 7C4 for shorter or longer time. In spite of the dynamics of the office members, I was always feeling comfortable there. Thank all for being friendly and sharing fruitful conversations and sometimes also afternoon snacks.

I would like to thank the coworkers of the Max Planck Institute for Solid State Research for their support in many aspects during my work here, especially Sabine Birtel and Mrs. King. Others include scientific and computer service groups, mechanical workshop, electronic support, the library, the store, managing departments, the cleaning staffs and the security.

As well as the Max Planck Institute, many people from EPFL had important contributions for my study. I deeply thank Dr. Stefano Rusponi, my PhD tutor in EPFL for his kind regards on the progress of my thesis and for a regular contact to make sure that everything runs smoothly.

Academic procedures in the doctoral program were very well coordinated by Mrs. Anh Eymann, whom I would like to thank for her effort.

My family has always been an essential source of my inspiration who deserves the most credit. I thank my mother, my father and my sister for their permanently unconditional support. I thank my mother particularly for laying a good foundation for me since my first education. She creates the best condition for me, providing me comfort and always encourage me through all my studies. I thank my sister for being my great emotional booster. She can always bring out a smile on my face under any

circumstances.

I thank my friends for spending all up and down times together: hanging out, chill out, celebrating, cheering, and listening. Especially my best friend, Sukhum Ruangchai, whom I thank for his consulting, companying and always being there.

Last but not least, I would like to thank Adrian Lerner for sharing, encouraging, for being undoubtedly reliable and for all the possible support.





# Curriculum Vitae

## Personal Information

Name: Nicha Thontasen  
Date of birth: 16 August 1981  
Place of birth: Nakhonratchasima, Thailand  
Nationality: Thai

## Education

2007-Jul 2011 PhD student in Physics at École Polytechnique Fédérale de Lausanne (EPFL)  

- doing research in the Nanoscale Science Department at Max Planck Institute for Solid State Research (MPI-FKF), Stuttgart

2004-2006 **M.Sc. Physics**, Universität Stuttgart, Germany

2000-2004 **B.Sc. Physics**, Khonkaen University, Thailand

1997-2000 **High School**, Kaennakhon Wittayalai School, Thailand

## Work Experience

### Research

2007-Jul 2011 **Ion Beam Deposition and STM analysis of Macromolecules in UHV**  

- Investigation of nanostructures on solid surfaces by scanning probe techniques (STM/ AFM)
- Functionalization of surfaces in UHV by Electrospray Ion Beam Deposition (ES-IBD)
- Chemical characterization by Matrix-Assisted Laser Desorption Ionization (MALDI) and Time-of-Flight Mass Spectrometry (TOF-MS)

Sep 2005-Nov 2006 **Electrospray Ionization Mass Spectrometry and Vacuum Deposition of Very Low Energy Molecular Ion Beams**  

- Optimization of the TOF and ion optics by computer simulations (SIMION)

Nov 2003-Apr 2004 **Synthesis and Dielectric Properties of  $\text{CaCu}_3\text{M}_4\text{O}_{12}$  (M = Ti, Zr)**  

- Synthesis of materials by Solid State Reaction (SSR) method
- Characterization of bulk materials by X-ray diffraction (XRD), Raman Spectroscopy and Scanning Electron Microscopy (SEM)

### Others

2001-2002 **Tutorship** in English and Mathematics for secondary school students  
Apr 1999 **Student assistant** at Physics Department, Khonkaen University

## Publications

- Z. Deng, N. Thontasen, N. Malinowski, G. Rinke, L. Harnau, S. Rauschenbach, and K. Kern. A close look at proteins: two- and three-dimensional folding at surfaces. *(in preparation)*
- Z. Deng, S. Kahle, N. Malinowski, C. Tonnoir, A. Forment Aliaga, N. Thontasen, G. Rinke, S. Rauschenbach, M. Ternes, and K. Kern. Addressing the magnetic properties of individual Manganese-12-Acetate molecular magnets at the surface. *(in preparation)*
- S. Rauschenbach, R. T. Weitz, N. Malinowski, N. Thontasen, Z. Deng, G. Rinke, G. Costantini, T. Lutz, P. M. de Almeida Rollo, L. Harnau, and K. Kern. Crystalline inverted membrane growth by electrospray ion beam deposition of large highly charges clusters. *(submitted)*
- N. Thontasen, G. Levita, N. Malinowski, Z. Deng, S. Rauschenbach, and K. Kern. Grafting crown ether alkali host-guest complexes at surfaces by electrospray ion beam deposition. *J. Phys. Chem. C*, 114(41):17768-17772, 2010.
- S. Rauschenbach, R. Vogelgesang, N. Malinowski, J. W. Gerlach, M. Benyoucef, G. Costantini, Z. Deng, N. Thontasen, and K. Kern. Electrospray ion beam deposition: soft-landing and fragmentation of functional molecules at solid surfaces. *ACS Nano*, 3(10):2901-2910, 2009.

## Extracurricular Activities

Guiding assistance for foreign students at the university - Volunteer as educational adviser for school students - Take part in the university's sport tournament - Join a cheer leading team in high school

## Languages

**Thai** : native language

**English** : fluent

**German** : competent in speech

## Hobbies

reading, swimming, Latin dancing